

**THE EFFECTS OF NON-UNIFORM INSONATION
ON ULTRASOUND MONITORING OF
CEREBRAL BLOOD FLOW CHANGES**

**Thesis submitted for the degree of
Doctor of Philosophy
At the University of Leicester**

by

**Lorna Sweetman
Department of Cardiovascular Sciences
University of Leicester**

2006

UMI Number: U214051

All rights reserved

INFORMATION TO ALL USERS

The quality of this reproduction is dependent upon the quality of the copy submitted.

In the unlikely event that the author did not send a complete manuscript and there are missing pages, these will be noted. Also, if material had to be removed, a note will indicate the deletion.



UMI U214051

Published by ProQuest LLC 2013. Copyright in the Dissertation held by the Author.
Microform Edition © ProQuest LLC.

All rights reserved. This work is protected against
unauthorized copying under Title 17, United States Code.



ProQuest LLC
789 East Eisenhower Parkway
P.O. Box 1346
Ann Arbor, MI 48106-1346

Abstract

Transcranial Doppler is widely used to measure flow velocity in the middle cerebral artery. These measurements are sometimes combined with Doppler power for use as an indicator of cerebral blood flow changes. This is based on the assumption that the power of the Doppler signal depends on the number of scatterers within the beam, which is proportional to the vessel area, so any changes in vessel area will be matched exactly by changes in Doppler signal power. A three-dimensional numerical model was developed to incorporate data from beam shape measurements with various vessel shapes and sizes in order to study the appropriateness of this assumption. *Post mortem* temporal bone samples were used to create beam shapes similar to those seen *in vivo* and magnetic resonance images were used to create realistic vessel shapes. It was found, using the model, that for a typical, clinical positioning of the ultrasound beam with respect to the vessel the ultrasound field was not uniform and Doppler signal power changes significantly underestimated vessel area changes. A flow phantom was set up to investigate the effects *in vitro*, and *in vivo* recordings from a number of volunteers were also studied. Evidence of non-uniform insonation was seen in both situations, indicating that power and area changes are not equivalent. Using the spectra from the *in vitro* and *in vivo* recordings, it was possible to estimate the shape of the insonating beam and its size relative to the insonated vessel. However, the variance in the beam estimate prevented a direct measurement of changes in vessel size. Instead, a look-up table was derived to allow a correction of signal power measurements to account for non-uniform insonation effects.

Table of symbols and abbreviations

ΔA	Relative change in vessel cross-sectional area
ΔP	Relative change in Doppler signal power
$\varepsilon'_{50\%}$	Eccentricity of ultrasound beam shape
θ	Angle of insonation
BMF	Blood mimicking fluid
c	Speed of sound
CBF	Cerebral blood flow
CT	Computed tomography
DAT	Digital audio tape
ECA	External carotid artery
f_D	Doppler frequency
FFT	Fast Fourier transform
FI	Flow index
f_T	Transmitted ultrasound frequency
GTN	Glyceryl trinitrate, nitroglycerin
ICA	Internal carotid artery
ISB	Intrinsic spectral broadening
IWM	Intensity weighted mean
MCA	Middle cerebral artery
MR	Magnetic resonance
MRA	Magnetic resonance angiography
MRI	Magnetic resonance imaging
P	Total Doppler signal power
$P(v_i)$	Power in the i^{th} bin of the Doppler spectrum
PET	Positron emission tomography

r	Radial distance from the centre of the vessel
R	Radius of vessel
$\overline{r}_{50\%}$	Average radius of beam for which sensitivity is 50% of maximum
rCBF	Regional cerebral blood flow
RF	Radiofrequency
SNR	Signal to noise ratio
SPECT	Single photon emission computed tomography
TAMV	Time averaged maximum velocity
TCD	Transcranial Doppler (ultrasonography)
TMM	Tissue mimicking material
v	Velocity
v_i	Velocity in the i^{th} bin of the Doppler spectrum
VI	Volume index
V_{IWM}	Intensity weighted mean velocity
V_{MAX}	Maximum velocity
V_{MCA}	(Maximum) Flow velocity in the MCA

Table of contents

Chapter 1 – Introduction

Aims	1
Objectives	1
Cerebral blood flow monitoring	1
Techniques	2
Applications	3
Transcranial Doppler ultrasonography	3
MCA anatomy	4
Transducer positioning	5
Doppler signal	5
Flow and Area Indices	6
Evidence for changes in MCA diameter	8
CO ₂ reactivity, Hyperventilation	8
Acetazolamide/Diamox	9
Glyceryl trinitrate, nitroglycerin (GTN)	10
Migraine	10
Caffeine	11
Vasospasm	11
Safety of Transcranial Doppler	12
Conclusions	13

Chapter 2 – Ultrasound Beam Shape

Introduction	14
Method	14
Beam plotting	14
Sensitivity	14
Free field measurements	15
Variation in commercial transducers	15
Distortion by bone	15
Beam profiles	16
Results	16
Freefield beam shape of commercial ultrasound systems	16
Effects of transmission through temporal bone	20
Discussion	23
Sensitivity field asymmetry	24
Axial shape of sample volume	25
Conclusions	26

Chapter 3 – Numerical Model

Introduction	27
Model	28
Assumptions	28
Ultrasound field	28
Coordinate system	28
Simple, straight vessel	29
Angled vessel	29
Realistic vessel paths	30
Magnetic resonance angiography	30

Vessel centre	31
Vessel mask	32
Straight, angled and real vessel paths	34
Discussion	36
Attenuation of blood and tissue	36
Magnetic resonance angiography	36
Real vessel shape	37
High pass filtering	37
Conclusions	38
<u>Chapter 4 – Maps of Doppler signal power</u>	
Introduction	39
Method	39
Results	40
Power maps	40
Angled vessels	43
Real vessel	43
Power changes	44
$\Delta P/\Delta A$	45
Impact of initial vessel diameter	46
Variation of $\Delta P/\Delta A$ with position	46
Discussion	52
Power maps	52
Vessel diameter changes	52
Symmetry of position changes	54
Conclusions	55
<u>Chapter 5 – Production of spectra using the numerical model</u>	
Introduction	56
Method	56
Calculating velocities	56
Sorting to velocity bins	57
Producing spectra	57
Intensity weighted mean velocity	58
Results	59
Discussion	61
ISB	63
Variation in V_{MAX} with insonation depth	64
Conclusions	64
<u>Chapter 6 – <i>In vitro</i> flow phantom recordings</u>	
Introduction	65
Method	65
Flow phantom construction	65
Blood mimicking fluid	65
Signal acquisition	66
Signal processing	67
Maximum velocity envelope	67
Spectral averaging	68
Results	68
Sonograms	68

Averaged spectra	69
Discussion	70
Shape of the spectrum	70
ISB and maximum velocity	70
Spectral averaging	72
Conclusions	72
<u>Chapter 7 – <i>In vivo</i> recordings</u>	
Introduction	73
Method	73
Signal acquisition	73
Systolic identification	73
Flattening the sonogram	74
Long-term repeatability	75
Results	75
Discussion	81
Accuracy of maximum velocity envelope	83
Conclusions	86
<u>Chapter 8 – Reconstructing Beam Shapes</u>	
Introduction	87
Method	87
Converting to radial sensitivity	87
Selecting valid data	88
Fitting data to model	88
Distinguishing different channel sizes <i>in vitro</i>	89
Comparison of relative vessel sizes <i>in vivo</i>	89
Repeatability	90
Results	90
<i>In vitro</i> recordings	90
Variation in channel sizes	91
<i>In vivo</i> recordings	94
Discussion	97
Assumptions necessary for technique	97
Comparison of reconstructed and measured beams	97
Additional attenuation	99
Flow profile	100
Suitability of model beam shape	101
Conclusions	104
<u>Chapter 9 – Summary and Conclusions</u>	
Summary of work	105
Further work	107
Using reconstructions to correct signal power method	107
Verification of signal power correction factors	108
Checking reconstruction technique <i>in vivo</i> in vasospasm	109
Conclusions	109
<u>References</u>	110

Chapter 1 – Introduction

Aims

Transcranial Doppler ultrasonography (TCD) is a useful tool for the monitoring of cerebral haemodynamics. Its low cost and ease of use have led to widespread utilisation of the technique for cerebral blood flow (CBF) monitoring in many different applications. However, this ubiquity may bring TCD into areas where it is being employed beyond the limits of its accuracy. This project aimed to determine those limits; quantify the errors that may arise when the limits were exceeded; and propose methods by which those errors could be reduced or corrected.

Objectives

The main objective of this project was to develop a numerical model to simulate the interaction between a non-uniform ultrasound field and a blood vessel and to use this model to evaluate the magnitude of the effect that inhomogeneities in the insonating beam would have on the power of the Doppler signal. Further investigation was then made into the consequent effect on any techniques using power to monitor the Doppler signal for changes in vessel diameter.

Data were collected *in vitro* from a variety of commercial TCD systems using *post mortem* temporal bone samples to produce a realistic form of the *in vivo* ultrasound field. This was combined with angiographic data on the shapes and sizes of typical cerebral arteries.

A secondary objective was the creation of a technique capable of identifying changes in vessel size based on beam shape information extracted from the Doppler signal. This was used to observe size differences between phantom vessels *in vitro* and to track vasoreactivity in the cerebral arteries *in vivo*.

Cerebral blood flow monitoring

The gold standard for measurements of global cerebral blood flow is a calculation of flow based on the Fick principle. It involves the introduction of a tracer into the arterial blood supply and the measurement of the concentration of the tracer in the venous outflow. The first use of this technique, by Kety and Schmidt (1945), signalled the

beginning of the modern era of CBF measurement, but it is invasive and only provides information on global values of CBF.

Techniques

Radionuclide imaging techniques using the γ emitter ^{133}Xe allow limited measurements of regional variations in CBF (rCBF). Individual radiation detectors positioned over different parts of the head measure the relative distribution of activity in the brain. The tracer is generally introduced by inhalation rather than intravenous injection, making the technique more acceptable for many subjects. The ^{133}Xe enters the cerebral circulation and passes through the blood-brain barrier. It is retained in the cerebral tissues for a short time before being released into the venous system. The detectors are used to follow the clearance curve of the radionuclide and CBF is calculated from the decay rate. A single detector may be placed over any part of the cerebrum, or a number of detectors may be used simultaneously. They are restricted to photon emissions from a particular region of interest by the use of collimators, but scattering from neighbouring regions may obfuscate measurements of regional CBF. ^{133}Xe is quickly removed from the circulation by the lungs and measurements can be repeated at 10-minute intervals with errors of only 5%.

Improved spatial resolution can be achieved by using single photon emission computed tomography – SPECT – (Lassen et al. 1981). The six hour half-life of $^{99\text{m}}\text{Tc}$ -based radiopharmaceuticals has the advantage of allowing the patient to be imaged a number of hours after administration but this method only provides qualitative information. An alternative technique using ^{123}I -IMP (isopropyl-iodoamphetamine) can be used for quantitative measurements (Ogasawara et al. 2003) but is very expensive. Whichever radiopharmaceutical is used, the imaging process is the same: a ring of detectors, or a rotating camera head, images the distribution of radioactive tracer within the patient from a number of angles. These projection images can then be reconstructed into two-dimensional transverse slices or a three-dimensional image. CBF can be established from the signal strength. Positron emission tomography (PET) provides even higher spatial resolution. The tracer used – water, labelled with ^{15}O – is introduced by inhalation of labelled CO_2 , which the lungs convert to H_2^{15}O . PET scanning is only available in specialist centres and the cost is high.

Other imaging techniques such as x-ray computed tomography (Axel 1980) and magnetic resonance imaging (MRI) may be employed. MRI can produce maps of

cerebral perfusion, using gadolinium contrast agent or endogenous tracers (Detre et al. 1998) such as haemoglobin. The most commonly used MRI techniques currently are called BOLD (blood oxygen level dependent) techniques. Computed tomography (CT) techniques also use contrast agents (dye contrast, or inhaled Xe) to provide spatial information on cerebral perfusion.

Applications

CBF monitoring is used for a wide range of diagnostic and prognostic purposes such as stroke, head trauma, Alzheimer's disease (Hunter et al. 1989). It is also widely used in studies of cerebral autoregulation (Skinhøj et al. 1970), vasomotor reserve (Detre et al. 1999) and migraine (Edmeads 1977). Although some investigations require only a single measurement, many others rely on serial measurements to detect changes in a condition or to follow the physiological response to a stimulus. The doses for the nuclear medicine tests are low, but the risk to the patient or research subject increases with each exposure, so frequent repetitions of these tests should be avoided. Magnetic resonance imaging techniques have the disadvantages of being costly and time consuming and some individuals find it difficult to tolerate the confined space and loud noise associated with the scans.

Transcranial Doppler ultrasonography

Transcranial Doppler (TCD) is an alternative to these techniques that is capable of providing long-term information on changes in cerebral haemodynamics without the risks of exposure to ionising radiation or the inconvenience of magnetic resonance imaging. As a non-imaging technique, it is limited in the spatial information it can provide. Changes in CBF are monitored by measuring the flow velocities in the main cerebral arteries. Most commonly, the middle cerebral artery (MCA) is the vessel of interest, but the posterior cerebral artery may be studied by groups concentrating on flow in the occipital region.

TCD monitoring of CBF is used in a wide variety of practices, both for its convenience and low cost and when other techniques would be unsuitable such as in vasomotor reserve studies. Recently, the field of functional TCD (Kelley et al. 1992) has seen a rapid expansion. Other groups/workers have used TCD measurements of MCA velocity to study CBF response to different stimuli (Haase et al. 2005), to look at the

integrity of cerebral autoregulation and to search for the underlying causes of migraine headache (Muller and Marziniak, 2005).

In almost all situations, an assumption of direct proportionality between the velocity in the MCA and CBF is made. This approach makes no allowances for changes in vessel diameter, nor does it consider the issue of non-uniform insonation. Non-uniform insonation gives an unequal weighting to signals from different parts of the vessel and can affect the accuracy of power and mean velocity calculations.

MCA anatomy

The head is supplied with blood through four main vessels: the left and right common carotid arteries and the left and right vertebral arteries. In a healthy subject, the majority of the blood flows through the carotid arteries. These bifurcate below the level of the ear, into the external and internal carotid arteries (ECA and ICA, respectively). The ECA principally supplies the superficial tissues whilst the ICA – taking the majority of the blood volume – supplies the brain. The middle cerebral artery originates at the distal end of the ICA and carries 80% of the blood flow from this vessel. The MCA (Figure 1.1) follows a horizontal path from the circle of Willis at the centre of the brain toward the lateral skull just above the level of the zygomatic arch and bifurcates at the sylvian fissure. The mean diameter of the proximal vessel lumen is 2.70 ± 0.25 mm (van der Zwan et al. 1993). The M1 segment refers to the section of the vessel from the origin to just beyond the bifurcation. The MCA is the main supply vessel to the parietal and temporal regions of the brain.

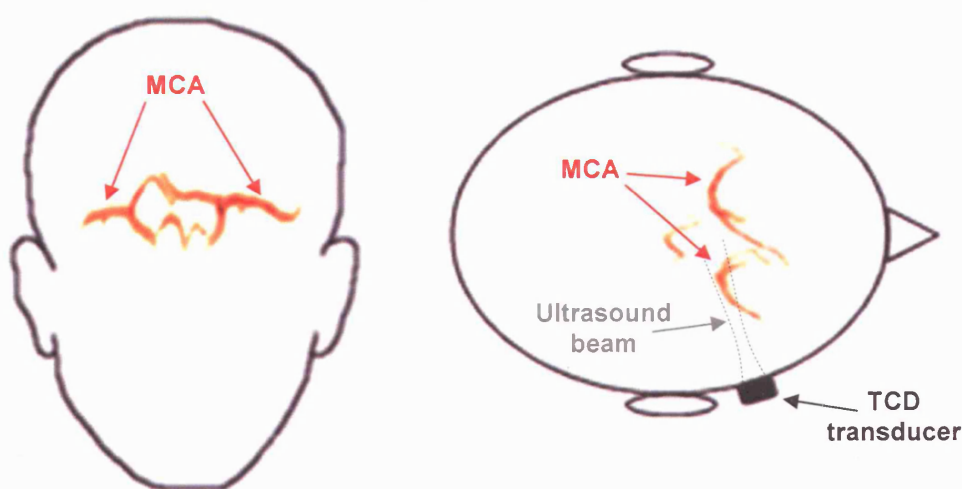


Figure 1.1. Anatomy of the middle cerebral arteries and positioning of ultrasound transducer

Transducer positioning

TCD makes use of the reduced thickness of the temporal bone in the region between the top of the ear and eye to transmit the beam of ultrasound into the brain. The path of the MCA – generally perpendicular to the skull – and its other characteristics make it an ideal vessel for investigations of general CBF.

TCD signals from the MCA are typically found at depths of 3.5 – 6.0 cm from the skull. The exact angle between the vessel and ultrasound beam depends on the anatomy of the vessel and the placement of the ultrasound transducer and is usually unknown, but assumed to be less than 30°. It has been shown that this angle can be exceeded, at least in elevation, for children with hydrocephalus (Finn et al. 1990).

In certain patients and certain groups of patients – generally older women (Itoh et al. 1993, Marinoni et al. 1997, Hoksbergen et al. 1999) – the anatomy of vessel and cranium may not allow a Doppler signal to be obtained. Halsey et al. (1990) measured the intensity of the received Doppler signal in different patient groups for a transmitted power of 800 mW.cm⁻² and found that the intensity was lowest for black women and highest for white men. This matched with their findings – from the study of *post mortem* bone samples – that the temporal bones of black women were significantly thicker, and those of white men were significantly thinner, than the other patient groups. *In vivo* CT studies have also shown that patients with poor ultrasound windows have thicker skulls (Jarquin-Valdivia et al. 2004). The higher attenuation of the sound wave by the thicker bone is the most likely reason for the unavailability of ultrasound signals in this particular group.

Doppler signal

The ultrasound transmitted into the skull is scattered by the red blood cells and some of the echoes return to the transducer. The frequency of the returned signal is shifted by an amount proportional to the velocity of the scatterers according to the Doppler effect:

$$f_D = \frac{2v}{c} f_T \cos \theta . \quad \text{Equation 1.1}$$

where f_D and f_T are the frequencies of the returned Doppler signal and the transmitted ultrasound, respectively, v is the velocity of the blood, c the speed of sound and θ the angle between the direction of flow and the ultrasound beam.

Pulsed Doppler produces a composite signal of the Doppler shift frequencies of all the targets within the sample volume. The width of the ultrasound beam, the length of the transmitted pulse and the time for which received signals are accepted define the boundaries of the sample volume. Uniform insonation means that the relative weighting of the different Doppler frequencies depends on the number of scatterers travelling at each velocity. Non-uniform insonation, non-straight vessels and non-zero angles of insonation complicate this picture and combine with characteristics of the signal reception and processing system to modulate the Doppler signal in a number of ways.

In the first decade of its use, much work was done in investigating the reproducibility of TCD velocity measurements. Maeda et al. (1990) determined intra- and inter-observer coefficients of variation of less than 14% and correlation coefficients ≥ 0.71 . Totaro et al. (1992) found that correlation coefficients increased from ≥ 0.76 to ≥ 0.91 if only recordings where $V_{MCA} > 40$ cm/s were considered. Low values of V_{MCA} may arise from a large value of θ and the reduced correlation coefficients for this group of recordings may be due to variations in θ greater than the limited range of angles usually possible through such a small window.

Flow and Area Indices

The complication of vessel diameter changes on CBF monitoring via TCD has been studied by several groups, who have produced index measurements that attempt to detect or compensate for vessel diameter changes (Poulin and Robbins 1996, Hatab 1997, Giller et al. 1998). The power of the Doppler signal depends, amongst other factors, on the number of targets available to scatter the incoming ultrasound pulse. Physiological changes – an increase or decrease in the haematocrit – can alter this number. Scattering is at a maximum for a haematocrit of 24-30%. Normal haematocrit is around 45% and does not change rapidly without external intervention. It will be assumed throughout that haematocrit is unchanging and that, for a fixed transducer, any change in power would be expected to have come from a change in the volume of blood within the sample volume, i.e. a change in the diameter of the vessel. By combining a measure of power, P , with the velocity, V , a flow index, FI, can be calculated. Such flow indices were described in Poulin and Robbins (1996) and Niehaus et al. (1998),

$$FI = P \cdot V_{IWM} \quad \text{Equation 1.2}$$

As, V_{IWM} , the intensity weighted mean velocity (Arts and Roelvros 1972, DeJong et al. 1975), is calculated by

$$V_{IWM} = \frac{\sum_i p_i v_i}{\sum_i p_i} \quad \text{Equation 1.3}$$

where p_i is the power of the signal in the i^{th} velocity bin, v_i , the expression for flow can be rearranged to

$$FI = \sum_i p_i v_i \quad \text{Equation 1.4}$$

Essentially FI is the first moment of the spectral power.

Different area indices, AI, have also been proposed. The first is the total power (Poulin et al. 1999) in the Doppler signal at each time, $P(t)$ – the zeroth moment of spectral power. The second is FI divided by the maximum velocity,

$$\frac{FI}{V_{\max}(t)} \quad \text{Equation 1.5}$$

This, second, index was proposed by Hatab et al. (1997) who instead refer to $P(t)$ as a volume index, VI, and doubt its ability to act as a surrogate for an AI, because of its sensitivity to variations in beam shape. This definition of AI was also preferred by Giller et al. (1998) for being less dependent on the shape of the beam and they were able to show good qualitative agreement between changes in vessel size determined by this AI and those determined angiographically.

Most indices are calculated over a number of consecutive beats of the sonogram rather than for each spectral estimate, so $V_{\max}(t)$ becomes the time averaged maximum velocity (TAMV).

In their work, Hatab et al. (1997) studied flow and area indices for different channel sizes in a phantom. They briefly mentioned the issue of a finite sample volume size, in relation to the difference between volume and area indices, but did not investigate the effects that non-uniform insonation would have on their measurements. Russell and

Brucher (2004) have also used cross-sectional area indices calculated by Equation 1.5 to study changes in the MCA in response to pharmaceutical agents.

All of these techniques assume that changes in signal power are directly proportional to changes in vessel area. This is the same as assuming that the average sensitivity in the changed area is the same as the average sensitivity in the original area, or that there is uniform insonation.

Evidence for changes in MCA diameter

Some published work has indicated a constant MCA diameter in certain situations, such as carotid surgery (Lindegard et al. 1987). However, an assumption that constant diameter applies in all situations may not be valid. It has been proposed that the MCA does not have the same degree of vasoreactivity as smaller arteries. Some work has indicated significant changes in vessel diameter during migraine headache and vasospasm. Small changes in MCA diameter have been seen concurrent with larger changes in the downstream vessels. Most reports of MCA reactivity have relied on flow index techniques or x-ray angiography. Other research that relies on magnetic resonance angiography has been hampered by the relatively poor resolution of the technique – minimum pixel sizes of 0.4 mm, or 20% of the typical vessel lumen diameter.

CO₂ reactivity, Hyperventilation

Valdueza et al. (1997a) studied the effect of hyperventilation on velocity and MCA diameter. They showed that, although V_{MCA} dropped by $49.6 \pm 5.7\%$ during hyperventilation, no diameter change was observable in the magnetic resonance images. A further study (Valdueza et al. 1997b) adding measurements of MR flow, corroborated the TCD measured flow change while still failing to show any diameter change in the images of the MCA.

In another respiratory-protocol based study with a dynamic end-tidal forcing system, Poulin and Robbins (1996), showed an increase in Doppler signal power of 3.8% after removal of a combined hypoxic and hypercapnic stimulus, but no significant differences in response to either hypoxia or hypercapnia alone. Significant increases in peak velocity were seen in all three states.

Clark et al. (1996) studied CBF using ^{133}Xe clearance over a range of arterial CO_2 levels, from hypocapnia to hypercapnia, simultaneously using TCD to measure V_{MCA} . They showed increases in both V_{MCA} and CBF as arterial Pco_2 increased, with a progressively increasing slope in the hypocapnic region to a linear response in hypercapnia. In comparison with their baseline of breathing 100% O_2 at rest, the data showed evidence of MCA dilation in both hypercapnia and hyperventilatory hypocapnic states.

Acetazolamide/Diamox

The vasodilating effect of CO_2 is used to study the capacity of the distal cerebral vessels to expand. This is an indicator of the reserves available to adapt to haemodynamic insults induced by proximal stenoses or occlusions. In studies that use a breathing protocol there may be problems of patient compliance or difficulties in achieving a maximally stressed cerebrovascular system (Settakias et al. 2003). As an alternative, a protocol using acetazolamide (Diamox) – a carbonic anhydrase inhibitor that increases the concentration of CO_2 in blood plasma – may provide results that are more accurate.

Dahl et al. (1994) studied changes in V_{MCA} and rCBF for patients with unilateral carotid artery disease. They found that both quantities showed side-to-side asymmetry in response to an administration of 1 g of acetazolamide, but there was poor correlation between the quantitative changes in flow and velocity. Démolis et al. (1996) cast doubt on the appropriateness of using TCD to measure the cerebrovascular response to acetazolamide when they were unable to show a correlation between ^{133}Xe SPECT-measured changes in CBF and changes in V_{MCA} . In neither case was an attempt made to measure MCA diameter changes, which Dahl et al. (1994) admitted could be responsible for the discrepancy between changes in velocity and flow.

Eicke et al. (1999) used a colour, duplex, M-mode system to monitor CCA diameter and flow velocity in volunteers who were administered 1 g acetazolamide. Through measurements of MCA flow velocities simultaneous with M-mode imaging of the CCA, they determined an increase in MCA diameter of 4%. A further test with 5% CO_2 inhalation also produced MCA dilation, this time by 6%. However, when Kleiser et al. (1995) looked for evidence of MCA diameter changes, by comparing the velocity in both the MCA and the extracranial ICA, their measurements showed no difference in the diameter of the ICA during normo- and hyper-capnia. This, together with the

insignificant differences between the velocity increases in the two vessels, indicated that the MCA diameter was constant.

A study of the dose related effects of acetazolamide (Dahl et al. 1995), showed a significant linear correlation between dose (in mg/kg) and maximum increase in V_{MCA} that was not seen in the SPECT measurements of rCBF. This is an unexpected result, as an increase in velocity without a concurrent increase in flow would indicate constriction of the MCA instead of the expected dilation. However, an MRI study of changes in CBF in patients with cerebrovascular stenosis (Dette et al. 1999) showed a variation in CBF from -33% to +164% after administration of acetazolamide, so it may be that there are large variations in the individual responses to the drug.

Glyceryl trinitrate, nitroglycerin (GTN)

The effect of GTN on V_{MCA} and CBF has also been studied. Dahl et al. (1989) combined measurements of TCD and ^{133}Xe inhalation SPECT. They found that there was no significant change in hemispheric CBF, but V_{MCA} dropped by 26% after sublingual administration of 1 mg GTN. White et al. (2000) observed dose-dependent velocity decreases in the MCA during GTN infusion, whilst volume flow in the CCA and ICA remained constant. Global and regional CBF were also unchanged. The maximum decrease in V_{MCA} was 24.7% in response to an infusion rate of 1.0 $\mu\text{g}/\text{kg}/\text{min}$. Finally, Bednarczyk et al. (2002) used an infusion of GTN to provoke migraine-type headaches in a group of healthy volunteers without any previous history of migraine. During the infusion, global CBF was unchanged, although there were regional variations, and V_{MCA} decreased by 11.7% - 20.8% depending on the level of infusion. All three of these papers imply a dilation of the MCA. In keeping with these findings, Russell and Brucher (2004) found that a 1 mg dose of nitroglycerin could cause an average increase in MCA area of 25% without any change in flow.

Migraine

The underlying phenomena of abnormal cerebrovascular reactivity and increased vasoneuronal coupling are suspected to exist in patients with migraine and have frequently been investigated with TCD (Totaro et al. 1997a, Baezner et al. 1999, Silvestrini et al. 2004). Indeed, experiments in provocation of migraine attacks using vasodilating pharmaceuticals – e.g. GTN, as previously mentioned, and dipyrindamole – have indicated an element of vasoreactive behaviour of the cerebral vessels in the aetiology of the disease. Using an area index, Friberg et al. (1991) demonstrated evidence of vasodilation during a migraine attack, which could be reversed using

pharmaceuticals from the triptan family of 5HT₁ agonists. In their 2004 study, Russell and Brucher found that sumatriptan, in particular, could reduce MCA cross-sectional area by 16.5%. Studies that measured flow velocities alone have shown reduced V_{MCA} at the onset of a spontaneous migraine attack that increased after sumatriptan administration, at least on the headache side (Totaro et al. 1997b). Unlike the trial of Bednarczyk et al. mentioned above, Thomaidis et al. (2003) found that the reduction in V_{MCA} caused by GTN was only significant ($p < 0.01$) in migraine sufferers and not in the control group. In this study, the reduced flow velocities during the provoked migraine were increased by triptan administration, as they were in the case of spontaneous headache. Schmetterer et al. (1996) in their study of GTN-provoked migraine found that the increase in V_{MCA} from sumatriptan did not extend to the ophthalmic artery, where velocities remained reduced.

Kruuse et al. (2000) looked at the effect of an infusion of dipyridamole on the V_{MCA} and rCBF of healthy subjects. When rCBF values were corrected for the variation in PCO_2 , there was no change seen during the dipyridamole infusion but, PCO_2 -corrected values of V_{MCA} decreased by $8.4\% \pm 11.7\%$. However, other work carried out by Kruuse et al. (2003), using sildenafil (Viagra®) also triggered migraine-type headaches without changes in either V_{MCA} or global CBF.

Caffeine

The effect of caffeine on CBF has also been looked at with some interest, due to the frequent consumption of caffeine by the general population and the concern that it might be detrimental to those recovering from strokes. Using ¹³³Xe clearance Ragab et al. (2004) showed that CBF was reduced after caffeine administration in both patients and controls. They confirmed this using TCD. Although it was not discussed, the reduction in CBF was larger than the reduction in V_{MCA} , which could indicate a narrowing of the MCA although it was not possible to determine this conclusively from the data presented. Lunt et al. (2004) specifically compared the effect of caffeine on CBF and V_{MCA} . They measured a reduction of 22% in CBF using a xenon-clearance method, but V_{MCA} was only reduced by 13%. Using a Poiseuille model of flow in the arteries and arterioles, they predicted that there was a diameter reduction of 4.3% in the MCA, and a reduction of 5.9% in the arterioles.

Vasospasm

Cerebral vasospasm is a complication of subarachnoid haemorrhage involving a severe narrowing of the cerebral arteries. TCD diagnosis of vasospasm is generally based on raised velocities in the MCA (Mascia et al. 2002). Further increases in

velocity subsequent to diagnosis are considered indicative of an exacerbation of the condition. The acceptance of TCD for diagnosis and monitoring of the course of vasospasm is not uncontested and comparisons with other methods of CBF measurement often show discrepancies between the techniques (Vajkoczy et al. 2001). Oskouian et al. (2002) studied 45 patients undergoing treatment for vasospasm, comparing ^{133}Xe -clearance measurements of hemispheric CBF ($\text{CBF}_{15\text{-H}}$) with TCD measured MCA velocities and calculating a spasm index, $V_{\text{MCA}}/\text{CBF}_{15\text{-H}}$. After treatment, the spasm index decreased in all patients, although the decrease reversed in patients treated with intra-arterial papaverine alone. Patients treated with balloon angioplasty showed an average increase of 62.9% in the diameter of the intermediate vessels, which included the M1 segment of the MCA, with a contemporaneous reduction in V_{MCA} of 51.6%. (Low spasm indices could be seen in patients with severe vasospasm, if CBF is maintained through a well-developed collateral network of vessels.)

Safety of Transcranial Doppler

Safety advice to sonographers often includes the instruction to avoid keeping the beam in the same location for long periods and to keep power levels low (British Medical Ultrasound Society 2000). TCD monitoring of CBF generally requires contravention of the first directive, but there have been no reports of deleterious effects in humans resulting from its use at diagnostic power levels. The Output Display Standard (AIUM and NEMA, 1992) was introduced in the United States as a means by which ultrasound safety could be increased. The standard proposed four indices, of which Tlc – the thermal index for superficial bone – is most appropriate for transcranial applications. The displayed value of Tlc should represent the ratio of the acoustic output to the acoustic power required to produce a 1° rise in the temperature of tissue. ODS indices are not often seen on standalone Doppler equipment but when they are available they are likely to be inaccurate because they do not include the contribution of transducer self-heating (Shaw et al. 1998). Bone is a strong attenuator of ultrasound and it has been shown to increase the thermal hazard of ultrasound by concentrating heating effects near its proximal surface, through the generation and rapid absorption of transverse waves and strong reflection of longitudinal waves (Fujii et al. 1999). In TCD, both the effects of a bone-soft tissue interface and transducer self-heating will be concentrated in the more superficial tissues. However, studies have mostly looked at situations where there are significant amounts (~ 5 cm) of soft tissue overlying the

bone (Moros et al. 2004). Wu et al. (1995) developed a specific transcranial phantom and found that the calculated values of Tlc were, indeed, an underestimate of the actual temperature rises that they measured. However, their model was unable to account for perfusion, which may have a lowering effect on temperature.

The techniques described later in this thesis do not require any monitoring of the blood flow signal additional to that which would already be performed, nor do they require higher power levels. Instead, they use either off-line processing of the collected data to derive calibration factors which can be applied to the Doppler information to improve the accuracy of the measurements.

Conclusions

All of these investigations, with the variability of their outcomes that indicate different amounts of vasoreactivity or, indeed, lack of vasoreactivity underline the difficulty in measurement of cerebral blood flow and MCA diameter. While it is not universally accepted, there is much evidence to show that changes in MCA diameter do occur, at least in response to certain pharmaceuticals, such as GTN and triptans, and in certain conditions, e.g. migraine. In light of this, a robust method for correcting flow velocity measurements to account for cross-sectional area changes seems necessary. Although the work presented in this thesis does not aim to solve the problem in its entirety, it is hoped that the techniques described may be of some use in reducing the uncertainties arising from the use of TCD for CBF monitoring.

Chapter 2 – Ultrasound Beam Shape

Introduction

If non-uniform insonation of the MCA does occur, it must arise from either the intrinsic beam shape or the distortion of the beam by the cranial bone. A number of different commercial ultrasound systems were studied to determine the typical profile of a TCD beam. The normal diameter of the M1 segment of the MCA is approximately 2.9 mm (Serrador et al. 2000). In comparison, the physical dimensions of the housing of transcranial Doppler transducers are generally no more than 2 cm in diameter and are often less than this. Indeed, the diameter of the piezoelectric crystal will, naturally, be smaller than the housing. Along with the physical size of the crystal and the wavelength of the ultrasound, the degree of focussing of the transducer will dictate the 'flatness', or uniformity, of the ultrasound field. An indication of the shape and size of the extrinsic beam – the beam as would be measured within the skull – was obtained by placing samples of temporal bone in the path of the ultrasound beam. The measured beam diameters were compared to the typical MCA diameter to determine the degree of non-uniformity that might be expected *in vivo*.

Method

Beam plotting

All measurements of the transmitted ultrasound power were made in a large water tank, with the transducer coupled to a thin polythene window using standard ultrasound gel. A complete ultrasound system – SciMed QVL120 (SciMed, Bristol, UK) – with a 2 MHz transcranial transducer was used with the standard clinical settings for depth and sample volume length. The output power was reduced as necessary to prevent saturation of the measured signal. A needle hydrophone (Precision Acoustics, Dorset, UK) was fixed to a support and submerged in the tank. Computer controlled motors drove the movement of the support in the *x*-, *y*- and *z*-directions. In-house developed software collected pressure measurements at a user-defined resolution over a chosen volume of interest. The signal was available either as a digitised RF pulse or the peak positive value as captured by a peak detector circuit. These data, when acquired by the motion control software, were written to disk in a format suitable for further analysis in the MATLAB programming environment. Each plane of data took approximately 50 minutes to collect, thus a full beam plot of 7-10 planes required a whole working day.

Sensitivity

The power of a Doppler blood flow signal depends on several factors, including the number of scatterers in the beam and the sensitivity of the ultrasound system. The

overall sensitivity is a combination of the transmitted intensity and the configuration of the reception zone. For a single crystal transducer, the shape of the sensitivity field can be assumed identical to the transmission field. Thus, the overall sensitivity is proportional to the square of the transmitted intensity, i.e. the fourth power of the amplitude of the hydrophone signal.

Free field measurements

The intrinsic beam shape measurements were made with the ultrasound propagating along a homogenous water path. The transducer was clamped in position at the front of the water tank and the TCD system was switched on. The hydrophone was manually positioned in the centre of the beam using an oscilloscope to check the hydrophone output and the transmitted power was reduced, as appropriate, to avoid saturation of the signal. Care was taken to exclude any air bubbles or excess coupling gel from the area between the transducer face and the polymer window. Pressure data were collected at 0.5 mm steps over two planes of 15 mm x 15 mm at distances of 5 cm and 6 cm from the transducer face. The measurements were processed to produce maps of the relative sensitivity at each position in the field. Both plots were interpolated to a resolution of 0.1 mm using a 'spline' two-dimensional interpolation routine. A square of side 10 mm at the centre (the point of maximum sensitivity) of the interpolated field was isolated.

Variation in commercial transducers

The outputs of two other commercial ultrasound systems – the SciMed PCDop842 and TC22 – were measured and compared with the results from the QVL120. Again, the sensitivity over two planes at 5 cm and 6 cm from the transducer was plotted. Both of these systems were operated at the same frequency as the QVL120, i.e. 2 MHz.

Distortion by bone

The distorting effect of the skull on the ultrasound beam was determined by placing samples of human temporal bone between the transducer of the QVL120 and the window of the water tank. The process of recording data in two planes 5 cm and 6 cm from the transducer was again followed. The field of view of the plots was increased, when necessary, for the most distorted beams to avoid missing features such as secondary lobes. However, all the interpolated plots were ultimately reduced to 10 mm x 10 mm centred on the point of maximum sensitivity. Plots were made for each of the four different samples of bone.

Beam profiles

One-dimensional beam profiles were created from the two-dimensional plots of sensitivity. These correspond to the off-axis variation in sensitivity. Generally, transcranial ultrasound beams are axisymmetric. However, temporal bone alters the beam in such a way that this symmetry is lost. Thus, the beam profiles for those sensitivity fields measured through the bone samples were calculated by finding the average sensitivity along the locus of points at each distance from the beam axis.

Results

Freefield beam shape of commercial ultrasound systems

The plots of ultrasound sensitivity for the QVL 120 are illustrated in Figure 2.1. For the purposes of clarity of the figures, the sensitivity in each plane has been normalised to the maximum at that distance. In fact the maximum sensitivity at 6 cm is 46% lower than the maximum at 5 cm. The spread of the ultrasound energy over a larger area at 6 cm is apparent in the figures. There is a flatter beam profile at greater depths.

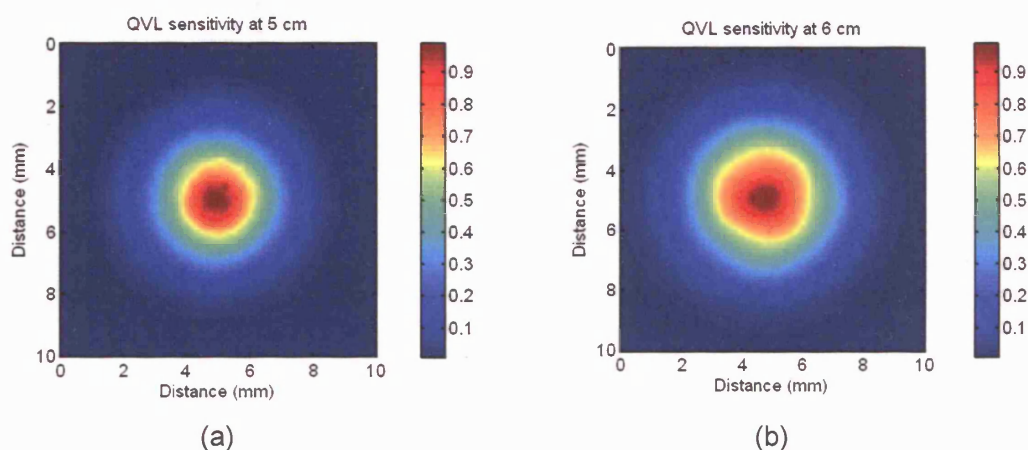


Figure 2.1 Relative sensitivity of the ultrasound field of a Scimed QVL120 2 MHz transducer at distances of 5 cm (a) and 6 cm (b) from the transducer face

Beam profiles for the QVL120 are shown in Figure 2.2. The sensitivity has now been normalised to the maximum at 5 cm from the transducer. The increased flatness and the reduction in sensitivity at 6 cm can be seen from the relative heights of the profiles. The average radius, $\overline{r_{50\%}}$, at which the sensitivity in that plane has decreased to 50% of its maximum, can be determined easily from the beam profiles. This quantity is closely related to the beam width and gives a simple comparison of different beams. It is also indicative of the degree of variation in sensitivity with distance from the beam

axis. For the QVL120 at 5 cm, $\overline{r_{50\%}}$ is 1.30 mm and at 6 cm it increases to 1.69 mm, equivalent to beam widths of 2.6 mm and 3.4 mm.

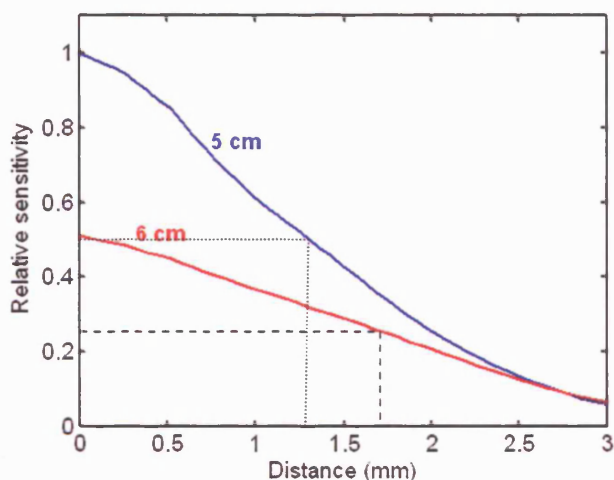


Figure 2.2 One-dimensional profile of relative sensitivity at 5 cm and 6 cm from the transducer for Scimed QVL120 TCD system with the $r_{50\%}$ distances indicated by the dotted and dashed lines, respectively

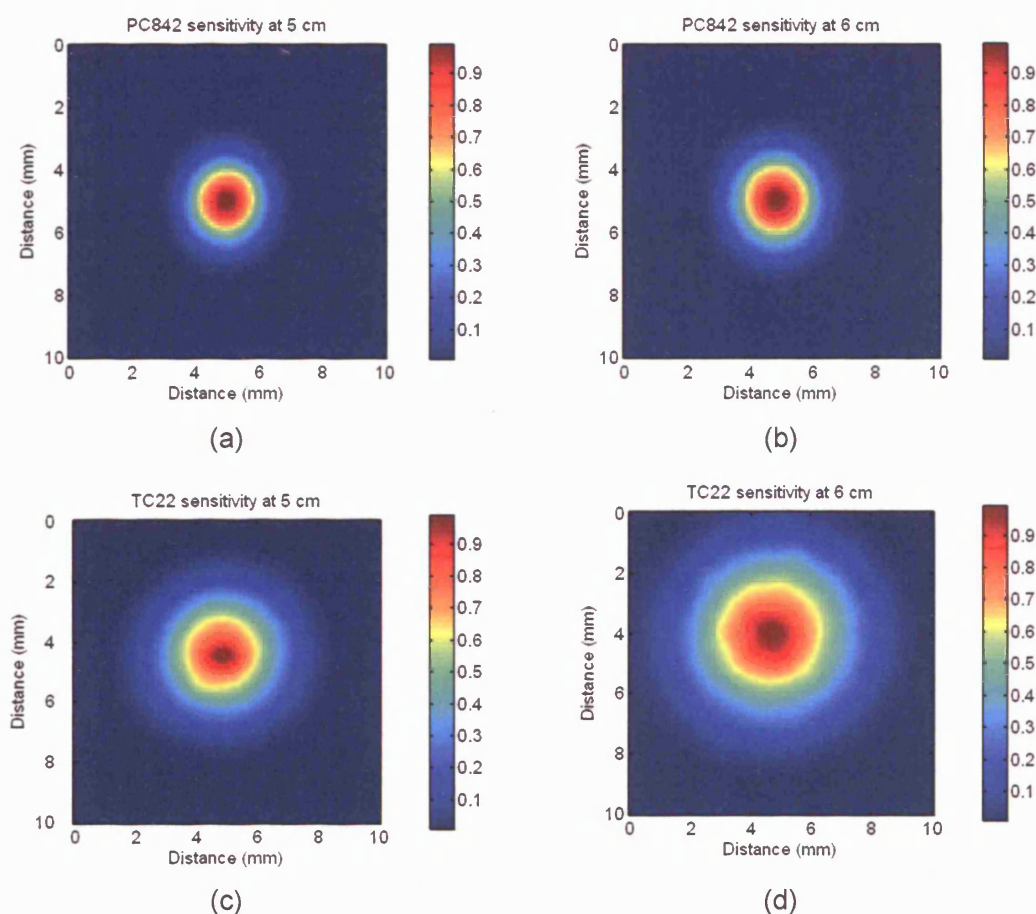


Figure 2.3 Relative sensitivity of the ultrasound field at distances of 5 cm and 6 cm from the transducer of two commercial TCD systems a Scimed PC842 (a-b) and a Scimed TC22 (c-d)

Figure 2.3 shows the two-dimensional profiles of the two other commercial systems that were investigated: a Scimed PCDop 842 and a Scimed TC22. The map of the sensitivity of the TC22 could not be centred in the same way as the QVL120 because the data were only collected over a smaller field. Figure 2.4 illustrates the beam profiles of all three systems. There are clear differences despite the apparent similarities in the systems: same manufacturer, same application, same transmission frequency and transducer diameter.

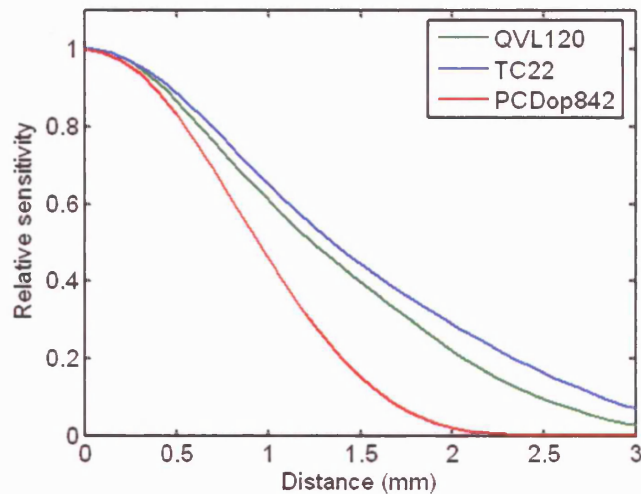


Figure 2.4 Transverse sensitivity profiles of three commercial TCD systems in a plane 5 cm from the transducer

Axial sensitivity plots of the field from these two commercial ultrasound systems were also obtained and are shown on the next page. The first, Figure 2.5, is the PCDop842. The maximum intensity occurs at about 4 cm from the transducer face. This is a weakly focussed transducer according to the Kossoff criteria (Kossoff 1979). Kossoff's criteria require knowledge of the transducer diameter, d , and radius of curvature, A , which was not available here. These parameters were, instead, estimated. The transducer housings were no more than 2 cm in diameter, meaning the crystal must be smaller than this. Therefore, $d < 2$ cm and the transition distance, $T = d^2/4\lambda$, of an equivalent flat transducer is less than 13 cm. The Kossoff definition of a weakly focussed transducer is one in which $A \geq T/2$. For $A = T/2$, the maximum intensity occurs at a distance $0.4T$ from the transducer. The focussing of the PCDop842 is close to this limit but without a better estimate of the transducer diameter it is not possible to definitively categorise it.

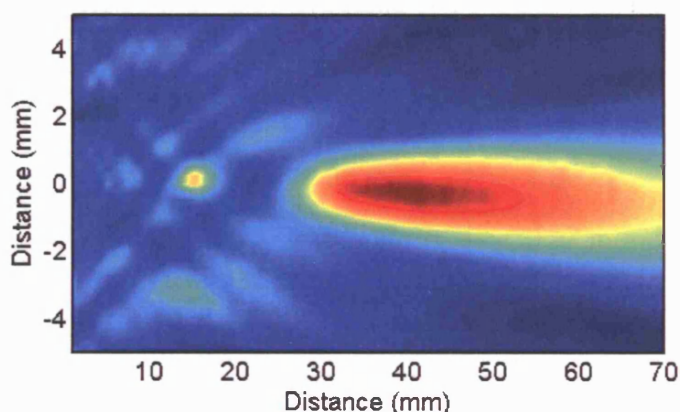


Figure 2.5 Relative sensitivity in a central plane of the ultrasound field of a Scimed PCDop842 transmitted through water

The TC22 system was more strongly focussed than the PCDop842. The axial sensitivity is shown in Figure 2.6. The appearance of the beam is smoother because the sensitivity data were sampled at more widely spaced points. The near field is also missing from the plot. However, it is still possible to determine that the maximum intensity occurs at a distance no greater than 2.5 cm from the transducer, i.e. 0.2T. From the figures in Kossoff's paper, this corresponds to a transducer with medium focussing.

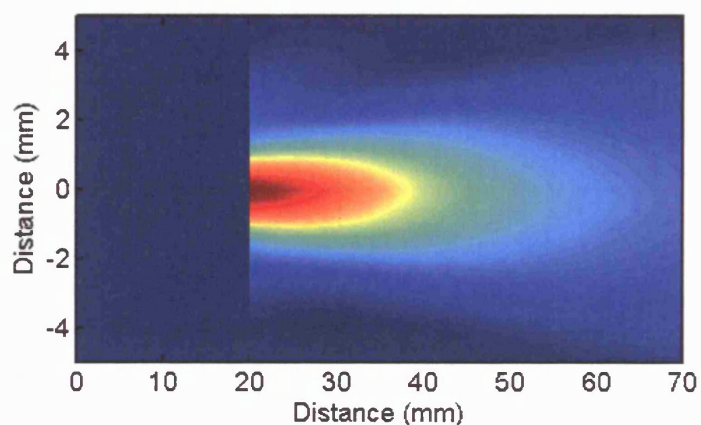


Figure 2.6 Relative sensitivity in a central plane of the ultrasound field of a Scimed TC22 transmitted through water

The values of $\overline{r_{50\%}}$ for the TC22 ultrasound beam are 1.14 mm and 1.38 mm at 5 cm and 6 cm respectively. The PCDop 842 displayed a much narrower beam at 5 cm and 6 cm ($\overline{r_{50\%}}$ of 0.80 mm and 0.97, respectively) due to a deeper focus than both the TC22 and the QVL120. The beam widths of the commercial systems are summarised in Table 2.1 below.

Table 2.1 50% beam widths measured at depths of 5 cm and 6 cm from the transducer face for three commercial, transcranial Doppler ultrasound systems using a 2 MHz transmission frequency

	$\overline{r}_{50\%}$ at 5 cm	$\overline{r}_{50\%}$ at 6 cm
QVL120	1.30 mm	1.69 mm
PCDop842	0.80 mm	0.97 mm
TC22	1.14 mm	1.38 mm

Effects of transmission through temporal bone

The overall effect of the bone was to spread the ultrasound energy over a wider area. A graphical comparison between the average beam profile for measurements through temporal bone and the beam profile for the free field is shown in Figure 2.7.

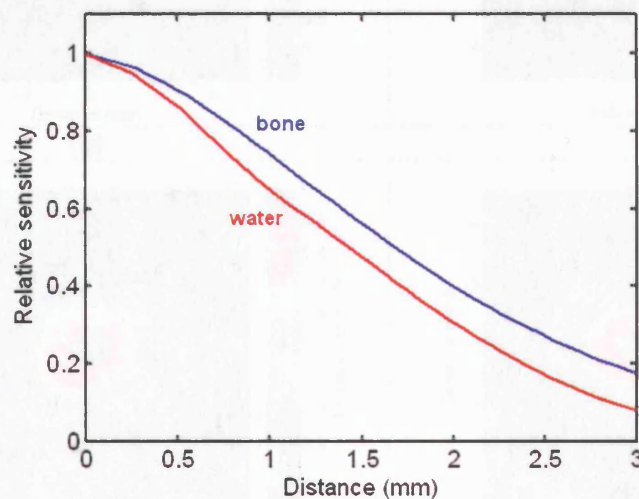


Figure 2.7 Sensitivity profiles for beam propagation through temporal bone and in the free field (propagation through water only)

The ultrasound sensitivity of the QVL120 as transmitted through temporal bone is illustrated in the eight plots of Figure 2.8. There are two plots for each bone sample: one at 5 cm from the transducer and the other at 6 cm. Again, the sensitivity for each plane has been normalised to the maximum sensitivity within that plane. Each of the bone samples had a different effect on the sensitivity, with some being more distorting than others. Samples 1 and 6 appear to be the most distorting with high levels of relative sensitivity (>0.4) at large distances – more than 5 mm – from the beam axis. The majority of the beam also seems to have been concentrated into a smaller area for bone sample 6 (at a distance of 5 cm) than for the other bone samples.

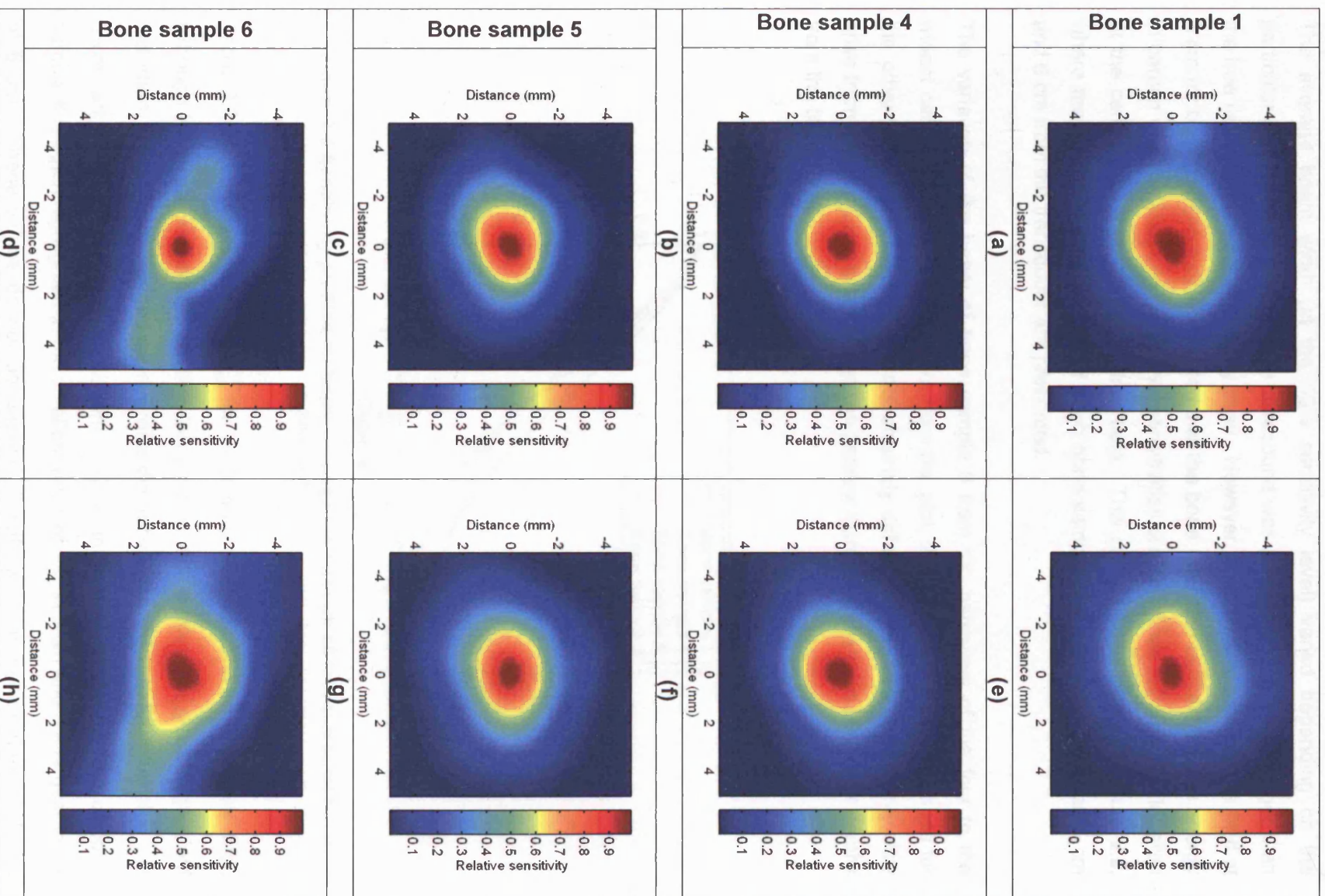


Figure 2.8 Ultrasound sensitivity at 5 cm (a-d) and 6 cm (e-h) from the transducer face after transmission through four samples of temporal bone

The average beam width (at the 50% sensitivity level) varied depending on the particular sample through which the ultrasound was propagating, but was larger than the free field measurements in every case. However, a closer inspection of the field at 5 cm for bone sample 6 demonstrates that the bone may also concentrate the energy in certain circumstances. The highest sensitivities are contained within a smaller area at the centre than they are in the free field. This can be seen below in Figure 2.9, where the average beam profiles of each bone sample over distances between 5 cm and 6 cm from the transducer are presented.

The variation of the beam of bone sample 6 from the narrowest of the four to the widest can be seen. It also appears from the plot, that the relative beam shapes for the other three bone samples are not strikingly different. Part of this similarity may arise from the averaging process and the general increase in flatness at greater depths from the transducer.

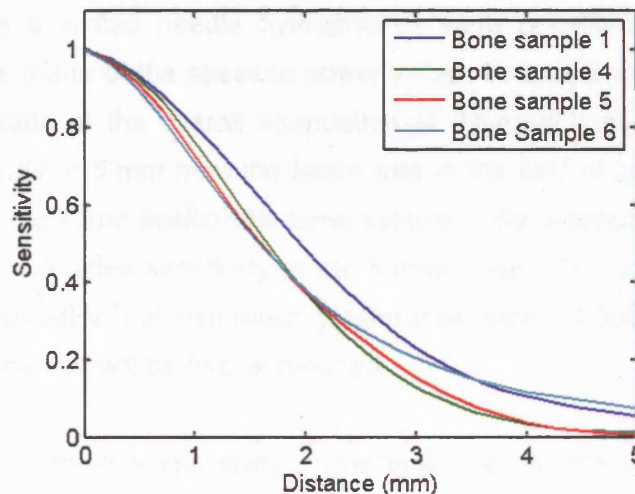


Figure 2.9 Sensitivity profiles for beam propagation through all four temporal bone samples

Table 2.2 shows the values of $\overline{r_{50\%}}$ for each bone sample. The values show that, although a visual inspection of the two-dimensional pattern suggests significant distortion, the radially averaged beam profile did not vary as much. The value of $\overline{r_{50\%}}$ at 5 cm ranged from 1.24 mm to 1.86 mm. The unusual shape of the field of bone sample 6 is again highlighted in the smallest value of $\overline{r_{50\%}}$ at 5 cm and the largest value at 6 cm. These values do not correspond directly with the values that would be estimated from Figure 2.7 as the data in the table deals separately with the sensitivity

patterns at 5 cm and 6 cm from the transducer, whereas the plot uses the average of the two planes.

Table 2.2 Values of beam width based on radial distance $\overline{r_{50\%}}$, at which the average sensitivity has dropped to 50% of the maximum for four temporal bone samples

Bone sample	$\overline{r_{50\%}}$	
	5 cm	6 cm
1	1.86	1.86
4	1.50	1.68
5	1.41	1.59
6	1.24	1.94

Discussion

Absolute measurement of the amplitude of the ultrasound pressure wave was not possible as the available needle hydrophones were uncalibrated. Therefore, no comparison was made of the absolute power values from different ultrasound systems nor was one made of the overall attenuation of different bone samples. Thus, the absolute sensitivity at 5 mm from the beam axis in the field of bone sample 6 may be less than that in the same position for bone sample 4, for example, despite there being a higher value of relative sensitivity in the former case. The attenuation of cerebral tissue ($0.8 \text{ dB}\cdot\text{cm}^{-1}\text{MHz}^{-1}$) is also much greater than water ($0.002 \text{ dB}\cdot\text{cm}^{-1}\text{MHz}^{-1}$), so *in vivo* beam sensitivities will be further reduced.

However, it is the relative sensitivity of the beam across the width of a vessel that affects the reliability of the assumption of proportionality between changes in signal power and changes in vessel diameter. In a clinical setting, absolute signal power measurements are not comparable between different patients nor between different recordings from the same patient. In the former case, this is due to the differences in physical anatomy that will influence signal power. In the latter, identical positioning of the transducer from session to session is unlikely and variations can easily occur in the position of the beam relative to the anatomical structures that lie in its path. This was seen *in vitro* where the appearance of the field was strongly dependent on the position of the transducer on the bone sample and any change in the arrangement altered the pattern of transmitted intensity.

It is presumed that the distorting effect of the temporal bone is neither predictable nor directly measurable *in vivo*; the variability of the *in vitro* sensitivity fields demonstrates the difficulty of any attempt to make such measurements. However, the modification of ultrasound beams by the skull is currently under intense investigation by researchers working in the field of high-intensity, focussed ultrasound (Aubry et al. 2003). The virtual source, time reversal techniques that they have developed are already capable of producing beams of the required shape for thermo-ablation. Such experiments use large, multi-element arrays and, thus, may not provide useful data for single-crystal, diagnostic, Doppler systems.

Sensitivity field asymmetry

Although $\overline{r_{50\%}}$ is a useful comparator of different beam widths, it gives no indication of the asymmetry of the beam. A more comprehensive index of the distortion caused by the temporal bone can be derived from the formula for the eccentricity, ε , of an ellipse

$$\varepsilon = \sqrt{1 - \frac{b^2}{a^2}} \quad \text{Equation 2.1}$$

where a is the semi-major axis and b is the semi-minor axis. ε increases with increasing eccentricity from 0 for a circle to 1 for maximum eccentricity. The pattern of ultrasound sensitivity lacks even the symmetry of the ellipse and so does not have perpendicular semi-major and semi-minor axes. Instead, r_{max} and r_{min} – the greatest and smallest radii at which the sensitivity dropped to a given percentage of the maximum sensitivity – were used and the expression of eccentricity became

$$\varepsilon' = \sqrt{1 - \frac{r_{min}^2}{r_{max}^2}} \quad \text{Equation 2.2}$$

The measure of distortion varied with the choice of the sensitivity threshold. Generally, the lower the value, the larger the distortion measured. The eccentricity of the fields for sensitivity thresholds of 75% and 50% are given in Table 2.3.

Although bone sample 6 appears the most distorted on visual inspection, most of the power of the ultrasound is concentrated at the centre – at a plane 5 cm from the

transducer the value of $\varepsilon'_{75\%}$ is the smallest of all the cases. The distortion is more clearly seen in the high value of $\varepsilon'_{50\%}$ at 6 cm.

Table 2.3 Eccentricity measures of the ultrasound field transmitted through temporal bone samples. The subscript to ε corresponds to the value of sensitivity used to determine the outline of the beam.

	5 cm		6 cm	
Bone sample number	$\varepsilon'_{75\%}$	$\varepsilon'_{50\%}$	$\varepsilon'_{75\%}$	$\varepsilon'_{50\%}$
1	0.75	0.72	0.84	0.80
4	0.57	0.66	0.55	0.66
5	0.67	0.74	0.69	0.70
6	0.50	0.70	0.78	0.87

Axial shape of sample volume

The ultrasound sensitivity maps are based solely on the measurements of the transmitted field and the assumption that the pattern of reception sensitivity will be the same. However, factors in the receiver electronics will also have influence on the shape. The axial profile of the sample volume, which is a convolution of the transmitted pulse and the length of time for which the receive gate stays open, will alter the relative contributions of planes at different distances from the transducer. Planes at the beginning and end of the range gate will have a reduced weighting relative to planes in the centre. The exact shape will depend on the relative durations of transmit pulse and receive gate. In the most extreme situation, these will be of the same duration and the axial profile will have a triangular shape as shown in Figure 2.10. It is likely that the precise axial shape of the sample volume will vary between manufacturers due to their different approaches to changing the length of the transmitted pulse for user-selected sample volume lengths. The axial sensitivity of one of the commercial systems presented in this chapter, the PCDop 842 was measured by Angell and Evans (2003) and has a similar appearance to the theoretical shape of Figure 2.10.

The power spectrum of the Doppler signal is modulated by the radially averaged beam shape. However, the two- and three- dimensional shape of the ultrasound field will determine the changes in power in response to lateral and angular offsets of the beam and vessel. A beam that spreads laterally in one preferred direction may have a sharp drop-off in power at some points, but be relatively insensitive to lateral movements along the line of spread. On the other hand, a beam shape that is concentrated in a

small area may have a reasonably flat profile across the vessel but be very susceptible to signal loss as a result of small movements away from an optimum alignment. The impact of both these factors will be considered by modelling the effect of changes in vessel diameter for many different alignments and misalignments of the ultrasound beam and model vessel.

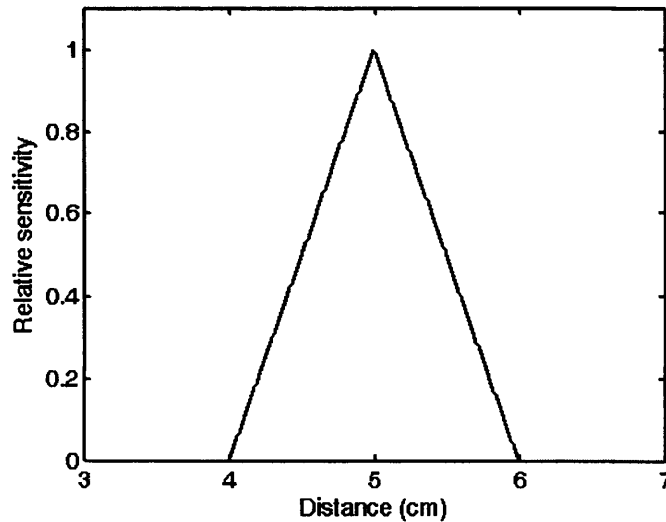


Figure 2.10 Theoretical shape of the axial sensitivity of a Doppler beam with a transmitted pulse and receive gate of the same duration

Conclusions

Commercial TCD systems have beam widths that are comparable to the diameter of the MCA. In the absence of bone, the beam width would cause a 50% variation in sensitivity across a typical vessel. *Post mortem* temporal bone samples placed in front of the transducer distorted the ultrasound field in comparison to the free field shape and, on average, increased the beam width by 20% over the free field value – effectively reducing the non-uniformity of the field. The ultrasound beam becomes asymmetric when transmitted through bone and the appearance of the field is variable in respect of different bone samples and different orientations of any one bone sample. The overall impact of transmission through bone is unpredictability in the spatial distribution of the ultrasound sensitivity. The effect that this has on the Doppler signal power will be demonstrated in the following chapters.

Chapter 3 – Numerical Model

Introduction

The programming language MATLAB (Mathworks, NY, USA) was used to create a model that could take input in the form of geometrical information about the sizes, shapes and positions of the ultrasound beam and MCA and output the power or spectrum of the Doppler signal. The sensitivity information was incorporated into the model of the interaction between a vessel and the ultrasound field. This model combined the sensitivity information from the work in the previous chapter with various vessel shapes and alignments. A more realistic vessel path was introduced through positional information based on MRI measurements of the MCA *in vivo*. The model made it possible to compute the total signal power (the sum of all the sensitivities) or the Doppler spectrum for a range of beams and vessels.

This model is a development of the work carried out by Deverson and Evans (2000a) where the effects of position on returned power were studied for a two-dimensional ultrasound field. Expanding the model to three dimensions allows consideration of the variation in ultrasound sensitivity with depth and provides an opportunity for a wider range of vessel positions and shapes to be studied.

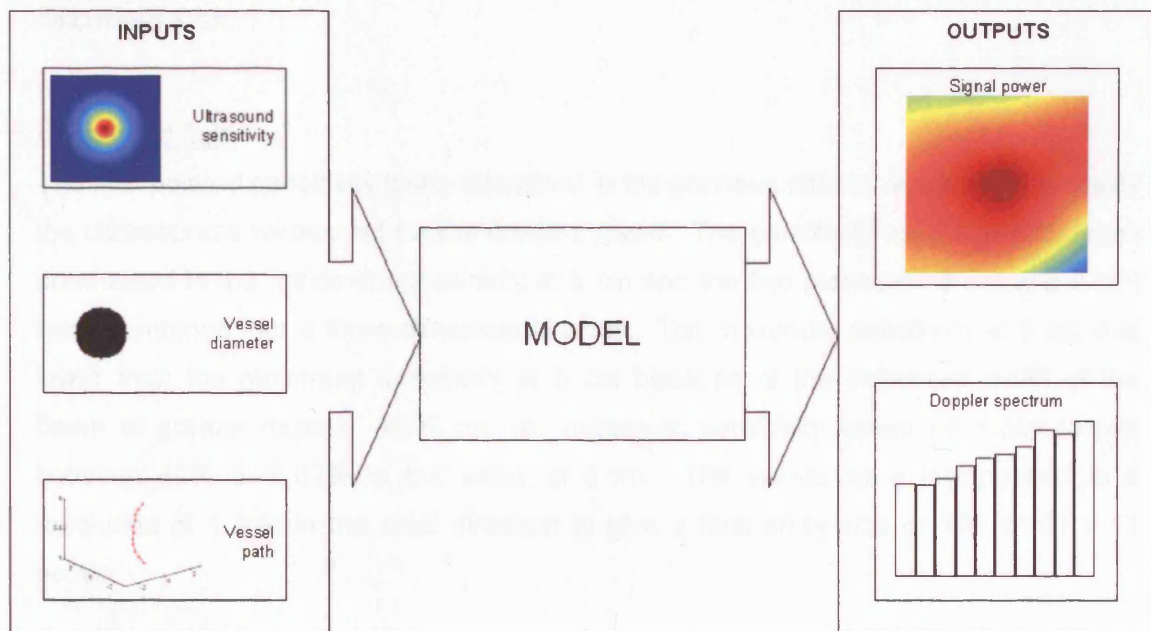


Figure 3.1 Symbolic schematic of inputs to and outputs from numerical model

Model

Assumptions

The primary assumption made in the creation of the model was that there was uniform scattering within the vessel, i.e. the proportion of the transmitted ultrasound power returned to the transducer was the same at each point in the vessel. The consequence of this assumption is that the signal power from any area depends only on the sensitivity of the field at that point. In reality, the scattering particles (blood cells) may not be uniformly distributed through the vessel. In smaller vessels blood cells concentrate in the centre, which would result in a reduced Doppler signal from the vessel periphery even if the vessel were uniformly insonated.

Physical and physiological factors that could alter the Doppler signal such as transmitted power and frequency, haematocrit and skull thickness were assumed to be unchanging. No assumptions were made in advance about the shape or size of vessels and the model had the flexibility to accommodate various vessel diameters and angles of insonation.

The velocity profile of the blood within the vessel is not relevant except that the blood is moving and, therefore, will produce a detectable Doppler signal. In chapter 5 the Doppler spectrum will be considered and the detail of the velocity profile will be discussed then.

Ultrasound field

The interpolated sensitivity fields described in the previous chapter were used to create the ultrasound environment for the model system. The sensitivity values at 6 cm were normalised to the maximum sensitivity at 5 cm and the two planes (at 5 cm and 6 cm) were combined into a three-dimensional array. The maximum sensitivity at 6 cm was lower than the maximum sensitivity at 5 cm because of the increased width of the beam at greater depths. At 6 cm, the maximum sensitivity varied from plot to plot between 49% and 62% of the value at 5 cm. The values were interpolated to a resolution of 1 mm in the axial direction to give a final array size of 101 x 101 x 11 points.

Coordinate system

The coordinates of any point in the model space are given by x , y and z . The x - and y -directions are perpendicular to the beam axis with x corresponding to horizontal

displacements and y describing vertical distance. z is parallel to the beam axis and increases with increasing depth (shown in Figure 3.2). In this it is opposite to the conventional, right handed coordinate system. The origin of the model coordinate-system is at the centre of the three-dimensional matrix of sensitivity, i.e. halfway along the sample volume length.

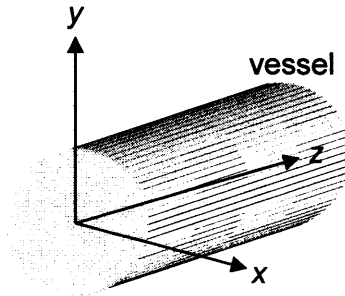


Figure 3.2 Arrangement of axes for model space, z is along the axis of the beam

Simple, straight vessel

For creating the model vessel, a three-dimensional array, $[x, y, z]$, matched in size to the arrays of sensitivity data was set up. The path of the vessel was defined by specifying the coordinates of the centre of the vessel in each of the xy -planes. A further array, D , containing the lateral distances (x_d and y_d) from the vessel centre was then calculated.

For a straight vessel, parallel to the ultrasound beam, the vessel centre lies at the same place in each plane, i.e. each plane has identical values of x_d and y_d (which will also be the same as the values of x and y if the beam and vessel are coaxial), and the cross-section of the vessel in each of the planes is circular. If R is chosen as the radius of the vessel, points will lie within the vessel when

$$\sqrt{(x_d^2 + y_d^2)} < R \quad \text{Equation 3.1}$$

and the vessel will look like a cylinder.

Angled vessel

If a non-zero angle of insonation, θ , is introduced, the position of the centre of the vessel varies with depth according to $z \tan \theta$. The vessel has an elliptical cross-section when viewed in an xy -plane and points within the vessel are defined according to

$$\sqrt{\frac{x_d^2}{R^2} + \frac{y_d^2}{\frac{R}{\cos\theta}^2}} \leq 1 \quad \text{Equation 3.2}$$

for a vessel rotated about an axis parallel to $x = 0$, or

$$\sqrt{\frac{x_d^2}{\frac{R}{\cos\theta}^2} + \frac{y_d^2}{R^2}} \leq 1 \quad \text{Equation 3.3}$$

for rotation around an axis parallel to $y = 0$. Rotations with components around both axes were not considered.

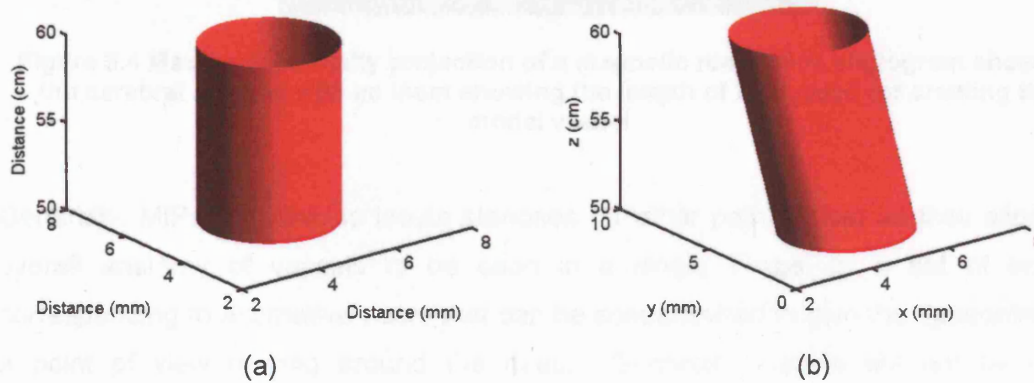


Figure 3.3 Shape of model vessel for a coaxial insonating beam (a) and for an ultrasound beam at a non-zero angle of insonation (b)

Realistic vessel paths

The model vessel described above, with its straight path, is a much-simplified version of the real anatomy of the MCA. *In vivo*, it is more likely that the MCA follows a curved path in the ultrasound beam. MR images were obtained to investigate the typical anatomies of the MCA. These images were acquired as part of the routine clinical practice for patients with suspected stroke. Clearly, in many patients confirmation of a stroke is likely and some of those cases could involve involvement of the MCA and its territory. Therefore, only those vessels where pathology was not apparent were selected for further study.

Magnetic resonance angiography

A time-of-flight technique was used to enhance the resonance signal from flowing blood. In these images, the blood appears as areas of higher signal strength because

the signal from the stationary tissues is saturated by the particular pulse sequence used. Images of transverse slices of the head were acquired with a resolution $0.4 \text{ mm} \times 0.4 \text{ mm}$ and slice thickness of 0.8 mm . A maximum intensity projection (MIP) of one dataset is illustrated in Figure 3.4.

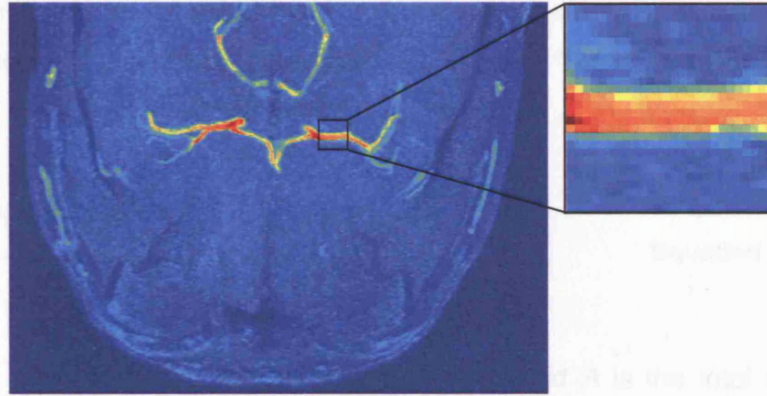


Figure 3.4 Maximum intensity projection of a magnetic resonance angiogram showing the cerebral arteries with an inset showing the length of MCA used for creating the model vessel

Generally, MIPs are used to locate stenoses (or other pathologies) as they allow the overall anatomy of vessels to be seen in a single image, or a set of images corresponding to alternative views that can be concatenated to give the appearance of a point of view moving around the head. Generally vessels will not be found exclusively in the plane of an individual, MRI slice. The first steps in producing an MIP are choosing a projection direction and segmenting the three-dimensional data into columns parallel this direction. The image can then be created by displaying the maximum pixel of each column. Single mipped images have a similar appearance to plain film angiography (although the colour scales used may be different).

MIPs were used for the initial localisation of the MCA but, as the 3-D path of the MCA was of interest, the full matrix of MR data was retained. The data were transferred from the imaging system as an 8-bit array of pixel intensity values. A volume of interest was chosen that included a reasonably straight segment of artery at a depth of approximately 5-6 cm from the skull. The volume size was chosen to match the size of the sensitivity arrays - $10 \text{ mm} \times 10 \text{ mm} \times 10 \text{ mm}$.

Vessel centre

As the MR images were not acquired specifically for the purpose of tracking the MCA path they were not optimised for this application. It was necessary to interpolate the

pixels to increase the resolution to match the ultrasound sensitivity data and post-processing was required to determine the relative centre of the vessel in each z-plane. It was decided to use the centroid of the cross-sectional area as the vessel centre. Points with intensities above 127 – the mid-point of the intensity scale – were considered to be within the vessel, so determining the shape of the area. This may exclude some slower flow, which would have a lower signal strength, but the MR images were not being used to set the vessel boundary directly. The centres in the x-, C_x , and y-, C_y , planes were calculated using the formulae:

$$C_x = \frac{\sum I(x, y) \cdot x_i dA}{A}, \quad C_y = \frac{\sum I(x, y) y_i dA}{A} \quad \text{Equation 3.4}$$

where I is the signal intensity, dA is the area of each pixel and A is the total area. Figure 3.5 shows one such vessel cross-section with the centroid marked by +. For comparison, the pixel in which the maximum signal intensity is found is marked with O.

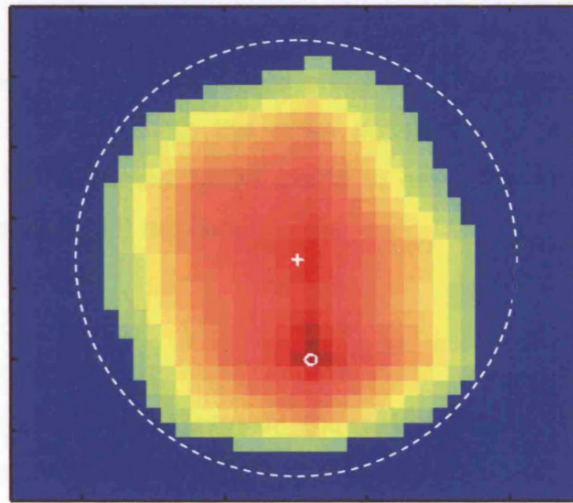


Figure 3.5 Cross-section of an MCA as seen on MRA; + indicates the centroid, O the pixel of maximum signal intensity and the dashed line indicates the circumference of a 3 mm diameter circle centred on +

The path of the real vessel was mapped in x , y and z by drawing a straight line from one centroid to the next. The matrix $[x_d, y_d, z]$ was calculated and Equation 3.1 was used to determine the limits of the vessel. Figure 3.6 shows an example of a model vessel constructed from MRI data. The path of the vessel is shown on the left and the shape of the vessel on the right. The vessel was rotated to a position that gave an average angle of insonation of 0° . The coordinates of the vessel axis (in mm) are:

$X = ($	0.4,	0.2,	0.0,	0.0,	-0.1,	0.0,	0.0,	0.1,	0.1,	0.1,	0.3)
$Y = ($	-0.5,	-0.2,	-0.1,	0.1,	0.0,	0.0,	0.1,	0.0,	0.0,	-0.3,	-0.5)
$Z = ($	-5.0,	-4.0,	-3.0,	-2.0,	-1.0,	0.0,	1.0,	2.0,	3.0,	4.0,	5.0)

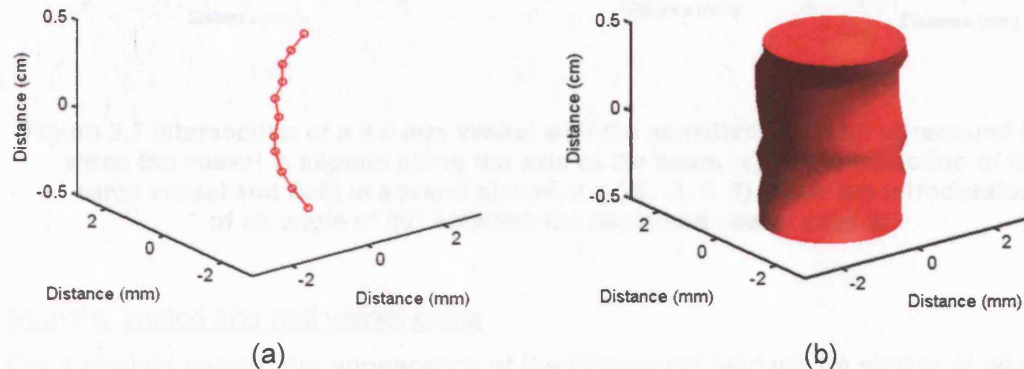


Figure 3.6 Vessel trajectory (a) of a real MCA (locus of vessel centres over a distance of 1 cm) and a model vessel (b) created along the same path

Subsequent rotations relative to the beam could be introduced to study the effect of different angles of insonation. In the initial position, vessel was assumed to be sufficiently close to being parallel to the beam to have the appearance of a circular cross-section, i.e. Equation 3.1 applied.

Vessel mask

Whichever path was chosen for the vessel, the matrix of distances, $[x_d, y_d, z]$, from the vessel centre, was converted to a logical array – true for points within the vessel and false for those outside – and applied as a mask to the beam sensitivity array. This separates out the volume of the ultrasound beam that insonates the scatterers within the vessel and, thus, contributes to the Doppler signal. Figure 3.7(a) shows a single plane of sensitivity values within a vessel of diameter 3.0 mm. Figure 3.7(b) shows a selection of slices from the sensitivity array for a vessel angled at 45° to the beam.

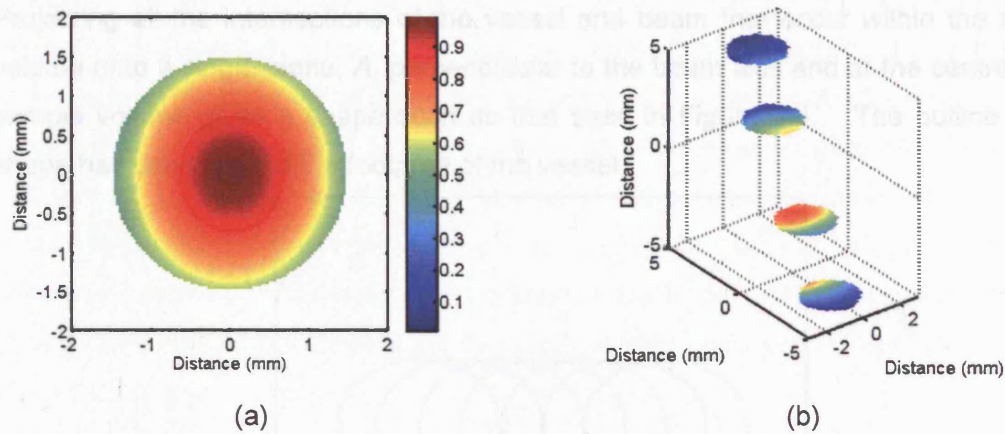


Figure 3.7 Intersection of a 3.0 mm vessel with the sensitivity field an ultrasound beam when the vessel is aligned along the axis of the beam (a) and intersection of the same vessel and field in several planes, $z = \{-5, -2, 1, 5\}$, after the introduction of an angle of 30° between the beam and vessel axes (b)

Straight, angled and real vessel paths

For a straight vessel, the appearance of the ultrasound field will be similar at all depths with differences arising only from the increasing width of the ultrasound beam. The situation is different for angled vessels and modelled vessels that follow non-straight trajectories. For these types of vessel, the position of the vessel relative to the beam centre will vary with depth and so the vessel will intersect a different part of the field at each depth. This is illustrated schematically in Figure 3.8 for a straight vessel angled with respect to the beam.

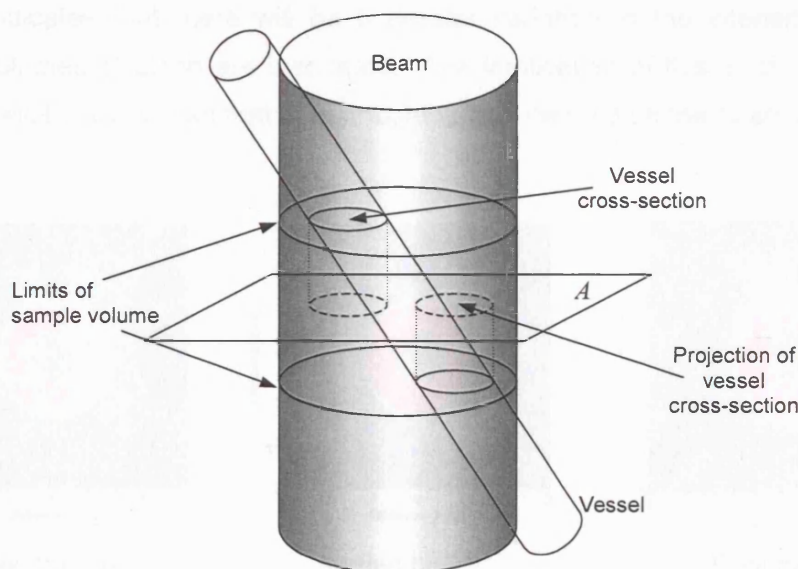


Figure 3.8 Schematic of the intersection between beam and vessel, showing the method of projecting the vessel cross-section onto a single plane at the centre of the sample volume

Projecting all the intersections of the vessel and beam that occur within the sample volume onto a single plane, A, perpendicular to the beam axis and at the centre of the sample volume gives a shape such as that seen in Figure 3.9. The outline of this shape has been termed the footprint of the vessel.

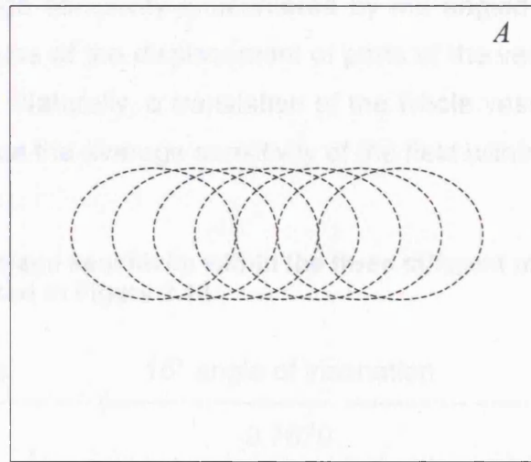


Figure 3.9 Illustration of projections onto a central plane A as demonstrated in Figure 3.8

Footprints of three types of model vessels are shown in Figure 3.10 superimposed on an ultrasound sensitivity field. A realistic vessel path will give a model vessel with a larger footprint than the straight, cylindrical vessel because of the curvature of the axis. It is a much smaller effect than that which arises out of the introduction of an angle of 15° between the vessel and the beam. The size, shape and position of the footprint indicates the areas of the ultrasound field that the vessel will intersect. A larger footprint indicates that there will be a greater variation in the intensity with which different volumes of blood are insonated. The implication of this is that the average sensitivity will be lower than that of a straight vessel centred on the beam axis.

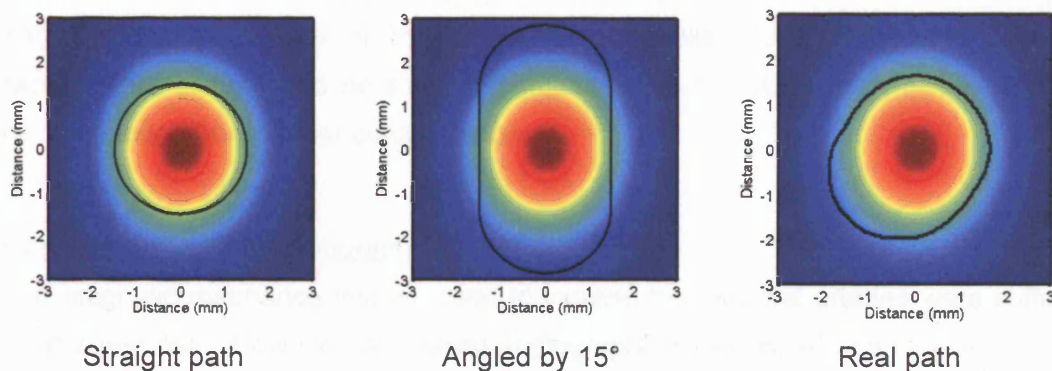


Figure 3.10 Projection of vessel outline onto a single plane of beam sensitivity data for three possible vessel trajectories. Each of the vessels had a 3.0 mm diameter.

The relative values of average sensitivity for each of the different vessel footprints is indicated in Table 3.1. This is obtained by summing the sensitivity of all the points in the volume of intersection of the beam and vessel. The sensitivity of a straight, parallel vessel centred on the beam is taken to be 1 and, again, all vessels had a diameter of 3.0 mm. The average sensitivity encountered by the angled vessel and the realistic vessel is lower because of the displacement of parts of the vessel to greater distances from the beam axis. Naturally, a translation of the whole vessel away from the beam axis would also reduce the average sensitivity of the field within the vessel.

Table 3.1 Relative average sensitivity within the three different model vessels whose footprints are illustrated in Figure 3.10

Straight vessel	15° angle of insonation	Realistic path
1.000	0.7670	0.9911

Discussion

Attenuation of blood and tissue

The additional attenuation due to scattering and absorption by tissue was not included in the model. It was assumed that the tissue through which the ultrasound passes between the transducer and Doppler sample volume was homogeneous and would not change the spatial distribution of sensitivity in the way that the temporal bone does. Ultrasound travelling within the vessel, rather than through water as for the measurement of sensitivity in Chapter 2, will also be subject to the attenuation coefficient of blood, which is approximately 0.4 dB cm⁻¹ at 2 MHz. The situation is complicated by the variable amounts of tissue in the path of a beam that encounters an angled vessel as well as the reflections from the walls of the vessel itself, but these factors were assumed to be small in comparison to the attenuation of the skull and were excluded from further consideration.

Magnetic resonance angiography

The magnetic resonance images used to localise the cerebral arteries were sufficient for this purpose. However, a detailed angiographic study would use cardiac gating to collect each slice at the same point in the cardiac cycle. The image of the vessel cross-section is made up of lines from different transverse slices and the velocity of

blood in the vessel will vary in the time interval between each slice acquisition. As the signal strength depends on the velocity the signal strength will also vary from slice to slice. This resulted in the rather asymmetric appearance of the vessel where a circular shape would be expected. It also meant that the maximum signal strength was not necessarily centred in the vessel and the resolution of the images might not be as high as possible. However, the path of the vessel could still be determined and anyway the size of the vessel is chosen by the user as one of the inputs to the model. It was, however, reassuring to see that the size of the MCA seen in the MR images was within the range of diameters chosen for study.

Real vessel shape

One of the assumptions of the model was to use a circular cross-section for model vessels following the path of a real vessel. The maximum deviation of the real vessels from a parallel, straight vessel was calculated as 7.3° . This would correspond to an eccentricity of 0.13 or a 0.8% difference in area, compared to that of a circle, in the plane perpendicular to the beam axis. This would have only a small effect both on the volume insonated and the average sensitivity of the ultrasound field at the periphery of that area. This is especially true if the deviation from a straight path only occurs over a short length of the sample volume, because averaged over the whole length the cross-sectional area will be closer to circular. However, only five vessels were studied, so it is possible that there may be greater variations in anatomy than those seen, even amongst healthy subjects.

The effect of deviations from the mean path of the vessel are not only an issue for accurate cross-sectional area calculations. They also affect the accuracy of the measured velocity. An assumption of $\theta = 0$ in the $\cos \theta$ term in the Doppler equation results in an underestimation of the velocity of flows at non-zero angles. The underestimate is greater if the overall angle of insonation is large. However, realistic vessel paths will only be considered for average angles of insonation of 0° where the errors in the cross-sectional areas and velocities are small.

High pass filtering

In reality, the limits of the vessel will be determined by the high pass filters that remove the low velocity, but high amplitude, signal from the vessel walls rather than the walls themselves. These filters will also remove a part of the flow within the vessel: the part

of the Doppler signal which falls below the cut-off frequency. It is possible to more closely match the clinical situation by calculating the relative velocity at each point within the vessel and defining the boundaries based on a velocity threshold. This effectively makes the vessel smaller than its actual diameter. The issue of high pass filters and their influence on the Doppler signal power will be discussed in more depth later.

Conclusions

A numerical model was created to calculate the returned power from a blood vessel insonated with a typical TCD ultrasound beam. This model used the three-dimensional sensitivity field measurements presented in Chapter 2 as the basis for the ultrasound beam. Flexibility built into the model and its three dimensional nature allowed the inclusion of different vessel sizes and geometries. Any choice of vessel diameter or angle of insonation could be used, although the results presented later are confined to a selection of the possible arrangements. Information collected from magnetic resonance images was used to construct model vessels with trajectories similar to those found *in vivo*. This increased the realism of the modelled interaction between beam and vessel and reduced the number of assumptions necessary to describe the MCA. These model vessel shapes will now be used to predict changes in Doppler signal power for different vessel diameters and trajectories.

Chapter 4 – Maps of Doppler signal power

Introduction

The numerical model was used to calculate Doppler signal power, P , for vessels at various locations in the ultrasound field. Using two vessels of different sizes, the power change (ΔP) for a given area change (ΔA) could also be determined at each point. In this way, the typical values of the ratio of power change to area change, $\Delta P/\Delta A$, were found for vessels in each of the sensitivity fields. When there is uniform insonation of the vessel, ΔP and ΔA are equal. Non-uniformity of the ultrasound field is indicated by $\Delta P/\Delta A \neq 1$. The effects of lateral translations and non-zero angles of insonation on the ratio $\Delta P/\Delta A$ were considered.

Method

The Doppler power for a model vessel insonated by each of the plotted ultrasound beams was calculated using the numerical model. The centre of the model vessel was translated relative to the beam in the x - and y - directions to find the returned power at different locations in the field. The resulting array, $P(x,y)$, is a map of the Doppler signal power. Maps were produced for vessels of diameters 2.0 mm, 3.0 mm and 4.0 mm in the fields of all four bone samples and in the free field. Three arrangements of the model vessel were used: a straight, cylindrical vessel aligned parallel to the beam axis, a straight vessel angled with respect to the beam and a vessel based on the path of a real MCA.

A further set of power maps was produced for vessel diameters of 1.8, 2.2, 2.7, 3.3, 3.6 and 4.4 mm, i.e. diameters 10% larger and smaller than the initial vessel sizes. Taking the power maps in pairs, e.g. the map for a 1.8 mm vessel with the map for a 2.0 mm vessel, the fractional change in power, $\Delta P(x,y)$, was calculated at each point. The fractional change in area, ΔA , for each pair of vessels was also calculated numerically. The changes in power, ΔP , were then divided by ΔA , producing a matrix of the ratio $\Delta P/\Delta A$ at the various positions. For each bone sample, there were six different combinations, corresponding to 10% increases in diameter and 10% decreases in diameter for each of the three original vessel sizes.

The values of $\Delta P/\Delta A$ were analysed to find the minimum and median values for a subset of beam-vessel positions. This subset of positions was chosen by requiring that the power returned by the original vessel be within 1 dB of the maximum for that combination of vessel and field.

Results

Power maps

The power maps are similar in appearance to the sensitivity field used in their creation. They are, effectively, the convolution of the matrices of sensitivity and the vessel mask. Figure 4.1 shows the relative returned power from a straight, 3 mm vessel in the field of bone sample 6. Each point in the map corresponds to the relative power of a vessel centred on that point.

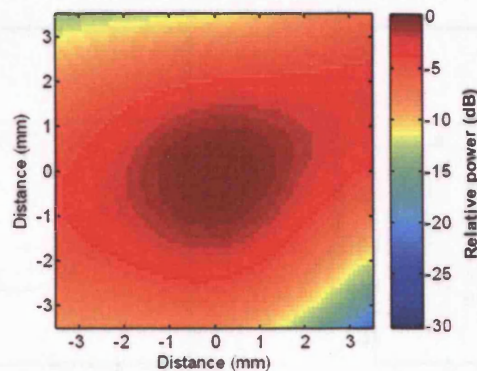


Figure 4.1 Variation in relative Doppler power returned from a 3 mm diameter vessel at various positions in the sensitivity field of bone sample 6. The x- and y- coordinates give the location of the centre of the vessel and the colour at that point indicates the relative power

In comparison, Figure 4.2 shows the power returned from 2 mm and 4 mm vessels in the same sensitivity field. The gradient of the spatial variation is reduced for larger vessel diameters. This is more clearly seen in the lower right quadrant of the figures where, for the 2 mm vessel, the relative power drops to a minimum of approximately -30dB but in the same location a 4 mm vessel returns a power greater than -20 dB.

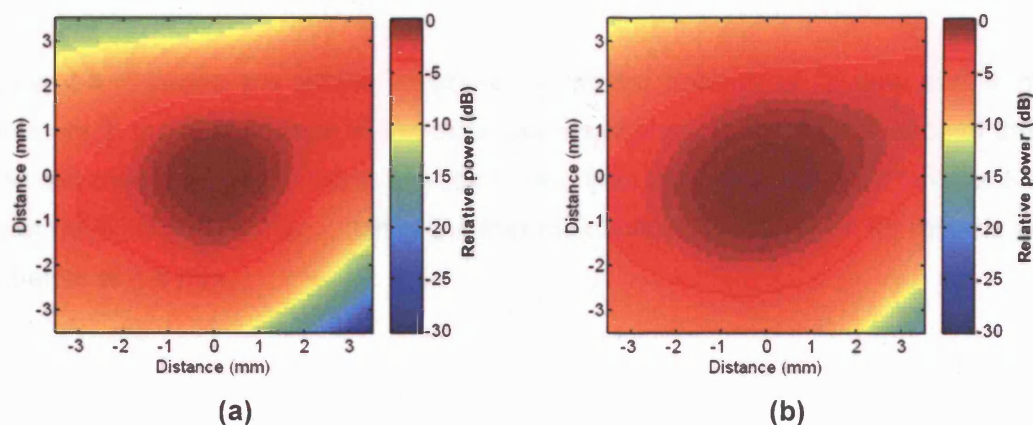


Figure 4.2 Variation in the relative Doppler power returned from a 2 mm (a) and a 4 mm (b) diameter vessel at various positions in the sensitivity field of bone sample 6

Although the illustrated power maps cover a small area, only 7 mm x 7 mm, the range of signal powers is very large – up to 30 dB. Plotting the -1, -2 and -3 dB contours emphasizes the differences between vessel sizes and sensitivity fields. Figure 4.3 presents the same data as Figure 4.2 but in the form of contour lines. It highlights the slight lateral movements that will result in significant changes in the signal power. The asymmetry of the distribution of power values is also clearly visible.

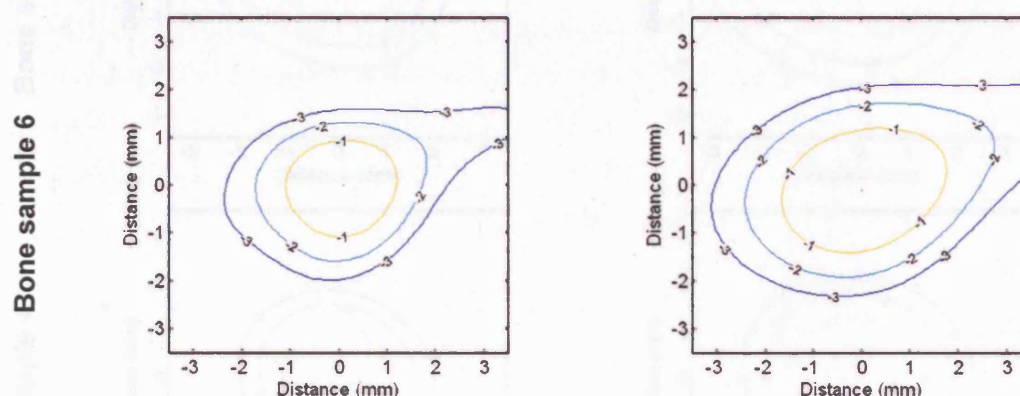


Figure 4.3 -1, -2 and -3 dB contours of relative Doppler power for 2 mm (left column) and 4 mm (right column) model vessels in the field of bone sample 6. This is an alternative presentation of the data in Figure 4.2

The contour presentation is also an appropriate way of demonstrating the differences between the fields of different temporal bone samples and the differences that result from the choice of model vessel diameter. The consequence of the larger vessel diameter is a convolution of the sensitivity field with a wider top-hat function, effectively applying a more strenuous smoothing function. This produces more widely spread contours that are at greater distances from the centre of the field.

Figure 4.4 includes the power contours for model vessels of 2 mm and 4 mm diameters in the field of each of the other bone samples. In the field of each of these bone samples, changes in beam position of less than 3 mm are sufficient to reduce the power returned to less than a half of the maximum value possible even for vessels with diameters of 4.0 mm.

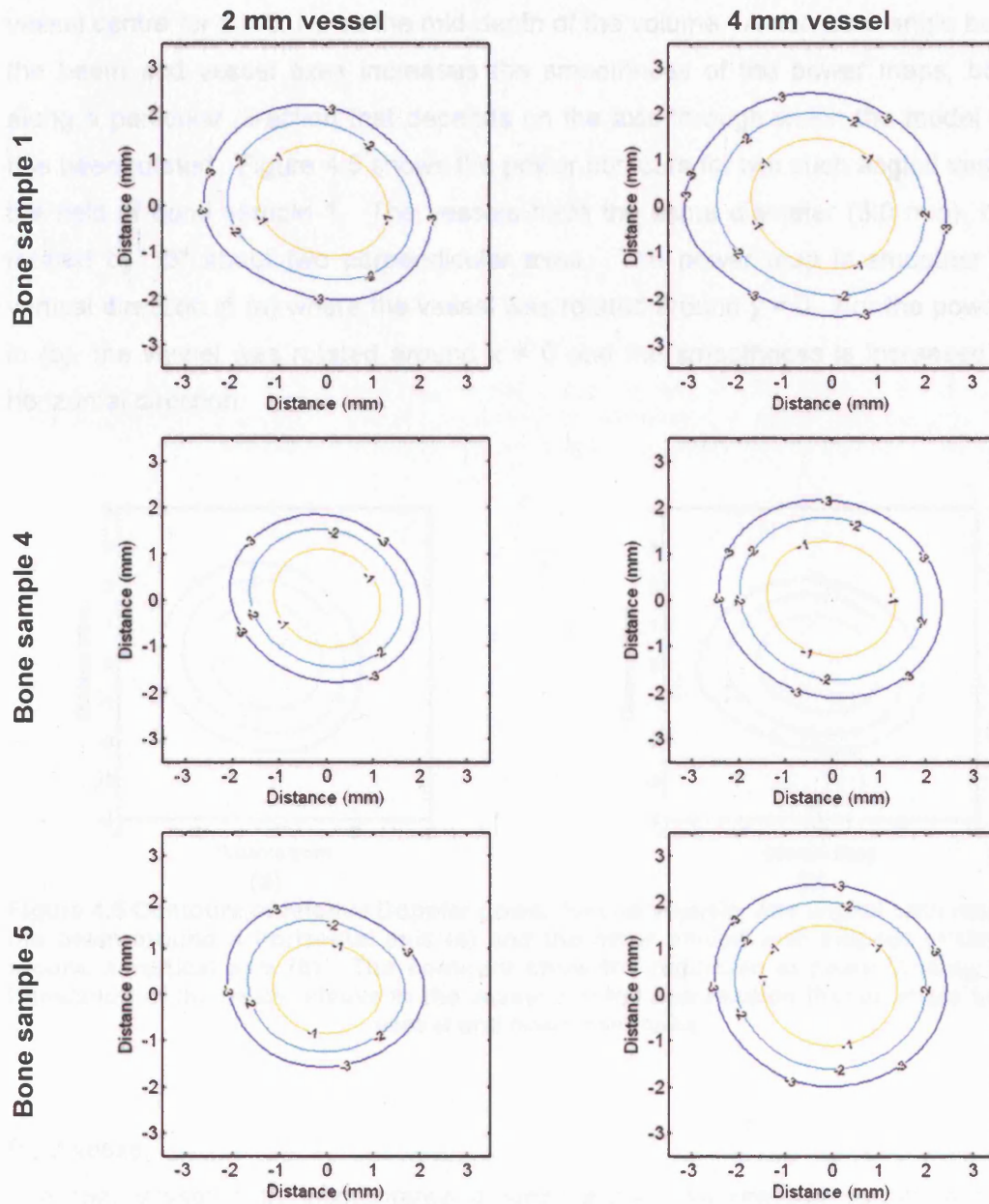


Figure 4.4 -1, -2 and -3 dB contours of relative Doppler power from a 2 mm, model vessel (left column) and a 4 mm, model vessel (right column) in the field of three different temporal bone samples

Angled vessels

The x- and y- coordinates of the centre of a vessel angled with respect to the beam will vary with depth. The power for such a vessel was assigned to the coordinates of the vessel centre for $z = 0$, i.e. at the mid-depth of the volume. A non-zero angle between the beam and vessel axes increases the smoothness of the power maps, but only along a particular direction that depends on the axis through which the model vessel has been rotated. Figure 4.5 shows the power contours for two such angled vessels in the field of bone sample 1. The vessels have the same diameter (3.0 mm), but are rotated by 15° about two perpendicular axes. The power map is smoother in the vertical direction in (a) where the vessel was rotated around $y = 0$. For the power map in (b), the vessel was rotated around $x = 0$ and the smoothness is increased in the horizontal direction.

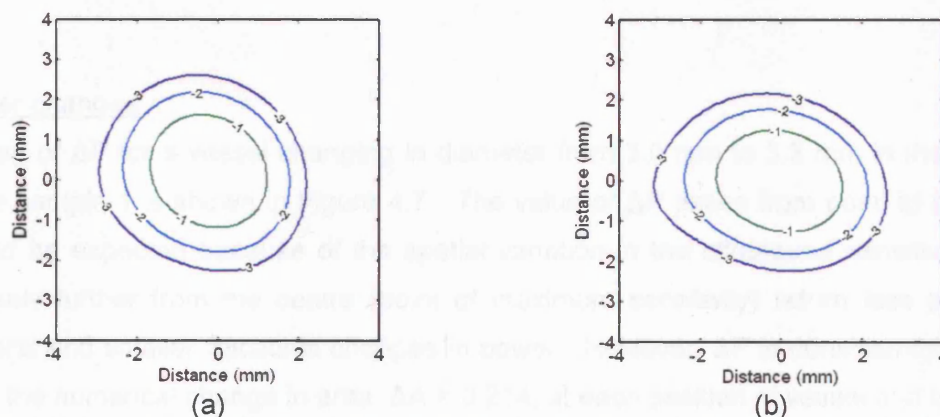


Figure 4.5 Contours of relative Doppler power for two vessels, one angled with respect to the beam around a horizontal axis (a) and the other angled with respect to the beam around a vertical axis (b). The contours show the reduction in power arising from a translation of the beam relative to the vessel and the contribution that an angle between vessel and beam can make.

Real vessel

The real vessel path incorporates a small angle between the vessel and beam although the average angle of insonation is 0° . There is a small effect on the power map, which is barely perceptible even in the power contours. Figure 4.6 combines the contours of a model vessel that follows a real trajectory and a straight, model vessel of the same diameter.

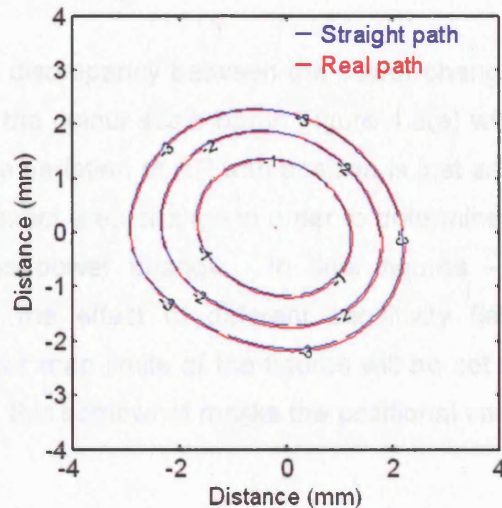


Figure 4.6 Contours of relative Doppler power for a model vessel that follows a real MCA trajectory (red) compared with a model vessel following a straight path, parallel to the beam (blue). Both vessels have a diameter of 3 mm

Power changes

A map of ΔP for a vessel changing in diameter from 3.0 mm to 3.3 mm in the field of bone sample 1 is shown in Figure 4.7. The value of ΔP varies from point to point, as would be expected because of the spatial variation in the ultrasound sensitivity field. Vessels further from the centre (point of maximum sensitivity) return less power in general and smaller fractional changes in power. However, ΔP is consistently smaller than the numerical change in area, $\Delta A = 0.214$, at each position of vessel and beam.

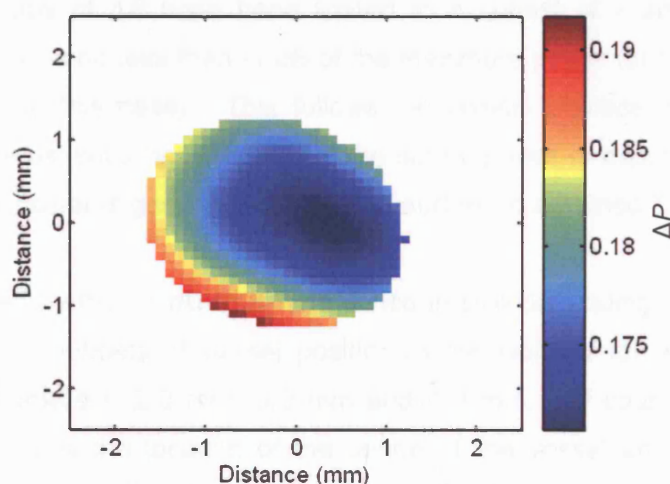


Figure 4.7 Relative change in power, ΔP , for a 10% increase in diameter of a vessel that was initially 3.0 mm in diameter

$\Delta P/\Delta A$

The magnitude of the discrepancy between the power change and the area change is more clearly seen on the colour scale bar in Figure 4.8(a) where ΔP has been divided by ΔA . The qualitative variation of ΔP with position is just as evident, but now there is no need to know the exact area change in order to determine the size of the difference between this and the power change. In later figures – for the sake of easier comparison between the effect of different sensitivity fields and different vessel trajectories – the colour map limits of the figures will be set to 0.5 and 1 as in Figure 4.8(b). Unfortunately, this somewhat masks the positional variation.

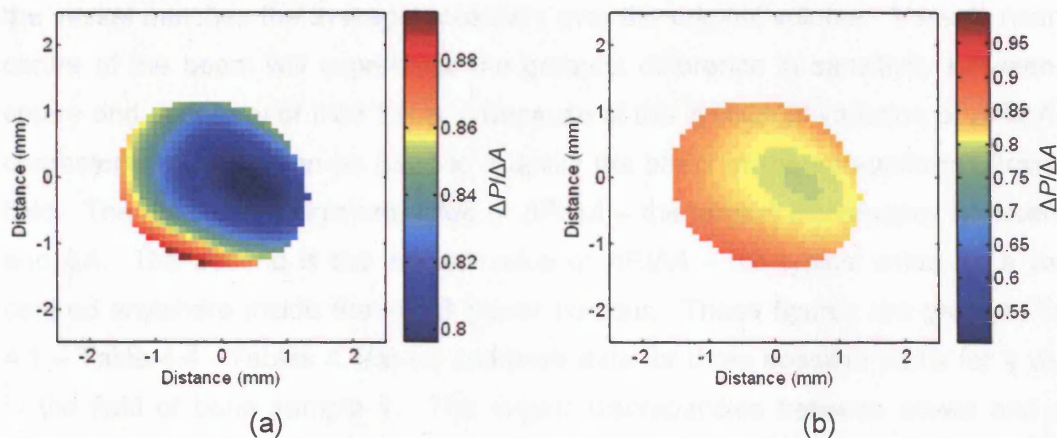


Figure 4.8 Ratio of power change to area change ($\Delta P/\Delta A$) for a 10% increase in diameter of a model vessel with an initial diameter of 3.0 mm – (a) colour scale limited by values in plot; (b) colour scale limits set at 0.5 and 1.0

The displayed maps of ΔP have been limited to a subset of x and y positions by requiring that $P(x,y)$ is no less than -1 dB of the maximum power for the original vessel diameter (3 mm, in this case). This follows the clinical practice of positioning the transducer on the patient's head such that the signal power is maximised. A drop of 1 dB in the signal power is generally considered audible to a trained TCD technician.

The area enclosed by the -1 dB threshold varied in size depending on the size of the vessel, so different subsets of vessel positions were isolated for each of the three original vessel diameters: 2.0 mm, 3.0 mm and 4.0 mm. Of course, this subset of positions restricts only the location of the centre of the vessel and the vessel itself extends beyond the -1 dB contour. Hence, the signal power is affected by the sensitivity of the ultrasound field outside this boundary.

Impact of initial vessel diameter

Using the same colour scale for all the plots of $\Delta P/\Delta A$, makes the impact of different initial vessel diameters more apparent. The limits of the colour scale were set to 0.5 and 1. This covers the full range of $\Delta P/\Delta A$ values arising from the different combinations of vessel sizes and sensitivity fields. Larger vessels have smaller minimum values of $\Delta P/\Delta A$ but the limitation of the calculations to vessel positions near the centre of the beam meant that $\Delta P/\Delta A$ never exceeded 1.

Variation of $\Delta P/\Delta A$ with position

The values of ΔP are dependent on the gradient of the sensitivity over the vessel or, more specifically, how closely the sensitivity in the region added to or subtracted from the vessel matches the average sensitivity over the original volume. Vessels near the centre of the beam will experience the greatest difference in sensitivity between the centre and periphery of their lumen. Because of this positional variation of $\Delta P/\Delta A$ two characteristic values can be used to quantify the effect of the non-uniform ultrasound field. The first is the minimum value of $\Delta P/\Delta A$ – the largest discrepancy between ΔP and ΔA . The second is the median value of $\Delta P/\Delta A$ – the typical value for a vessel centred anywhere inside the -1 dB power contour. These figures are given in Table 4.1 – Table 4.4. Tables 4.1(a)-(c) comprise data for three possible paths for a vessel in the field of bone sample 1. The largest discrepancies between power and area occur for the straight, coaxial beam and vessel, but there is little difference between these figures and those for a realistic vessel path. In comparison, introducing an overall angle of 15° between the vessel and beam axes reduces the discrepancy in every case.

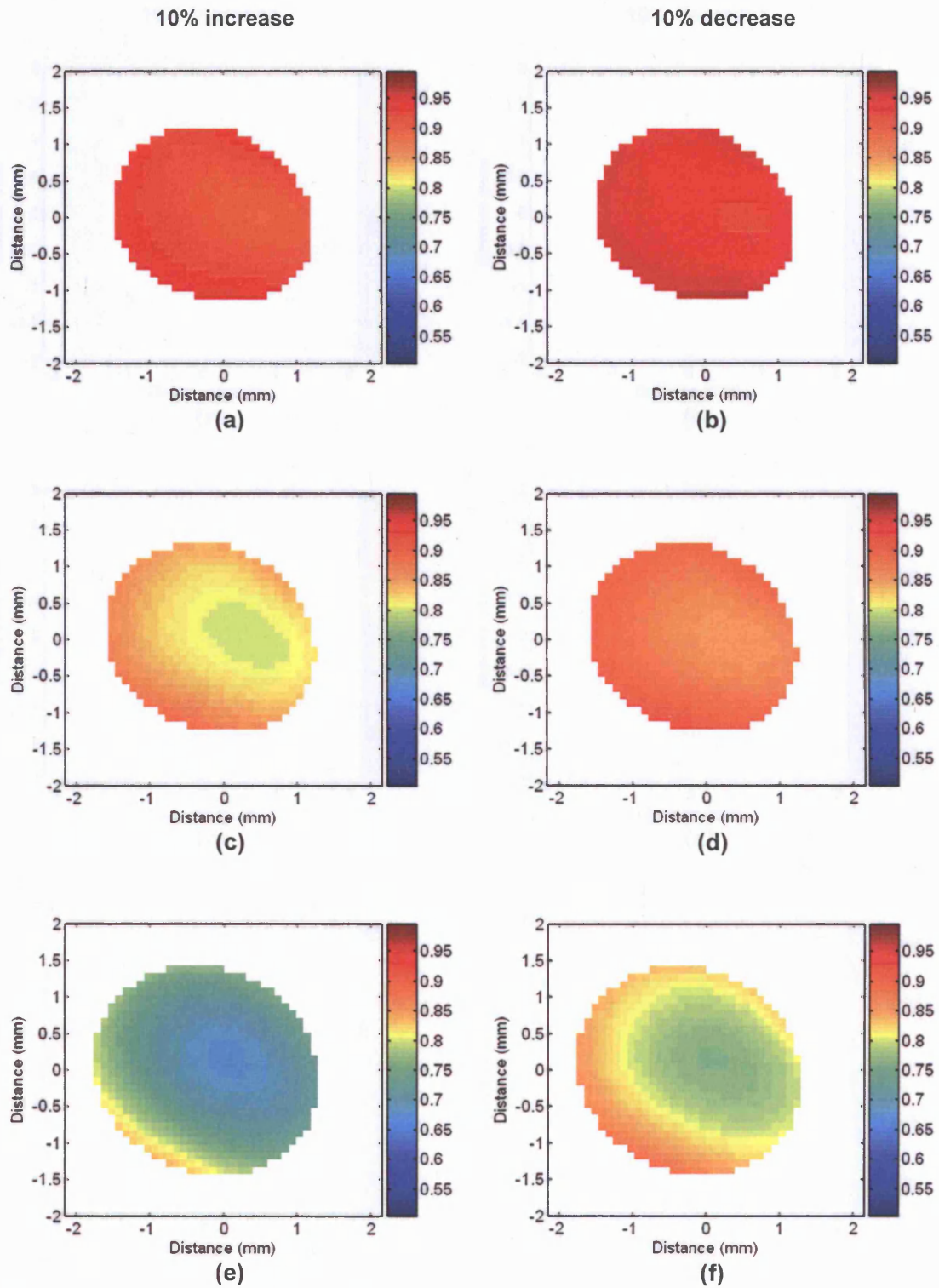


Figure 4.9 $\Delta P/\Delta A$ maps for a 10% increase (a, c, e) or 10% decrease (b, d, f) in diameter of a model vessel of diameter 2.0 mm (a, b), 3.0 mm (c, d) or 4.0 mm (e, f) following a realistic path in the field of bone sample 1

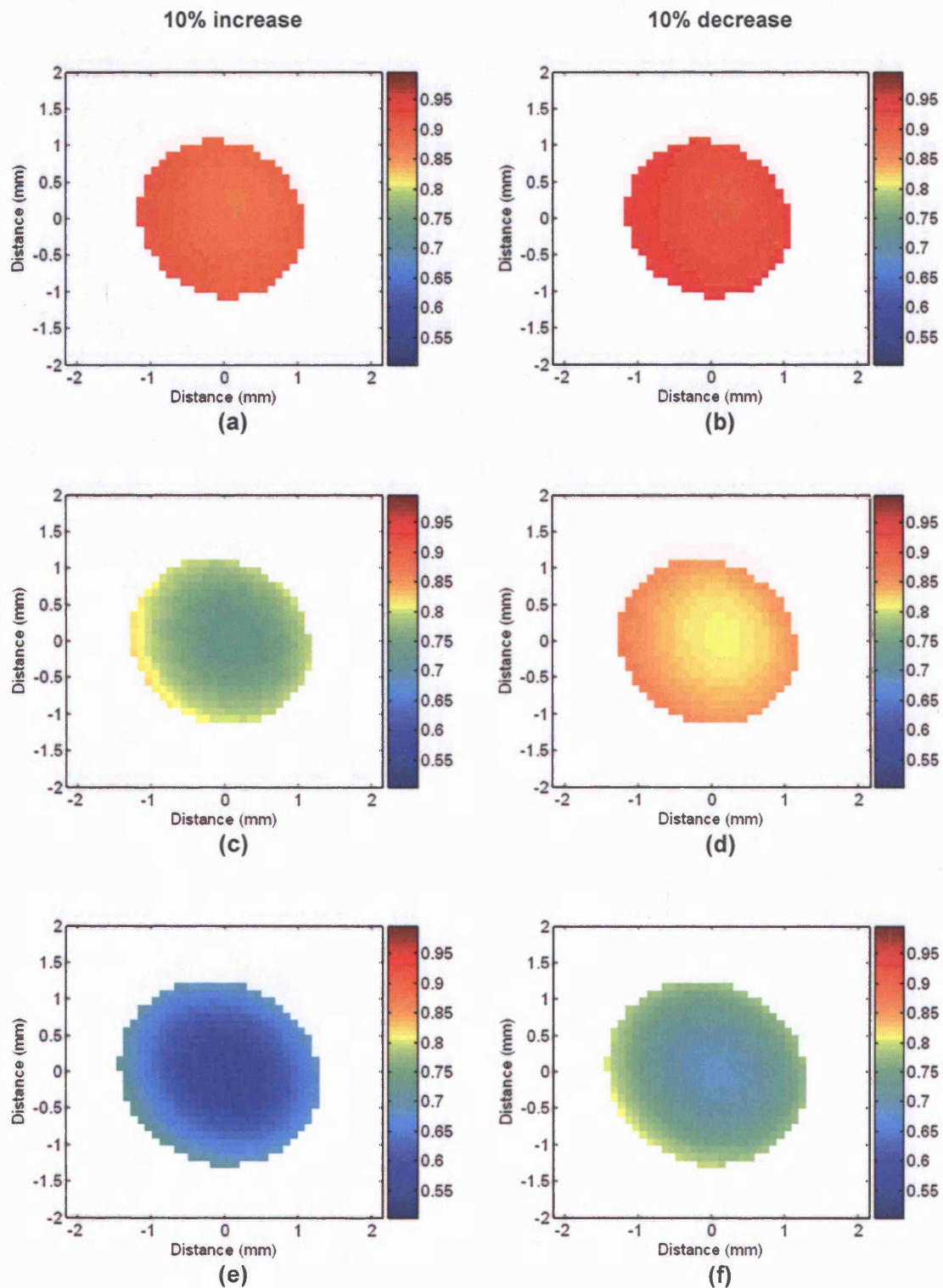


Figure 4.10 $\Delta P/\Delta A$ maps for a 10% increase (a, c, e) or 10% decrease (b, d, f) in diameter of a model vessel of diameter 2.0 mm (a, b), 3.0 mm (c, d) or 4.0 mm (e, f) following a realistic path in the field of bone sample 4

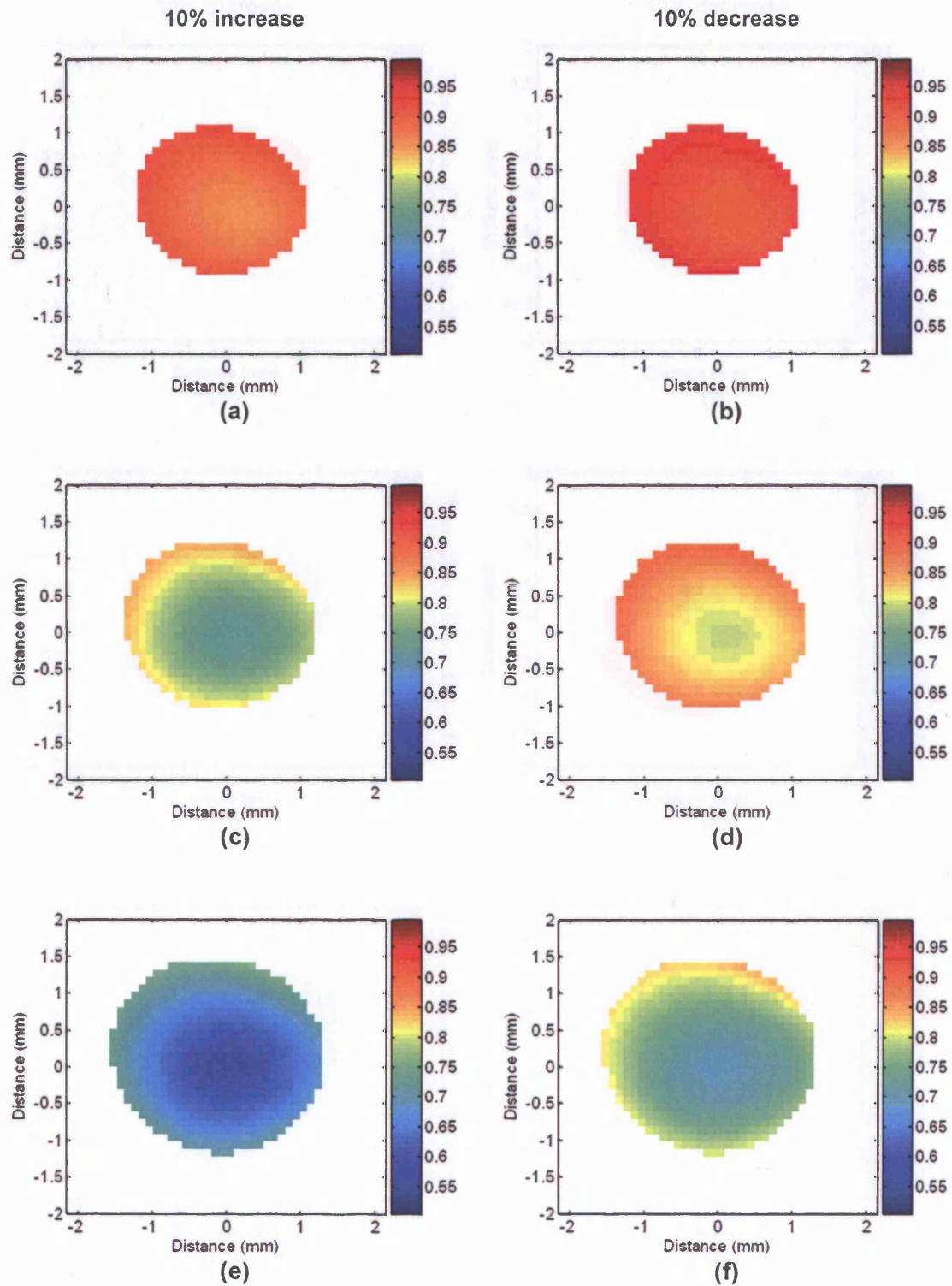


Figure 4.11 $\Delta P/\Delta A$ maps for a 10% increase (a, c, e) or 10% decrease (b, d, f) in diameter of a model vessel of diameter 2.0 mm (a, b), 3.0 mm (c, d) or 4.0 mm (e, f) following a realistic path in the field of bone sample 5

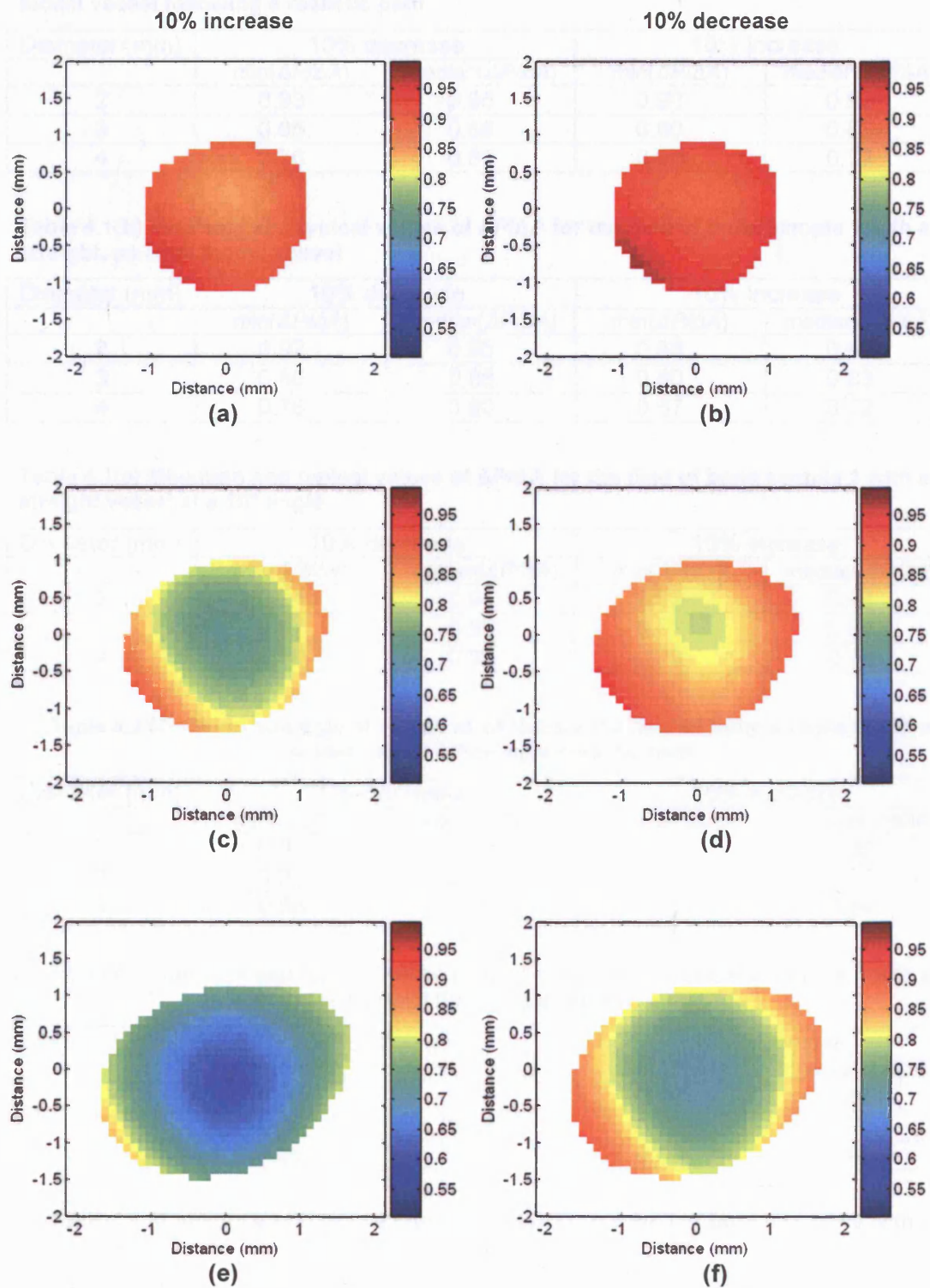


Figure 4.12 $\Delta P/\Delta A$ maps for a 10% increase (a, c, e) or 10% decrease (b, d, f) in diameter of a model vessel of diameter 2.0 mm (a, b), 3.0 mm (c, d) or 4.0 mm (e, f) following a realistic path in the field of bone sample 6

Table 4.1(a) Minimum and typical values of $\Delta P/\Delta A$ for the field of bone sample 1 with a model vessel following a realistic path

Diameter (mm)	10% decrease		10% increase	
	min($\Delta P/\Delta A$)	median($\Delta P/\Delta A$)	min($\Delta P/\Delta A$)	median($\Delta P/\Delta A$)
2	0.93	0.95	0.90	0.92
3	0.85	0.88	0.80	0.83
4	0.76	0.80	0.68	0.72

Table 4.1(b) Minimum and typical values of $\Delta P/\Delta A$ for the field of bone sample 1 with a straight, co-axial model vessel

Diameter (mm)	10% decrease		10% increase	
	min($\Delta P/\Delta A$)	median($\Delta P/\Delta A$)	min($\Delta P/\Delta A$)	median($\Delta P/\Delta A$)
2	0.92	0.95	0.89	0.92
3	0.85	0.88	0.80	0.83
4	0.76	0.80	0.67	0.72

Table 4.1(c) Minimum and typical values of $\Delta P/\Delta A$ for the field of bone sample 1 with a straight vessel at a 15° angle

Diameter (mm)	10% decrease		10% increase	
	min($\Delta P/\Delta A$)	median($\Delta P/\Delta A$)	min($\Delta P/\Delta A$)	median($\Delta P/\Delta A$)
2	0.94	0.95	0.92	0.93
3	0.87	0.89	0.82	0.84
4	0.78	0.81	0.70	0.74

Table 4.2 Minimum and typical values of $\Delta P/\Delta A$ for the field of bone sample 4 with a model vessel following a realistic path

Diameter (mm)	10% decrease		10% increase	
	min($\Delta P/\Delta A$)	median($\Delta P/\Delta A$)	min($\Delta P/\Delta A$)	median($\Delta P/\Delta A$)
2	0.91	0.92	0.87	0.89
3	0.81	0.84	0.73	0.77
4	0.68	0.74	0.58	0.64

Table 4.3 Minimum and typical values of $\Delta P/\Delta A$ for the field of bone sample 5 with a model vessel following a realistic path

Diameter (mm)	10% decrease		10% increase	
	min($\Delta P/\Delta A$)	median($\Delta P/\Delta A$)	min($\Delta P/\Delta A$)	median($\Delta P/\Delta A$)
2	0.90	0.92	0.86	0.87
3	0.79	0.84	0.72	0.78
4	0.69	0.76	0.60	0.66

Table 4.4 Minimum and typical values of $\Delta P/\Delta A$ for the field of bone sample 6 with a model vessel following a realistic path

Diameter (mm)	10% decrease		10% increase	
	min($\Delta P/\Delta A$)	median($\Delta P/\Delta A$)	min($\Delta P/\Delta A$)	median($\Delta P/\Delta A$)
2	0.89	0.92	0.85	0.89
3	0.79	0.85	0.73	0.79
4	0.70	0.78	0.61	0.70

Discussion

Power maps

Larger vessels smooth the sensitivity profile more than smaller vessels do. The -1 dB power contour will enclose a larger area if the power from a larger vessel is being considered. The particular distribution of sensitivity in the ultrasound field also affects the size and shape of the contours. For coaxial beams and vessels, one dimensional profiles, such as those shown in Chapter 2, indicate the average sensitivity for each part of the vessel. However, these profiles do not give any indication of the effect that off-axis movements or non-zero angles of insonation will have.

Vessel diameter changes

$\Delta P/\Delta A$ is a clear, concise indicator of the effects that non-uniform insonation has on the Doppler signal power. It can be used to compare the influence of difference sizes or shapes of vessels as well as different beams. Under the condition of uniform insonation, $\Delta P/\Delta A$ is always 1. A ratio less than 1 indicates that the change in power underestimates the change in area, while $\Delta P/\Delta A > 1$ implies that the change in power overestimates the change in area.

A well-aligned beam and vessel means ultrasound sensitivity that is lower at the periphery of the vessel than at the centre and any change in area will be underestimated by a measurement of the change in power. This is shown in the results presented. In no case did the value of $\Delta P/\Delta A$ equal or exceed unity. In the worst case, $\Delta P/\Delta A = 0.58$. Typically, $\Delta P/\Delta A$ was 0.83 ± 0.08 , i.e. the change in power was $17 \pm 8\%$ less than the change in area.

The ratio of power change to area change varies not only by position, but also by vessel diameter and direction of change in vessel diameter. Smaller vessels have a ratio closer to unity because the sensitivity of the field at the periphery of the vessel is more similar to the sensitivity at the centre than is true for large vessels. The change in power for a decrease in vessel size is also closer to the change in area than an increase because the sensitivity of an annulus lying just inside the vessel is higher than the sensitivity of an annulus just outside the vessel, at least for those vessels that are positioned near the centre of the ultrasound beam.

By including points down to -3 dB of the maximum power, beam/vessel arrangements with significantly poorer alignments are introduced. In this arrangement, vessels may be centred at positions ≥ 2 mm from the centre of the ultrasound sensitivity and it is

possible for the average sensitivity at large radii to exceed the sensitivity at the centre of a vessel, as shown in Figure 4.13.

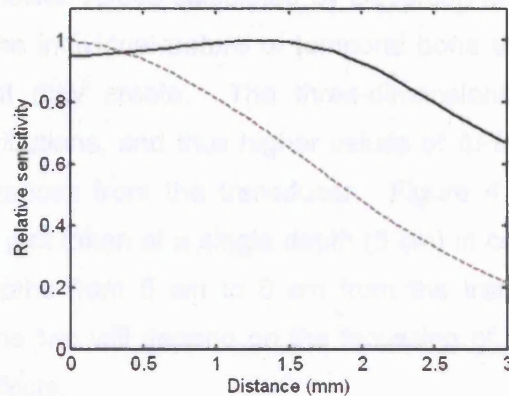


Figure 4.13 Radial variation in sensitivity for a vessel centred at a distance of 2 mm from the beam axis (solid line) compared with a vessel centred on the beam axis (dashed line)

These extended plots include values of $\Delta P/\Delta A > 1$, for example the plot shown in Figure 4.14. Therefore, it is possible for poorly aligned transducers to overestimate a change in vessel area. Transducer positions also exist where the changes in power exactly match changes in area. The locations of these vary with vessel diameter, magnitude and direction of diameter change and ultrasound sensitivity and cannot be predicted nor directly detected *in vivo*.

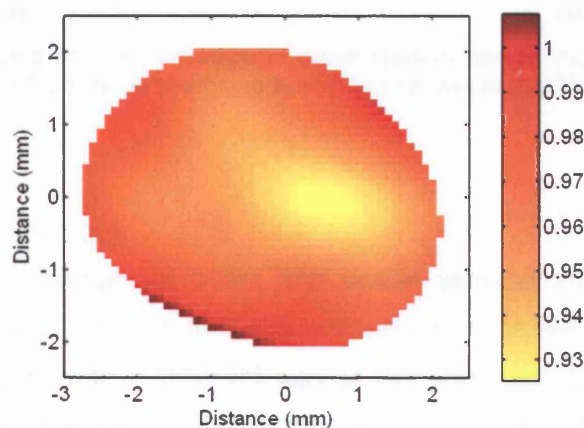


Figure 4.14 $\Delta P/\Delta A$ for vessels centred further from the beam axis. This plot contains all vessel locations where the returned power is no more than 3 dB below the maximum

Deverson and Evans (2000b) used a two-dimensional model to study power and area changes. They also found that the minimum values of $\Delta P/\Delta A$ occurred close to the centre of the ultrasound field with values ranging from 0.35 to 2.0 for beams propagating through temporal bone samples. The extremes of this range were not

seen in this work. Higher values were excluded by focussing only on those locations that returned power within 1 dB of the maximum whereas Deverson and Evans included points down to 25% of the maximum. This work found a minimum value of $\Delta P/\Delta A$ of 0.58. The lower values calculated by Deverson and Evans may have been missed because of the individual nature of temporal bone samples and the distorted ultrasound fields that they create. The three-dimensional model also results in smoother power distributions, and thus higher values of $\Delta P/\Delta A$, because of the wider beam at greater distances from the transducer. Figure 4.15 shows the difference between a sensitivity plot taken at a single depth (5 cm) in comparison to the average sensitivity for the depths from 5 cm to 6 cm from the transducer. The amount of difference between the two will depend on the focussing of the ultrasound beam and any temporal bone effects.

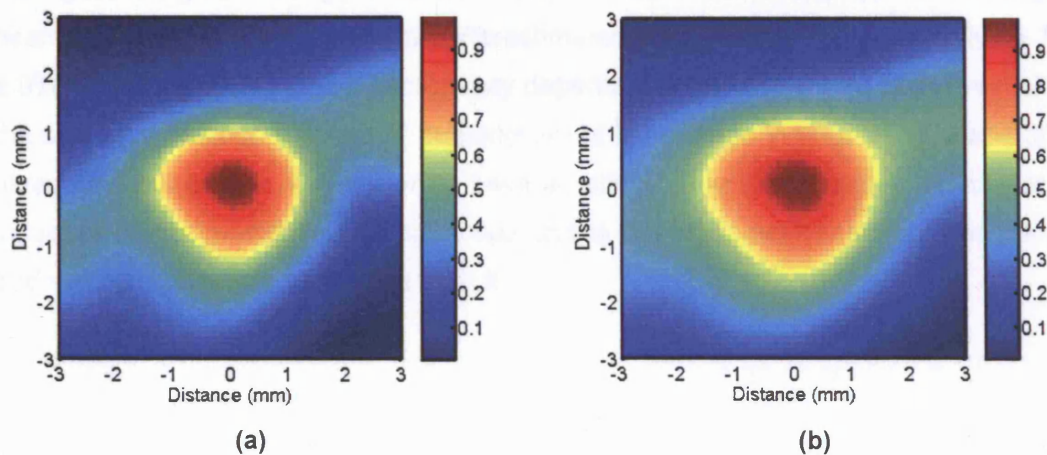


Figure 4.15 Sensitivity plot of an ultrasound beam transmitted through bone sample 6 at a single depth (a) 5 cm from the transducer and (b) averaged from 5 cm to 6 cm

Symmetry of position changes

The relative position changes of beam and vessel assume that the shape of the ultrasound field remains constant. In reality, movement of the transducer would mean interaction of the beam with a different part of the skull and a changed pattern of ultrasound sensitivity. It was previously mentioned, in Chapter 2, that the shape of the beam depended not only on the bone sample itself, but also the exact position of the transducer on the bone. Thus, any movement of the transducer creates a new, unpredictable configuration of non-uniformity. However, for monitoring of changes in blood flow or flow velocity it would be expected that the transducer would be left *in situ*, and this would not be an issue.

Of course, in practice, even an estimate of the pattern of ultrasound sensitivity will not be available although efforts to achieve this are being made in the field of high-intensity, focussed ultrasound as mentioned in Chapter 2. The data presented in this chapter simply indicate a level of variation that may arise in general. Later chapters will consider a possible method for determining, from information contained within *in vivo* Doppler signals, a quantitative indication of the amount of non-uniform insonation present.

Conclusions

Through modelling of simulated vessels and ultrasound beams, it was shown that non-uniform insonation could have a significant effect on the size of the change in power arising from a given change in vessel cross-section. It was found that for well-aligned beams the power change always underestimated the area change – typically by 17% \pm 8%. The magnitude of the discrepancy depended on the initial size of the vessel and the size and direction (dilation or constriction) of the change in area. The shape of the ultrasound beam was also shown to have an effect. The next chapter will look at the influence that non-uniform insonation has on the Doppler power spectrum and the flow and velocity indicators calculated from it.

Chapter 5 – Production of spectra using the numerical model

Introduction

Although previous chapters have dwelt almost exclusively on the total power of the Doppler signal, it is more common for TCD systems to display the power as a function of frequency (or velocity) and time, i.e. as a sonogram. In addition, users of TCD are more likely to be interested in the velocity of the blood rather than its reflectivity. However, blood within the MCA does not move with a unique velocity, instead it complies with an approximately parabolic profile in which the cells at the centre of the vessels move fastest. If there is uniform insonation of the vessel, the power spectrum is effectively a histogram of the number of ultrasound scatterers travelling at each velocity. A spatial variation in ultrasound sensitivity combined with the spatial distribution of velocities will produce a modulation of the Doppler spectrum. This modulation will, of course, affect any additional parameters that may be derived from the spectrum such as the intensity weighted mean velocity, V_{IWM} , or flow index, FI .

The numerical model introduced in Chapter 3, which was used in Chapter 4 to produce power maps based on ultrasound sensitivity fields, could also be used to calculate spectra for vessels within those fields. The model assumes a constant, but unknown, transmitted ultrasound frequency, so these are not strictly spectra in the sense of distributions of power density as a function of frequency, $p(f)$. The 'spectra' are actually intra-vessel distributions of power as a function of velocity, $p(v)$. For the sake of simplicity, and relying on the direct proportionality between velocity and Doppler frequency, the term spectrum will be used to describe both $p(f)$ and $p(v)$.

One of the assumptions stated previously was that there was uniform scattering of the Doppler signal at all points within the vessel. This also applies for the calculation of the spectra so that, once again, it is only the sensitivity of the ultrasound field at each location in the vessel that controls the contribution to the signal power that comes from the scatterers in that area.

Method

Calculating velocities

Much of the method was followed as described in Chapter 3. The construction of the vessel mask was the same as for the calculations of Doppler signal power. The main difference was the introduction of the velocity information required to produce a

spectrum. The velocity matrices were determined from the distance matrices in accordance with a parabolic velocity profile:

$$v(r) = V_{MAX} \left(1 - \frac{r^2}{R^2} \right) \quad \text{Equation 5.1}$$

where V_{MAX} is the maximum velocity, r is the distance from the centre of the vessel and R is the radius of the vessel.

A parabolic profile is a characteristic of fully developed, steady flow and fits well the pattern of flow in the part of the MCA that is studied using TCD. By choosing $V_{MAX} = 1$, relative velocities – rather than absolute velocities – were calculated. This greatly simplified later analysis and processing of the results.

Sorting to velocity bins

For each beam and vessel position, the vessel mask was applied as for the power and the velocities of the scatterers were calculated for all points within the vessel boundary. A set of equally spaced velocity intervals, v_i , was defined and the points were assigned to the appropriate bin based on the velocity of blood at that location. Then, the sensitivity values for all the points in each bin were summed and normalised to the maximum. This gave the spectrum, $p(v)$.

Producing spectra

Spectra were calculated at the same points that were used, in previous chapters, to determine the total Doppler power. Figure 5.1 shows a vessel divided into five segments based on evenly spaced velocity intervals from 0 to V_{MAX} . In practice, when calculating the power spectra a larger number of intervals than this would be used, but restricting the number displayed in the figure to five allows for clearer visualisation of the annuli. The array superimposed on the vessel indicates the points at which the calculations are made. The representation of the array spacing, 100 points per mm^2 , in the figure is accurate for a vessel diameter of 2 mm. The points would appear 50% closer for a 4 mm vessel. As with the total signal power, spectra were calculated for different ultrasound fields and for various vessel sizes and trajectories.

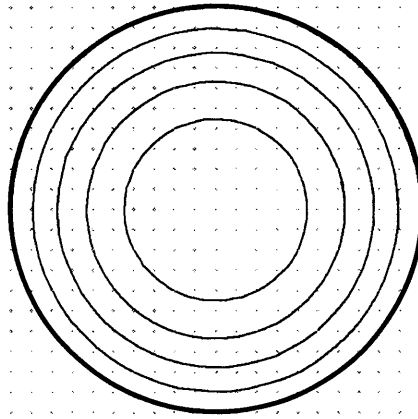


Figure 5.1 Calculation points (at a resolution of 100 points/mm²) superimposed on a 2 mm model vessel cross-section divided into five equal velocity areas. In practice, spectra were produced using at least ten velocity intervals.

Intensity weighted mean velocity

The intensity-weighted mean velocity, V_{IWM} , was also calculated for each of the spectra:

$$V_{IWM} = \frac{\sum_i p(v_i) \cdot v_i}{\sum_i p(v_i)} \quad \text{Equation 5.2}$$

where $p(v_i)$ is the total Doppler power from all scatterers with velocities in velocity interval v_i .

The ratio of the intensity-weighted mean velocity to the maximum velocity, V_{IWM}/V_{MAX} , is one parameter that can be used to indicate the degree of non-uniformity present in the spectrum. Uniform insonation of parabolic flow should mean $V_{IWM}/V_{MAX} = 0.5$. As the weighting of the velocity bins changes with the non-uniformities of the ultrasound field, V_{IWM}/V_{MAX} will have different values. Lower weighting of the slower velocities – reduced ultrasound sensitivity at the periphery of the vessel – will cause the ratio to increase, and vice versa. The numerical model was used to produce a map of V_{IWM}/V_{MAX} that could show the positional variations in the ratio.

However, even under conditions of uniform insonation the filters of the receiver circuitry of the ultrasound system will alter the value of V_{IWM} and, thus, the ratio V_{IWM}/V_{MAX} . Such filtering is used *in vivo* to remove the signal from the vessel walls, which are generally slower moving than the blood but would dwarf the blood signal because of their much greater reflectance. Estimates of the ratio of the size of echoes from tissue relative to those from blood range from 40 dB (Brands et al. 1995) to 100 dB (Heimdal and Torp 1997). Versions of the spectra modified to simulate the effect of high-pass filtering on the value of V_{IWM} were also produced.

A simple function, $w(v)$, was used to reduce the weighting of the lower velocity components.

$$w(v) = \frac{v/V_{MAX}}{0.2} \quad \forall v/V_{MAX} < 0.2$$

$$= 1 \quad \forall v/V_{MAX} \geq 0.2$$

Equation 5.3

The elimination of the lowest velocity bins causes V_{IWM}/V_{MAX} to exceed 0.5 even for a uniformly insonated vessel. Non-uniform insonation that gives greater weighting to the highest velocity signals – a well-aligned vessel and beam – will also increase the ratio V_{IWM}/V_{MAX} . Both of these influences – non-uniform insonation and high pass filtering – tend to increase the value of V_{IWM}/V_{MAX} but smaller variations in V_{IWM}/V_{MAX} will depend on the exact configuration of the inhomogeneities in the ultrasound sensitivity field.

Results

The nature of parabolic flow means that dividing the flow into equal velocity intervals is the same as dividing the vessel into annuli of equal areas. Therefore, uniform insonation of a vessel with uniform scatter will result in a power density that is the same at all frequencies, i.e. the spectrum is rectangular. Figure 5.2 shows the modelled spectrum for uniform insonation of a vessel. The small variation in the power of different frequency components is due to quantization error from the numerical determination of the annular areas. The power density has been normalised to the mean height of the bins.

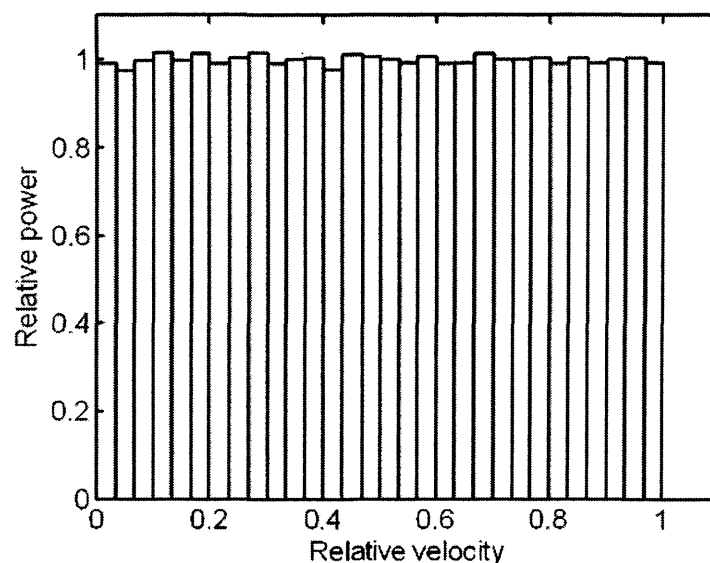


Figure 5.2 Modelled power spectrum for uniform insonation of a vessel with a parabolic blood flow profile. The spectrum shows the predicted rectangular shape.

In contrast, a spectrum from a non-uniformly insonated vessel will show evidence of the spatial variation in ultrasound sensitivity. An example of one of the spectra produced by the model is shown in Figure 5.3. This example has used a 3 mm diameter vessel with a straight path along the beam axis and a sensitivity field as measured through bone sample 1. The power from the outermost annulus is approximately 60% of the power from the central region. V_{IWM}/V_{MAX} for this spectrum was 0.533 and is indicated on the plot by the vertical red line. The spectrum on the right of the figure shows the same spectrum, but with the added effects of the high pass filter described by Equation 5.3. The lower velocity bins are reduced in power and V_{IWM} is consequently increased.

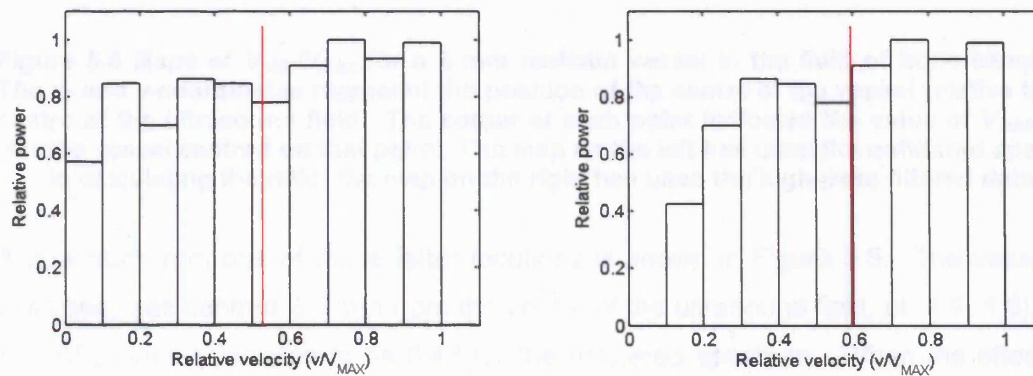


Figure 5.3 Power spectra calculated using the numerical model for a 3 mm diameter vessel centred in the field of bone sample 1. The spectrum on the right has had the effects of high-pass filtering applied to it, but is otherwise the same as the one on the left. The red line indicates the ratio of the intensity weighted mean velocity to the maximum velocity, V_{IWM}/V_{MAX} , and is 0.53 for the unfiltered spectrum and 0.59 if filtered.

The total power of the Doppler signal depends on the average ultrasound sensitivity within the sample volume: an effect of the average sensitivity rather than its specific distribution; the power spectrum shape is affected more by the spatial variation of the sensitivity field. Furthermore, the bigger the vessel is, the larger the sensitivity variation that may be encompassed by it. Vessels closer to the beam axis will also have a more striking modulation of their spectra than those at greater distances where the ultrasound power has dwindled and the variation in sensitivity is not so great. Figure 5.4 shows a map of the ratio V_{IWM}/V_{MAX} for different displacements of the beam with respect to the vessel. This example used a vessel with a realistic path in the field of bone sample 1.

As in the case of total Doppler power, the discrepancy between the calculated value of V_{IWM}/V_{MAX} and the expected value is large when the beam and vessel are best aligned. The ratio V_{IWM}/V_{MAX} approaches 0.5 away from this point and subsequently exceeds it

as more extreme displacements of the vessel with respect to the beam axis are considered.

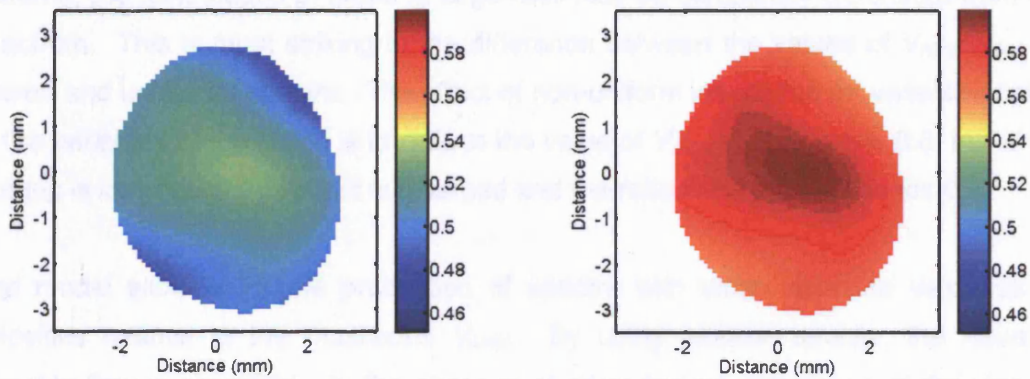


Figure 5.4 Maps of V_{IWM}/V_{MAX} for a 3 mm realistic vessel in the field of bone sample 1. The x- and y-coordinates represent the position of the centre of the vessel relative to the centre of the ultrasound field. The colour at each point indicates the value of V_{IWM}/V_{MAX} for the vessel centred on that point. The map on the left has used the unfiltered spectra in calculating the ratio, the map on the right has used the high-pass filtered data.

A spectrum from one of those latter locations is shown in Figure 5.5. The vessel, in this case, was centred 2.5 mm from the centre of the ultrasound field, at (1.9, 1.6), and V_{IWM}/V_{MAX} was calculated to be 0.48 for the unfiltered spectrum. When the effects of high-pass filtering were added, this ratio increased to 0.55.

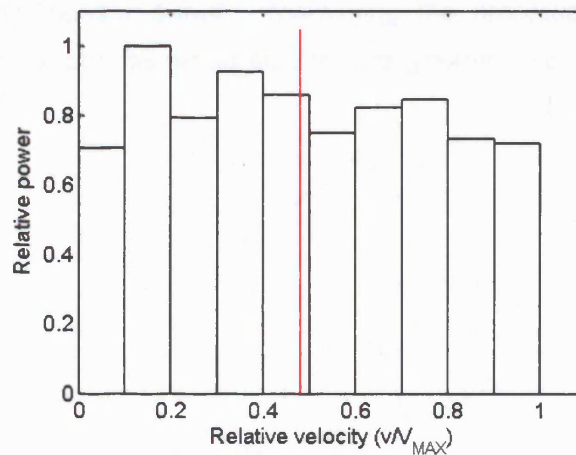


Figure 5.5 Spectrum calculated for a 3 mm vessel centred 2.5 mm from the beam axis in the field of bone sample 1. The coordinates of the vessel centre were (1.9, 1.6). V_{IWM}/V_{MAX} was 0.48 for the unfiltered spectrum and 0.55 for the high-pass filtered spectrum (not shown).

Discussion

The Doppler spectrum is more noticeably affected by certain frequency (velocity) dependent characteristics of the TCD system – such as filters in the receiver circuitry –

than is the total power. These attributes have a smaller effect on the overall power of the Doppler signal than they have on particular components of that signal. In the extreme, the contribution of blood at large radii may be completely eliminated from the spectrum. This is most striking in the difference between the values of V_{IWM}/V_{MAX} for filtered and unfiltered spectra. The effect of non-uniform insonation for vessels located at the periphery of the beam is to reduce the value of V_{IWM}/V_{MAX} to below 0.5, but when filtering is introduced this effect is reversed and the ratio once again exceeds 0.5.

The model allowed for the production of spectra with either absolute velocities or velocities relative to the maximum, V_{MAX} . By using relative velocity, the issue of pulsatile flow is simplified. In the absence of other factors, the shape of the velocity profile and relationship of V_{MAX} and V_{IWM} to each other remain the same during the cardiac cycle, although the absolute values of velocity change. This point will be returned to in later chapters that further consider the *in vivo* sonogram.

The number of bins and their widths were determined by a trade-off between velocity resolution and the partial area effects that introduce errors in the height of the columns. Figure 5.6 shows, in detail, the positions of the calculation points relative to a series of annuli (determined by dividing the vessel into areas of equal velocity intervals). The resolution of the calculation matrix is too low to accurately determine the average sensitivity of many, narrow annuli. Increasing the resolution of the points could increase the accuracy, but this would also require greater processing time.

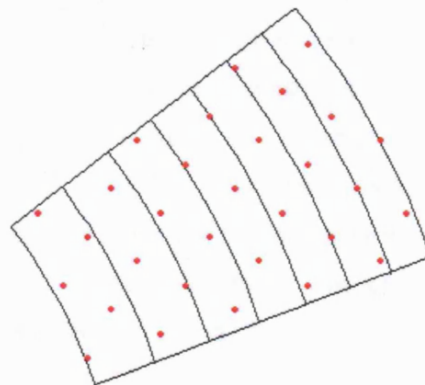


Figure 5.6 A close up of Figure 5.1 showing sectors of equal velocity divisions with calculation points (in red). An arbitrary number of velocity intervals and an arbitrary calculation matrix resolution were used in creating this figure.

A doubling of the resolution in the model leads to at least a four-fold increase in the processing time. Computing speed is, of course, always increasing. With the

computers available towards the end of this project, calculation time for the power maps had reduced to approximately 15 minutes for each combination of vessel and beam. At a resolution of 400 points per mm^2 , it would take of the order of an hour to produce each power map.

The alternative approach is to divide the vessel into a smaller number of annuli. The spectra in Figure 5.7 illustrate the difference between using 10 annuli and 20 annuli. The narrowest annuli – those at the largest distances from the centre – have the largest errors associated with the determination of their area. This can be seen in the variation in the heights of the bars for the lowest velocities in Figure 5.7(b).

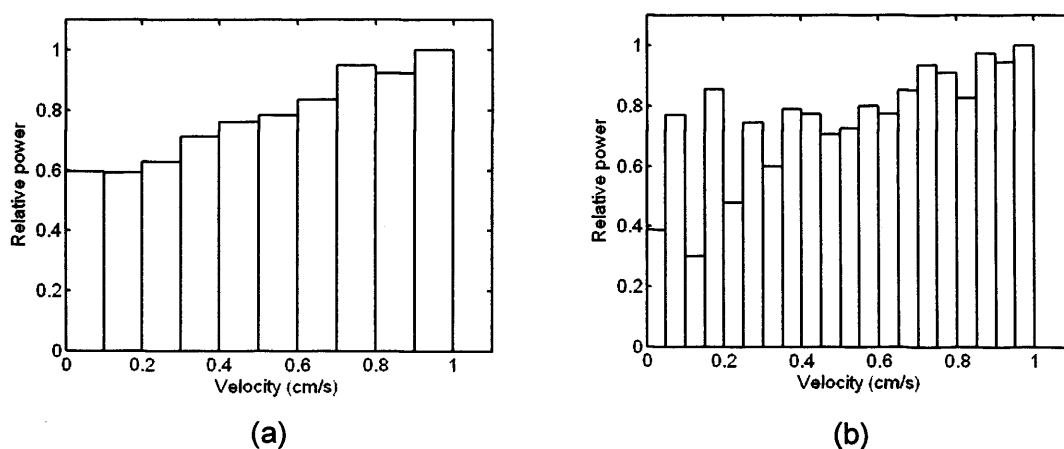


Figure 5.7 Spectrum of a 4.0 mm vessel centred in the field of bone sample 1 showing the difference between a small number (a) and a larger number (b) of velocity intervals (frequency bins)

In vivo, the number of velocity intervals in a spectrum depends on the number of points in the Fourier transform that was used to process the audio signal. Greater frequency resolution can be obtained by increasing the number of points, but only through the loss of temporal information. For the modelled power spectra the trade off was between velocity resolution and inaccuracies in the power density due to partial area effects. As the number of annuli increased, the calculation points became less representative of the annulus as a whole and the calculated power value became less reliable.

ISB

Another feature of the spectrum that was ignored by the model is the effect of spectral broadening which occurs due to the finite beam width and the shape of the vessel. It

was shown in the MR images in Chapter 3, that the MCA is not always a straight vessel. Curvature of the vessel can add to the range of maximum velocity measurements due to the $\cos \theta$ term in the Doppler equation. This was demonstrated *in vitro* by Balbis et al. (2004).

Variation in V_{MAX} with insonation depth

It may not be accurate to assume a single value for V_{MAX} along the whole length of the intersection between vessel and beam. It was shown by Hart and Haulszkiewicz (2000), that V_{MAX} reduces for shallower insonation depths, i.e. for more distal sections of the MCA. This is most likely due to the loss of flow into branch vessels and also the curvature of the vessel, which causes an apparent reduction in velocity due to the angle of insonation.

Conclusions

The effects of spatial non-uniformities in the ultrasound field are clearly visible in spectra produced by numerical modelling of the interaction between a real beam and a simulated MCA. The spectral power density visibly decreases from high velocities to low velocities. As the assumption of uniform scattering was maintained in this chapter, this is purely an effect of the reduced ultrasound sensitivity at the periphery of the vessel. A more complex modelling of the red blood cell distribution within narrow vessels would show greater decreases in power at low velocities as the cells have a lower density at the vessel periphery. In common with the investigation of total signal power, it was found that the differences between the modelled spectra and those expected under uniform insonation depended on the position and size of the model vessel. However, the characteristics of the TCD receiver electronics, such as the high-pass filters, have a larger effect on the shape of the sonogram than non-uniform insonation has.

Chapter 6 – *In vitro* flow phantom recordings

Introduction

It is apparent from the data presented in Chapter 2 that uniform insonation of a vessel the size of the MCA is impossible with commercial ultrasound systems, even in the absence of bone. An *in vitro* experiment was set-up to demonstrate that the non-uniformity of the field was manifest in the Doppler spectrum. A flow phantom was made with channels of similar diameters to the MCA and insonated with a commercial Doppler system. The resulting sonograms were processed and analysed for evidence of spatial variation in the sensitivity of the ultrasound field.

Method

Flow phantom construction

A wall-less flow phantom was constructed by casting a tissue-mimicking material (Ramnarine et al. 2001) around three cylinders of external diameters 2 mm, 3 mm and 4 mm. The plastic housing of the mould was designed to allow the open face of the TMM to be at an angle to the path of the rods. This can be seen in Figure 6.1. After the TMM had cooled and set, the rods were removed, leaving channels with the appropriate internal diameters. Connectors set into the walls of the mould allowed the channels to be supplied with blood mimicking fluid through external tubing.

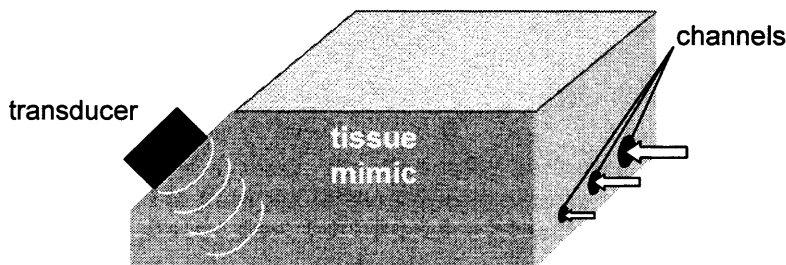


Figure 6.1 Schematic of wall-less phantom. Plastic tubing, via connectors, carries the blood mimicking fluid into the channels in the direction shown by the arrows. The tissue mimic, apart from the face where the transducer is applied, is contained within a rigid plastic structure. The open face is at an angle to the channels.

Blood mimicking fluid

A quantity of blood mimicking fluid (BMF) was made using the recipe of Ramnarine et al. (1998). This fluid contains small (3 μm and 30 μm) nylon spheres that imitate the scattering properties of blood. There is a tendency for these particles to settle out of the mixture with time, so care was taken to stir the fluid thoroughly before use. Aggregation of the particles and introduction of air into the BMF were also problematic. The mixture

was passed through a 40- μm sieve at intervals to remove particulate clumps and the fluid was allowed to run through the system for a time before recording was started to allow bubbles to clear from all parts of the tubing.

Steady flow was accomplished using a gravity-fed, twin reservoir system which is illustrated schematically in Figure 6.2. A peristaltic pump carried the fluid from the lower reservoir to the upper. The flow rate was varied by changing the height of the upper tank and by constricting the outflow tubing from this reservoir. The direction of flow was arranged so that insonation occurred at the distal end of the channels. The channels within the phantom were more than 12 cm long, sufficient for fully developed laminar flow. The entrance lengths were 3.4, 7.9 and 10.0 cm for the 2, 3 and 4 mm diameter channels, respectively.

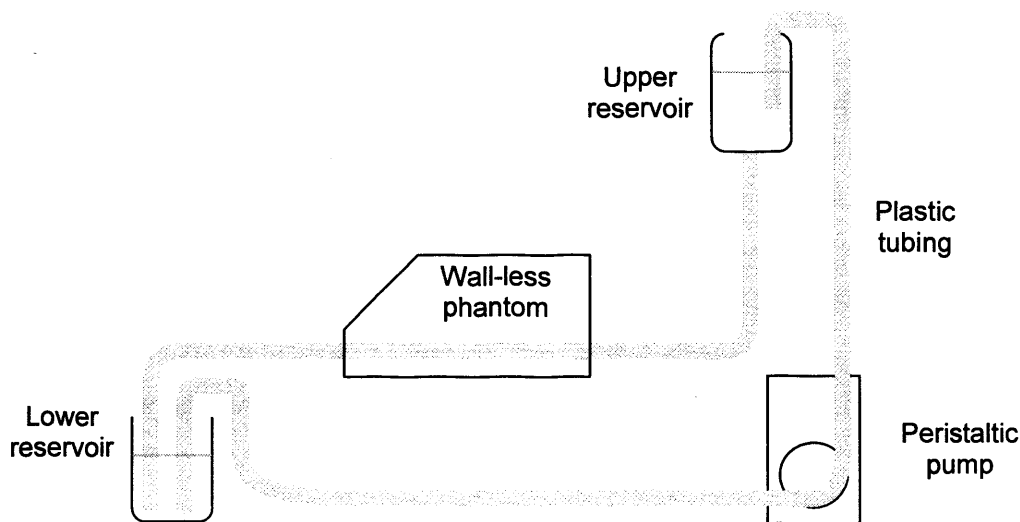


Figure 6.2 Schematic of flow system. Plastic tubing connects the various components and the blood mimicking fluid is pumped to the upper reservoir using a peristaltic pump. Using two reservoirs ensures steady flow, not otherwise possible with a peristaltic type of pump.

Signal acquisition

The phantom was insonated with a commercial, transcranial Doppler system (Scimed PCDop842) using a 2 MHz transducer. A depth of 5 cm and a sample length of 10 mm were chosen, in keeping with both the other studies in this work and the typical clinical settings. The transducer was moved from side to side until the received Doppler signal was at a maximum and then fixed in position with a clamp. In the absence of the overall attenuating effects of temporal bone, it was necessary to reduce the transmitted power of the ultrasound system significantly to avoid saturation of the signal. The audio output, i.e. the Doppler signal, was recorded onto digital audio tape (DAT) for off-line analysis.

Sections of each recording free from artefacts, such as high intensity signals caused by air bubbles circulating in the fluid, were transferred from the tape onto a computer hard disk using a sampling frequency of 12.5 kHz. The files were then read into the MATLAB software package for further analysis.

Signal processing

The audio signal was processed with a 512-point FFT to produce a sonogram – a series of spectral estimates. MATLAB contains a routine (specgram) for this purpose. The input is divided into overlapping segments, which are windowed to reduce spectral leakage. A discrete FFT is then used to estimate the power spectrum of each segment. A 50% overlap of the segments and a Hanning window were used. The length of the segments matched the length of the FFT, i.e. 512 points.

Maximum velocity envelope

For many TCD applications the maximum velocity of the blood is of greatest interest to the practitioner. Usually this is expressed in the form of a time-averaged maximum velocity (TAMV). However, determining the maximum Doppler frequency and, thus, the maximum velocity is not trivial. Several techniques have been proposed, of greater and lesser degrees of sophistication. Often, a simple threshold method is used. This establishes the maximum velocity as the velocity above which the Doppler power density is less than a given threshold. These methods are strongly affected by the noise level of the signal.

The chosen approach in this work was the hybrid method of Mo et al. (1988). This is a refinement of methods that use a threshold to identify the maximum velocity at which a signal exists. The power spectrum for each time interval is integrated to produce a function, $\Phi(v)$. The noise slope, N , is determined from a section of Φ outside the range of the signal. The slope of N , is increased by a factor α , to reduce the possibility of a positive bias in the algorithm. Then the line $\alpha N(v)$ is positioned so that it intersects with Φ at the highest velocity, v_T , in the spectrum, i.e. $\alpha N(v_T) = \Phi(v_T)$. A second point of intersection will now exist at a lower velocity; this is the maximum velocity, V_{MAX} , of the signal.

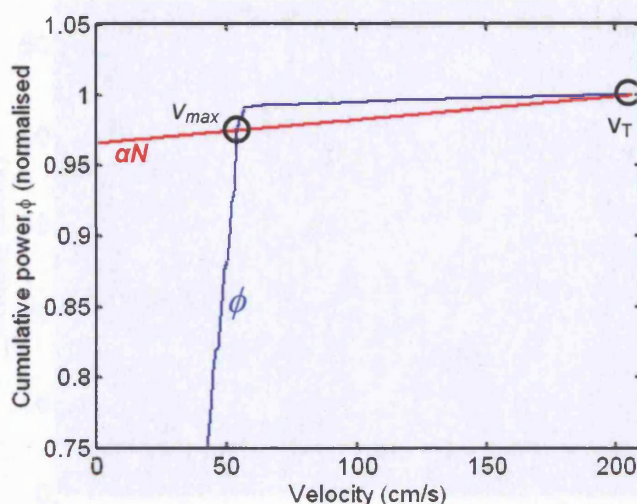


Figure 6.3 Graphical representation of hybrid method for maximum velocity determination. The red line is the noise slope multiplied by a factor α , which reduces overestimation of the maximum velocity. The maximum velocity is then the intersection between the red line, and the blue line which is the cumulative power in the spectrum

Spectral averaging

Individual spectra from the sonogram are very noisy, so the average was taken of neighbouring spectra to produce a better spectral estimate although this reduces the temporal resolution of the sonogram. While the velocity of the fluid is constant, the individual spectra have the same length and the average spectrum is representative of the true Doppler spectrum. For non-steady flow, the situation is not so simple and I will return to this in later chapters.

Results

Sonograms

Recordings from all three channel sizes were successfully collected and sonograms were created to examine and analyse the signals. The sonogram (such as that shown in Figure 6.4) is the traditional method for displaying the TCD signal. It is a two-dimensional representation of the signal strength, with each point, $p(t,v)$, corresponding to the FFT estimated Doppler signal power at time t , for velocity v . Each time slice of the sonogram corresponds to the power spectrum of a 41 ms (512 points at a sampling frequency of 12.5 kHz) segment of the audio signal. The individual spectra have an appearance similar to those shown in Figure 6.5. There is a large variance, arising from the stochastic nature of the Doppler signal, in the weights of the spectral components.

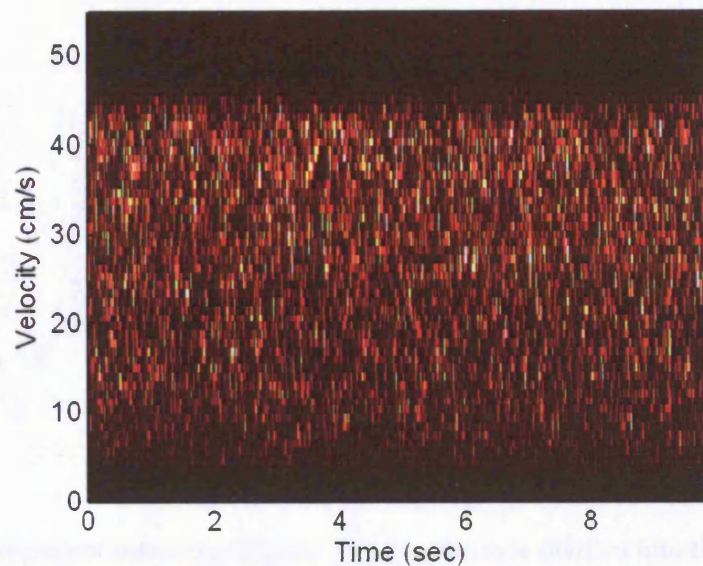


Figure 6.4 Sonogram recorded from steady flow of a blood mimicking fluid through a 4 mm channel in a wall-less phantom.

The steady flow rate of the BMF is apparent from the constant maximum velocity. This should be compared with Figure 7.1 – a sonogram of *in vivo* blood flow.

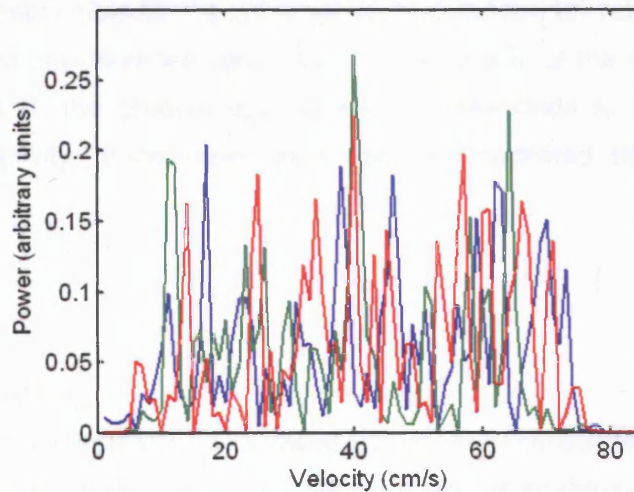


Figure 6.5 Estimated power density for three time segments of the *in vitro* Doppler signal displayed as a sonogram in Figure 6.4

Averaged spectra

Consecutive spectral estimates were averaged to highlight the overall features of the *in vitro* spectrum. Such an averaged spectrum is illustrated in Figure 6.6. Aside from the significant reduction in noise, three main features are apparent in this spectrum:

- no low velocity signals (A),
- a roll-off of power at high velocities (B),
- an overall increase in power from low velocities to high velocities (C).

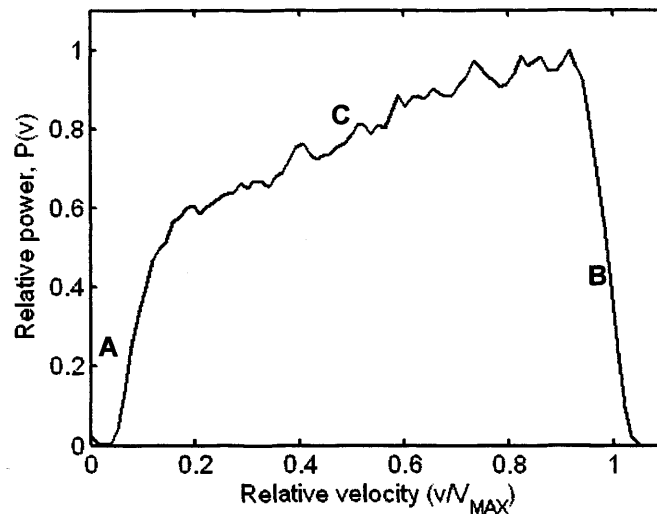


Figure 6.6 Averaged power spectrum. The spectrum is divided into three regions on the basis of the phenomena which contribute to their shape. (A) which is the region of wall-thump filters, (B) shows intrinsic spectral broadening and (C) is most likely influenced by non-uniform insonation

The absence of low velocity signals is due to “wall-thump” filters – high pass filters used to remove the high intensity, low frequency signal from vessel walls. Intrinsic spectral broadening is responsible for the presence of an extended tail rather than a sharp cut-off at a well defined maximum velocity, V_{MAX} . In the middle of the velocity range, between features A and B, the gradual upward slope corresponds to the spatial variation of ultrasound sensitivity. If the vessel were uniformly insonated, this region would be flat, i.e. $dP/dv = 0$.

Discussion

Shape of the spectrum

In a 1990 paper, Thompson et al. showed that *in vitro* spectra can be affected by critical angle effects. Their work was carried out on a type of phantom that directed the blood mimicking fluid through tubing with a density greater than its surroundings. Here, in contrast, a wall-less phantom was used in which tissue mimicking material made up the entire propagation path from transducer to BMF. Thus, although the affected spectra in the paper strongly resemble the spectrum shown above (Figure 6.6), the shapes arise from different phenomena.

ISB and maximum velocity

Intrinsic spectral broadening is at a minimum when the average angle of insonation is 0° . However, even then its presence can be seen as a gradual decrease in power at the

highest velocity bins rather than the sharp cut-off that theory predicts for a single angle of insonation. ISB arises from small variations in the angle of insonation due to finite width of the ultrasound transducer. This variation in the angle of insonation causes a degree of uncertainty in the velocity measurement because of the $\cos \theta$ term in the Doppler equation. Thus, the true maximum velocity will lie somewhere above the velocity where the signal power is highest. A simplistic approach of choosing V_{MAX} as the velocity with the highest power – on the basis that the beam is centred on the vessel – would incorrectly identify the centre of the vessel and underestimate the non-uniformity of the ultrasound beam by ignoring those higher velocity bin whose relative sensitivity has been reduced by the effects of ISB.

Modelling of the effect of ISB (Thompson and Aldis, 2002) has shown that the true maximum velocity can be found at the point where the second differential of the power spectrum, d^2p/dv^2 , is zero, i.e. where the down-slope of the spectrum has reached its maximum steepness. Unfortunately, the individual spectra were too noisy to apply this knowledge to the determination of the maximum velocity envelope. However, the method was applied to an averaged power spectrum with the results shown in Figure 6.7. The noise inherent in a real Doppler spectrum, rather than a modelled one, means that there are many zeros in the second differential of $p(v)$, so it was the last zero crossing that was taken as the estimate of maximum velocity.

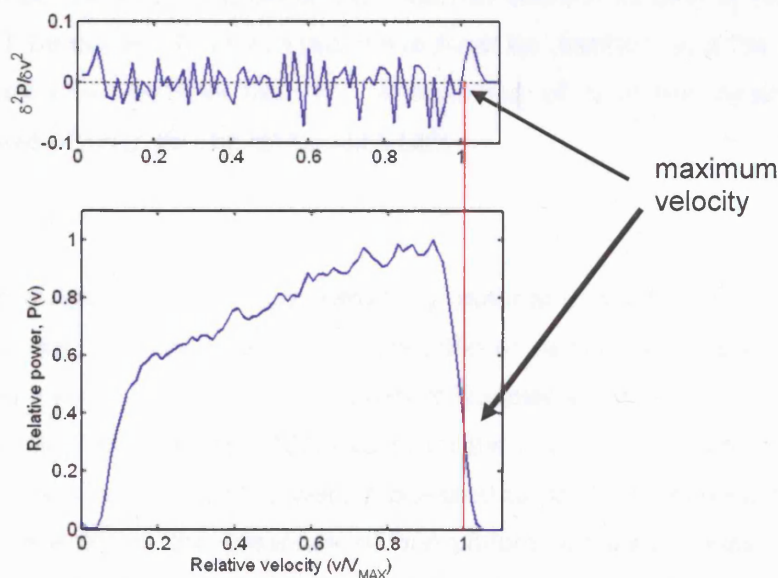


Figure 6.7 Averaged power spectrum, $P(v)$, and second differential, d^2P/dv^2 , demonstrating an alternative method for determining the maximum velocity

The maximum velocity found by this method and the maximum velocity determined by the hybrid algorithm were not the same, even for these *in vitro* recordings where the signal to noise ratio was high. Generally, the hybrid algorithm was found to overestimate the maximum velocity when compared with the differentiation technique. This overestimation could be reduced by increasing the value of α , the multiplier of the noise slope in the hybrid method, but it would be easy to then underestimate the maximum velocity and lose valid data. With an overestimation, it is still possible to use a two-stage process and apply the differentiation method to the remaining data to determine a more accurate maximum velocity for the averaged spectrum. An initial underestimate of the maximum velocity would incorrectly classify true signal as noise and result in the rejection of this data without the hope of subsequent recovery. It is also possible that the differential method was an overestimate and the hybrid method was more accurate. More work could be done with flow phantoms to investigate this possibility.

Spectral averaging

Spectral averaging can reduce the variance of Doppler spectrum estimates by a factor N , where N is the number of independent estimates used in the average. If the estimates are not independent the reduction in the variance will not be as large. Segments will be independent if they are sufficiently widely separated in time. Increasing the length of segments is possible but would prove problematic for pulsatile, *in vivo* flow as data become non-stationary with resulting spectral broadening. If segments are too short, spectral resolution will be reduced because of the condition that the lengths of the data segments and the FFT be equal. Thus a compromise must be reached, and the actual reduction in the variance will be less than N . A reduction of N in the variance is equivalent to an increase of \sqrt{N} in the signal-to-noise ratio.

Conclusions

A wall-less phantom constructed from tissue-mimicking material and a blood-mimicking fluid were successfully used to produce an *in vitro* imitation of steady blood flow. When insonated with a commercial TCD machine the resultant Doppler signal was very similar in appearance to *in vivo* signals from the MCA except for the non-pulsatile nature of the flow in the phantom. The signals collected were processed to produce sonograms and power spectra. After averaging, the presence of non-uniform insonation was clearly visible in the shape of the spectral estimates of the *in vitro* Doppler signal. Having established this, the next step in the process was to look for similar features *in vivo*. Then the possibility of using the Doppler signal to determine the shape of the insonating beam could be considered.

Chapter 7 – In vivo recordings

Introduction

Having found non-uniformity effects in the Doppler signal *in vitro*, samples of *in vivo* recordings were obtained to look for similar effects. *In vivo* recordings provide a number of challenges unmatched *in vitro*:

- the ultrasound beam shape is completely unknown;
- the true angle of insonation cannot be measured or calculated;
- the flow is pulsatile;
- there is a poorer signal to noise ratio, at least in part due to the attenuation of the signal by the temporal bone.

The temporal variation in maximum velocity due to pulsatile flow prevents use of the previous method of improving the signal to noise ratio by averaging over consecutive power spectra. Two approaches were taken to accommodate this. The first was to isolate spectra with similar maximum velocities, such as at systole, and average just these spectra from each cycle. The second was to modify the original sonogram to produce a flat maximum velocity envelope. The latter method allowed all spectra from a recording to be included in the average.

Method

Signal acquisition

Doppler recordings were collected from seven healthy volunteers. Short duration recordings (< 30 seconds) were acquired with the subject seated and the TCD operator holding the transducer in place. Longer recordings were collected with the subject either lying or sitting comfortably using an elastic headband to fix the transducer. The signals were recorded onto DAT as with the *in vitro* recordings.

Systolic identification

The recorded signals were checked for artefacts, and uncorrupted sections of the recordings were digitised and stored on a PC as previously described in Chapter 6. Firstly, sonograms were produced from the audio signal. These sonograms were then processed using the hybrid algorithm discussed in the previous chapter, to identify the maximum velocity envelope. Unlike the *in vitro* recordings, the maximum velocity varies throughout the cardiac cycle; it was used to identify the segments of each cycle. Three neighbouring spectra were isolated from each systole. These frames were averaged, producing a single, systolic, power spectrum for that recording.

The algorithm used to identify the systolic part of the cycle searched the gradient of the velocity envelope for the steep upslope that occurs between the end of one cycle and the start of the next. It was felt that this was a distinctive feature that would clearly identify the division between cycles, whereas the use of the systolic velocity itself could be adversely affected by the reduced SNR of the longer spectra. A variable threshold setting for the steepness of the slope added to the algorithm accounted for the variation in pulsatility of the flow in the different recordings. Signals with low pulsatility had the threshold reduced to avoid missing beats and signals with high pulsatility had the threshold increased to avoid detection of extra peaks. The threshold value was changed up or down automatically by a subroutine that looked for "extra" or "missed" beats. These showed up as irregularly spaced points, occurring too near or too far from their neighbours, when compared to the average spacing in the rest of the recording.

Flattening the sonogram

Although it was reasonably simple to isolate the systolic segments from the recordings, by choosing just these frames the average is limited to only a few spectral estimates from each cycle. A 20 second recording may produce an average power spectrum that is composed of fewer than 60 individual spectra – an improvement in SNR over an individual spectrum of $< \sqrt{60}$. (The discussion of averaging and independent estimates from Chapter 6 also applies to this case.) Averaging all of the 900 spectra in such a sonogram instead would give an SNR improvement approximately four times better than selective averaging of systolic frames. The *in vivo* signals had a lower, inherent SNR than the *in vitro* signals. With both of these factors in mind, a new algorithm was developed to allow all of the spectra in the sonogram to be averaged together. This new algorithm was needed because *in vivo* spectra are of varying lengths and applying the previous method would distort the shape of the eventual average.

The new technique was based on three assumptions: that the shape of the ultrasound beam does not change; it is in a fixed position relative to the vessel (and the vessel does not change size) and the velocity profile is constant, i.e. the relative velocities of scatterers at different radii do not vary with time (although the absolute velocities change).

The maximum velocity envelope was used to divide the sonogram into two parts:

- useful signal data – points up to the maximum velocity and

- noise - points above the envelope, which were discarded.

Once divided in this way, the data consisted of a large number of spectra of varying lengths. These were inspected to determine the number of components in the longest spectrum, i.e. the spectrum for which the maximum velocity was highest. The rest of the spectra were re-sampled to this maximum length, creating a set of spectra of equal length. An overall weighting factor was applied to the velocity components in each spectrum, so that the total power in any spectrum, $P(t) = \sum_v p(v, t)$, remained the same as before re-sampling. As all spectra now had the same length, the sonogram was, in effect, flattened; giving it the appearance of steady, non-pulsatile flow. From this flattened sonogram, an average spectrum, $\overline{p(v)}$, was produced by averaging the individual estimates of $p(v_i)$.

The success of the sonogram flattening technique obviously depends heavily on the accuracy of the maximum velocity envelope determination. In the first place, an appropriate multiplier for the noise slope must be chosen. It is also important that the technique work consistently in both the high and low velocity portions of the cycle, otherwise the shape of the spectrum at high velocities will be distorted.

Long-term repeatability

In clinical practice, *in vivo* recordings are frequently of more than 30 seconds duration. Therefore, data suitable for a study of the stability of the technique was collected. Four recordings of the Doppler signal from right MCA of the same subject were made. The recordings occurred at 15-minute intervals with the subject resting in between. An elasticated headband was used to minimise positional variation of the transducer.

Results

Figure 7.1 shows an example of a section of an *in vivo* recording with the maximum velocity envelope outlined in blue and the divisions between cycles identified by green crosses. The systolic frames were taken from the section of the sonogram between three and five frames after the start of each cycle, as indicated by the crosses. The position of the maximum velocity relative to the division between cycles will depend on the heart rate of the subject – there will be more frames per beat for slower heart rates – and the steepness of the upslope. The number of cycles that can be averaged from each cycle will also depend on the subject's heart rate. If the heart rate is fast, there

may be too large a difference in the maximum velocity of neighbouring spectra. The average systolic spectrum (taking three frames from each cycle) for the 10 seconds of data displayed in the sonogram in Figure 7.1 is shown in Figure 7.2.

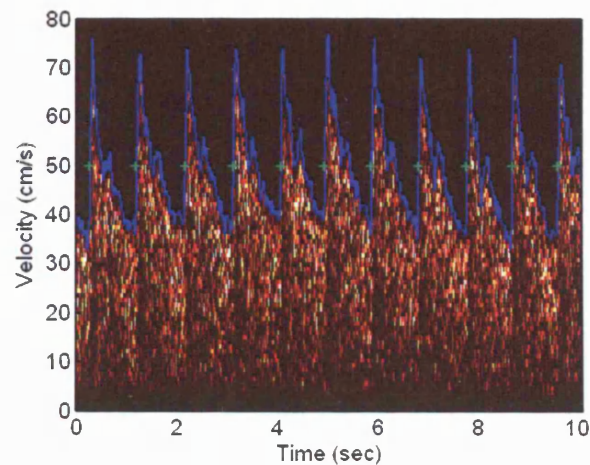


Figure 7.1 Ten seconds of *in vivo* sonogram data from a healthy subject. The maximum velocity envelope is marked in blue and divisions between cardiac cycles are marked with green +

The major features seen in the *in vitro* recordings are again visible: there is evidence of high pass filtering (A), non-uniform insonation (C) and, possibly, intrinsic spectral broadening (B). These features are less clear and the spectrum itself is noisier than Figure 6.5, but approximately three times fewer spectra have gone into producing the average in Figure 7.2. Furthermore, as already mentioned, the *in vivo* signal had an inherently poorer SNR.

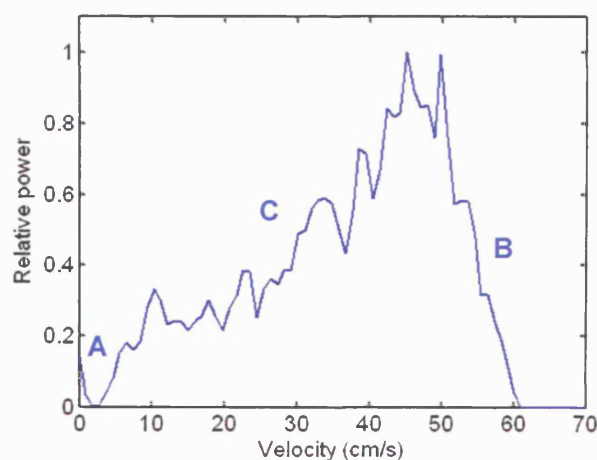


Figure 7.2 An average of the systolic spectra in the ten second recording shown in Figure 7.1. The labelled regions match those in Figure 6.6 – A: wall-thump filters, B: intrinsic spectral broadening, C: non-uniform insonation

Figure 7.3 shows a 'flattened' sonogram again produced from the original sonogram in Figure 7.1. The velocity scale has been converted to relative velocity. The 'flattened' sonogram could be averaged over all spectra.

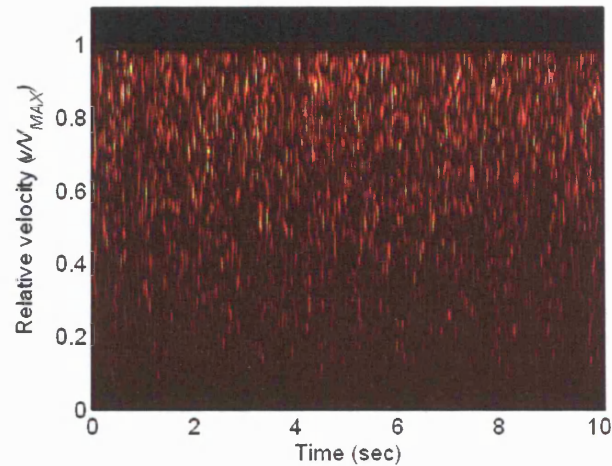


Figure 7.3 A 'flattened' sonogram obtained by interpolating all spectra from the sonogram in Figure 7.1 to the same length

Figure 7.4 shows the averaged spectrum from the full ten seconds of *in vivo* data. There is significantly less variance in the relative weights of the velocity components. The difference in power with velocity is also striking: indicating that there is significant non-uniform insonation of the vessel. A visual extrapolation of the slope through the low frequency region suggests that the sensitivity at the edges of the vessel is less than 20% of the sensitivity at the centre.

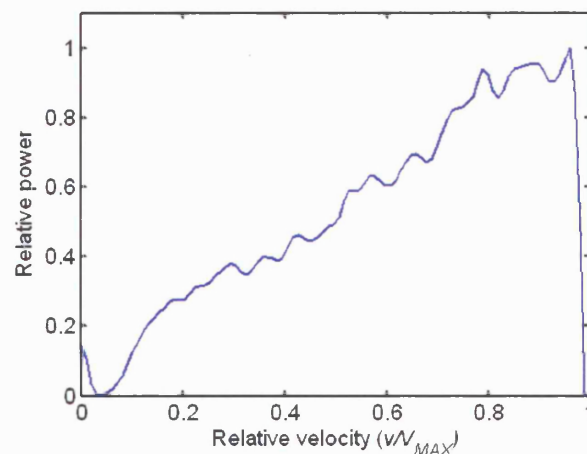
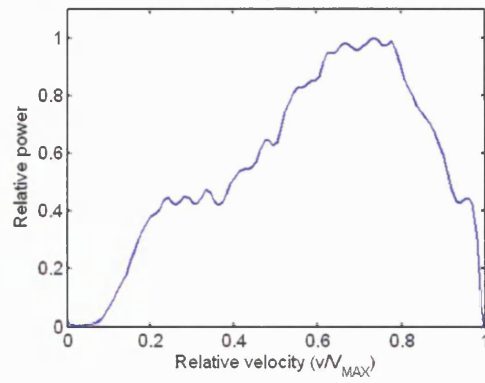
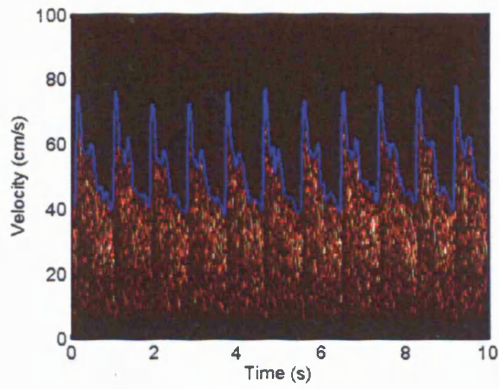


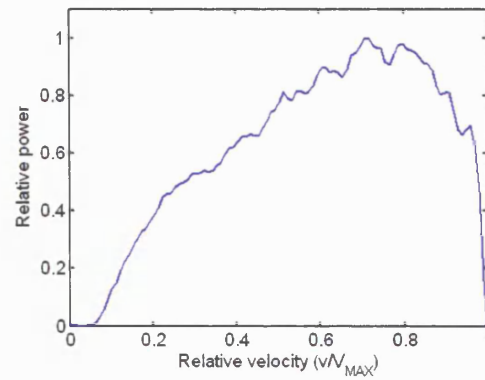
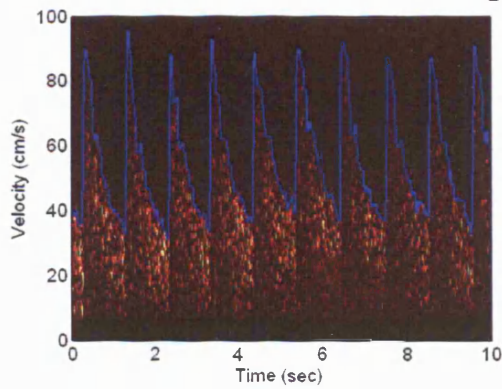
Figure 7.4 The averaged power spectrum from the flattened sonogram in Figure 7.3

A series of sonograms and averaged power spectra from seven healthy subjects are shown in Figure 7.5. The previously described processes of identifying the maximum

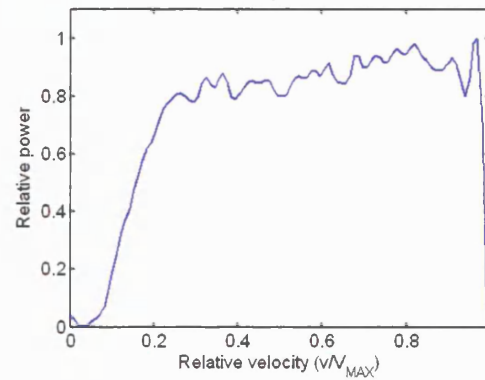
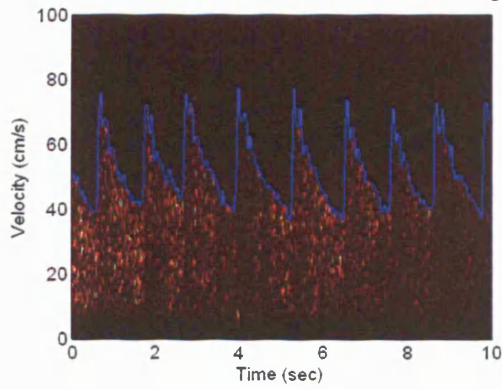
Subject 1



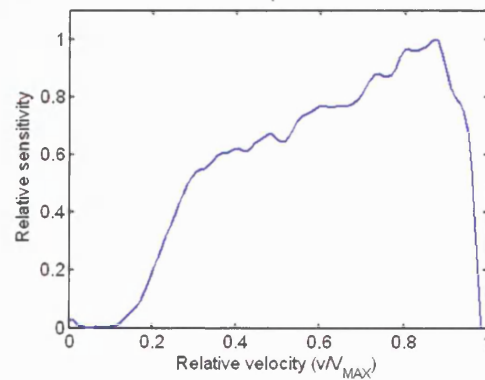
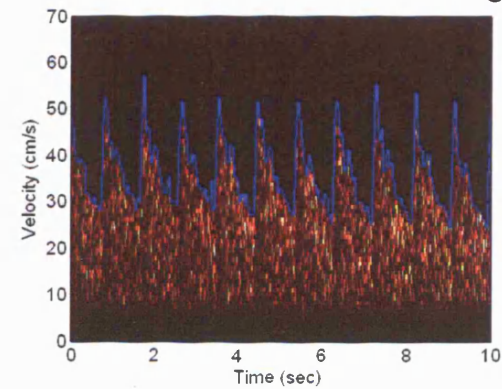
Subject 2



Subject 3



Subject 4



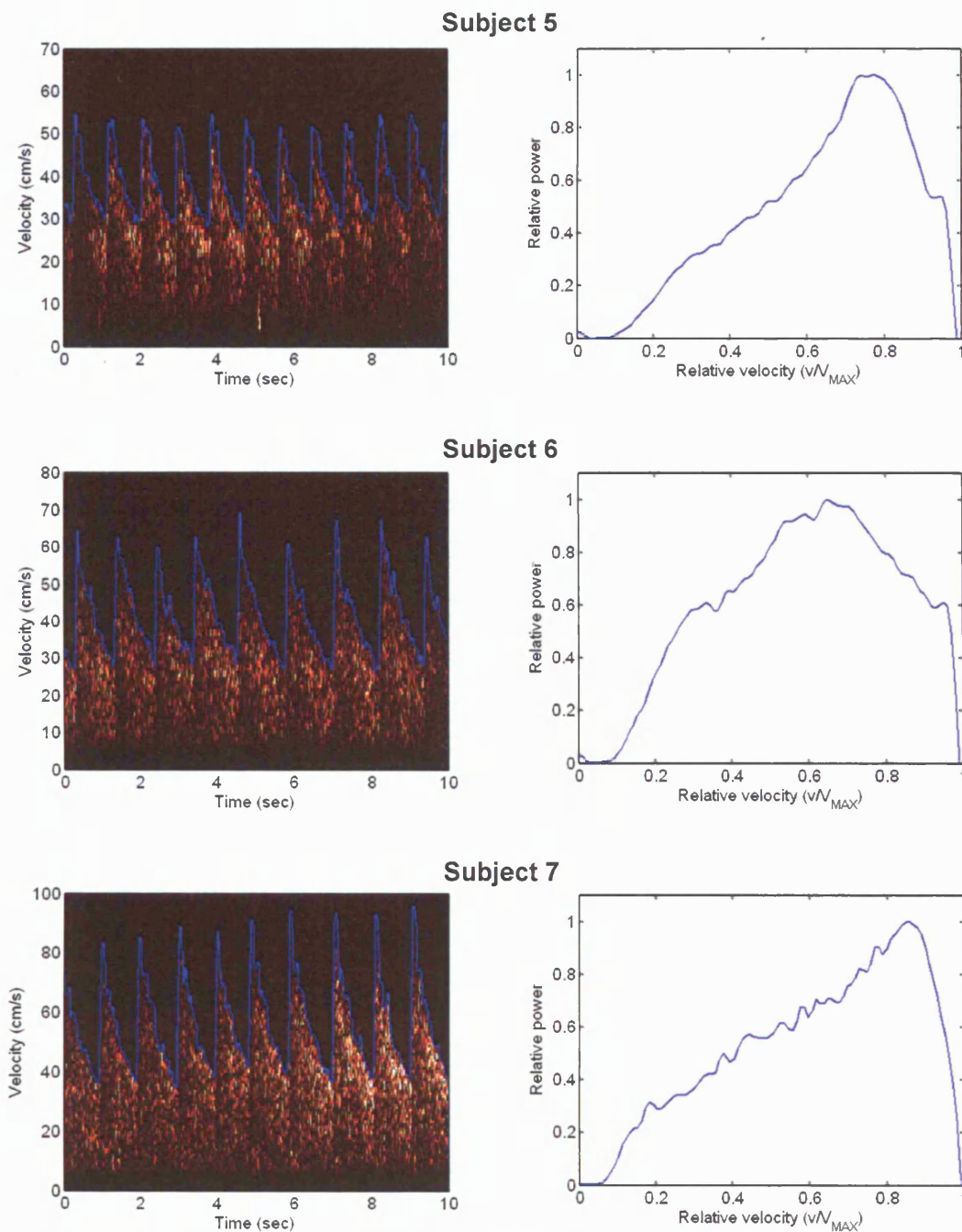


Figure 7.5 10-second segments of data from healthy subjects displayed as sonograms, including maximum velocity envelope (left-hand column), and averaged power spectra (right-hand column)

velocity envelope and flattening the sonogram were followed in creating each of the averaged power spectra.

Ten second sections were isolated from the repeated recordings. Although the transducer was fixed with a headband, it was found that small adjustments were

necessary to re-maximise the signal before each recording. The total signal power for these recordings was not constant, but the variation was less than 1 dB from the mean power of the four recordings. The signal power, relative to the mean, for each of the four recordings is shown in Figure 7.6.

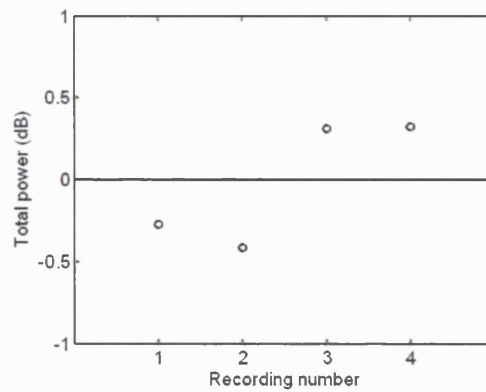


Figure 7.6 Relative power of four *in vivo* recordings taken from the same subject at approximately 15-minute intervals

The flattening and averaging algorithms were applied to these sections of recordings. Figure 7.7(a) shows all four averaged spectra. They are very alike in appearance. However, systemic offsets in power would be obscured by the individual normalisation of each spectrum. For comparison, Figure 7.7(b) shows the averaged power spectra for four, contiguous, 10-second segments of a single recording. The variation between spectra does not appear to be much larger for recordings that have a greater separation in time.

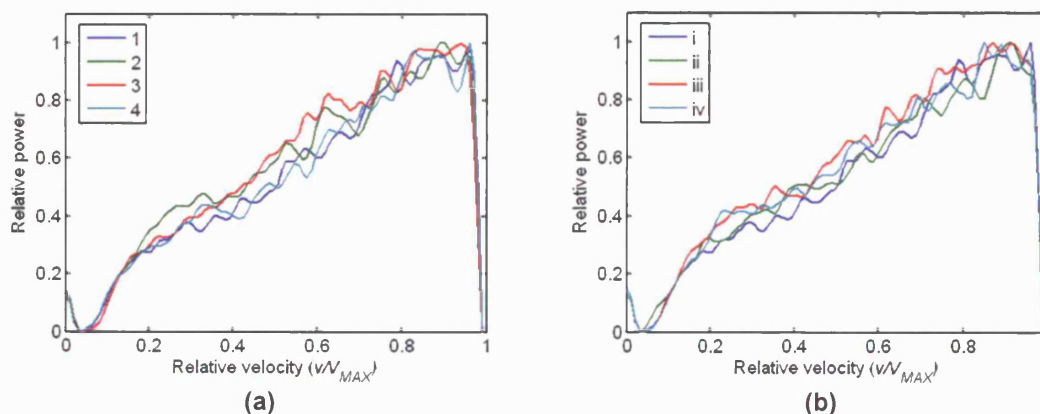


Figure 7.7 Averaged power spectra from four, 10-second, *in vivo* recordings of the signal from one subject with 15-minutes intervals between the data segments (a) and contiguous segments of data (b)

Discussion

The systolic and average spectra (presented in Figure 7.2 and Figure 7.4, respectively) appear to be quite different in shape. Part of this difference is due to a scaling of the horizontal axis, which makes the slope of the first look much steeper than that of the second. In Figure 7.8 below, the two spectra are shown again (in red and blue) on using relative rather than absolute velocities. Alongside them (in green) is plotted a spectrum taken only from diastolic segments of the sonogram. There is a visible difference between all three spectra, notably the increased smoothness of the spectrum corresponding to an average of all the individual spectral estimates. The systolic and diastolic averages are made up of approximately fifteen times fewer estimates. The spectra are scaled for their average power density rather than the normal approach of normalising to the maximum power.

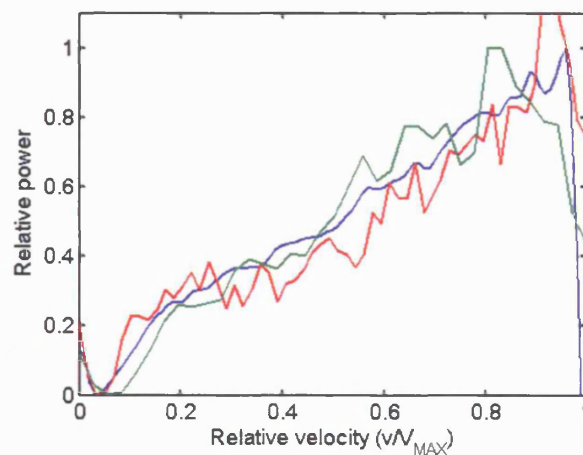


Figure 7.8 Power spectra at systole (red), diastole (green) and an average for the complete cardiac cycle. Spectra taken from the recording presented in Figure 7.1

Both of the assumptions that were used to develop the flattening technique have their difficulties. The issue of beam shape constancy *in vivo* has already been raised in Chapter 2 and there is little more that can be added to that discussion here.

The assumption of an unchanging flow profile may also seem weak. It has been demonstrated that the pattern of flow in the common carotid artery changes with the phase of the cardiac cycle. A comprehensive examination of the flow profile in the MCA is not possible using TCD. However, Evans (1982) showed it is possible, via the Womersley equations, to develop a mathematical description of the flow profile in a vessel for a given set of parameters including flow velocity and vessel size. Using the

equations included in that paper, together with an average waveform from an *in vivo* recording, the velocity profile for a 3 mm MCA was calculated. The model profile was found to be nearly parabolic throughout the cardiac cycle, as shown in Figure 7.9, never deviating from a parabolic shape by more than 0.2%. Thus, the parabolic profile assumption is an acceptable one.

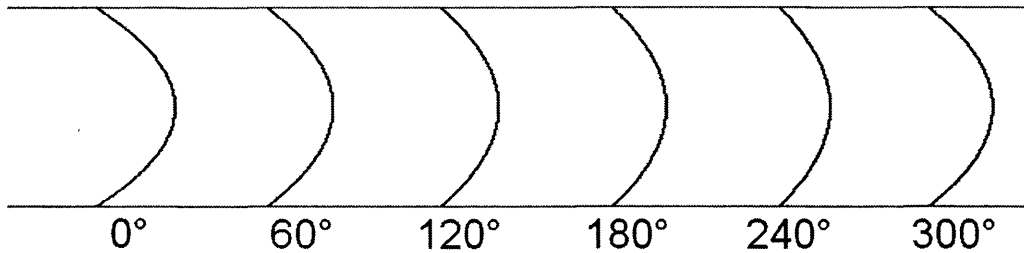


Figure 7.9 Velocity profiles in the MCA at different times in the cardiac cycle. These were calculated from physiological data and Womersley flow equations

As an alternative, the ratio V_{IWM}/V_{MAX} can be used to look for periodic changes in the shape of $v(r)$ *in vivo*. A plot of V_{IWM}/V_{MAX} (see Figure 7.10) for the recording presented as a sonogram in Figure 7.1 does not show any evidence of periodicity related to the heart rate. However, neither of these approaches constitute conclusive evidence that the flow profile is unchanging and, thus, that the flattening technique does not distort the spectral estimates.

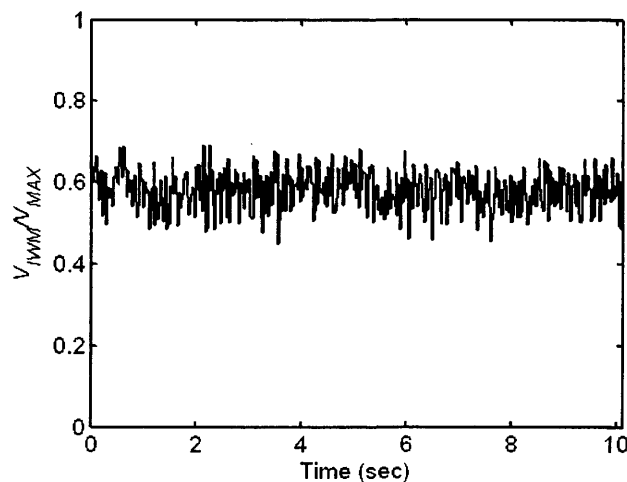


Figure 7.10 Ratio of intensity-weighted mean velocity to maximum velocity, V_{IWM}/V_{MAX} , for a 10 second *in vivo* recording. Changes in the velocity profile would change the ratio of V_{IWM}/V_{MAX}

It might be expected that, even for an unchanging velocity profile, there would be some cyclical variation in the ratio because of the fixed cut-off of the high pass filters but this

is not seen in Figure 7.10 either. It may be that both effects are too small to be seen in the ratio, or it may be that the two effects counteract each other.

Accuracy of maximum velocity envelope

The correct identification of the maximum velocity was, as ever, challenging but no more so than in any other situation. As always, the greater the signal-to-noise ratio, the easier it is to determine an accurate maximum velocity. The concern arising from the use of the sonogram flattening method is that the averaging technique would be invalidated by a poor maximum velocity determination. By varying the coefficient α in the hybrid algorithm, it was possible to produce envelopes that over-estimated and under-estimated the maximum velocity. The sonogram flattening technique was applied to these spectra and the flattened sonograms were averaged as before. The signal-to-noise of the Doppler signal used in Figure 7.11 was 14 dB.

It was discovered, on examining the averaged spectra, that the appearance of the spectrum seemed to indicate how well the maximum frequency follower performed. Examples of over- and under- estimation of the maximum velocity envelopes are shown on the left in Figure 7.11. On the right of the figure are the averaged spectra from the flattened sonograms. Overestimating the maximum frequency produced a spectrum with the highest power in the centre and a shallow downward slope at higher velocities (Figure 7.11 a). An underestimated maximum frequency introduced a noticeable peak at high velocities (Figure 7.11 b).

However, care should be taken not to ascribe to the maximum envelope method features that arise from the positioning of the transducer. Returning to Figure 7.5, the appearance of the averaged power spectrum for Subject 1 might indicate that the chosen value of α was too low and the maximum velocity was overestimated. Closer examination of the data established that this was not the case. In Figure 7.10, a single spectral estimate and the cumulative sum of this estimate are presented. The position of the maximum velocity as determined by the hybrid algorithm is also indicated. A visual inspection of both plots confirms that the maximum velocity is appropriately identified and that the maximum power in the spectrum is found at velocities below this maximum.

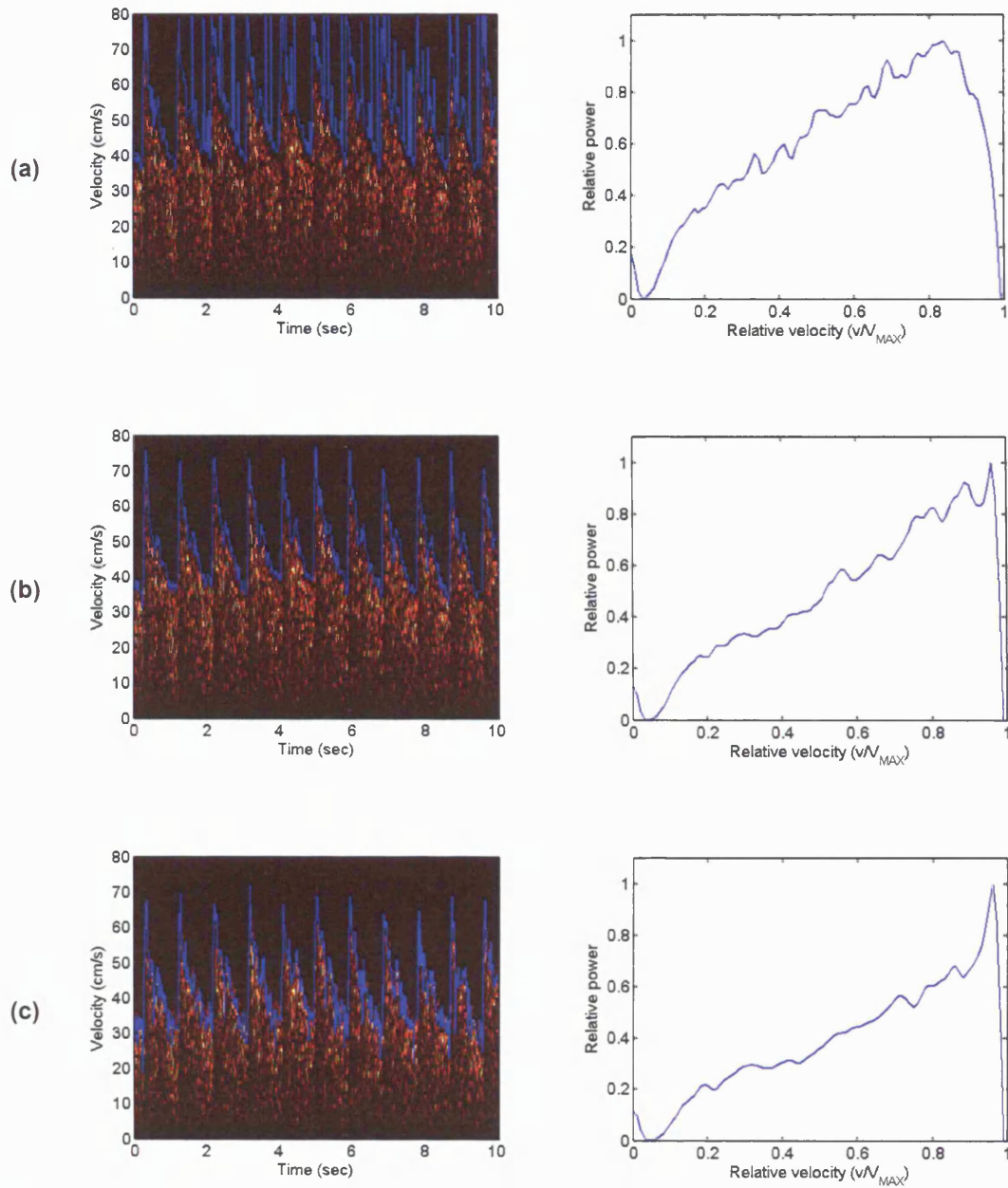


Figure 7.11 Sonograms with maximum velocity envelope marked in blue and the resulting averaged power spectra from the flattened sonograms. The top row (a) shows an overestimation of the maximum velocity and the bottom row (c) an underestimation. The centre row (b) shows what is considered to be an appropriate maximum velocity envelope.

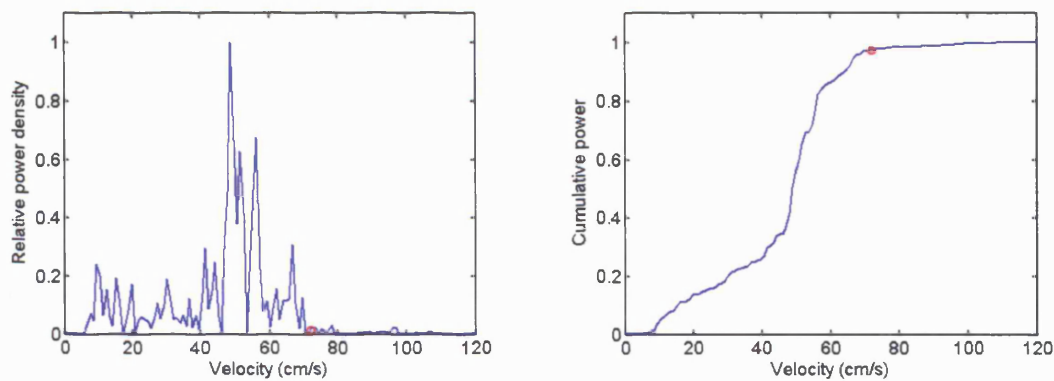


Figure 7.12 An individual spectral estimate for one time interval of the *in vivo* signal from Subject 1 and the corresponding cumulative power distribution with the maximum velocity (as determined by the hybrid algorithm) indicated in red

It could be that the beam and vessel were offset in this case, with the axis of maximum sensitivity at a distance from the centre of the vessel. Alternatively, there may be a situation when two vessels are within the sample volume, or the MCA is particularly curved. In which case, the sonogram may be comprised of a superposition of two signals with different maximum velocities and different powers.

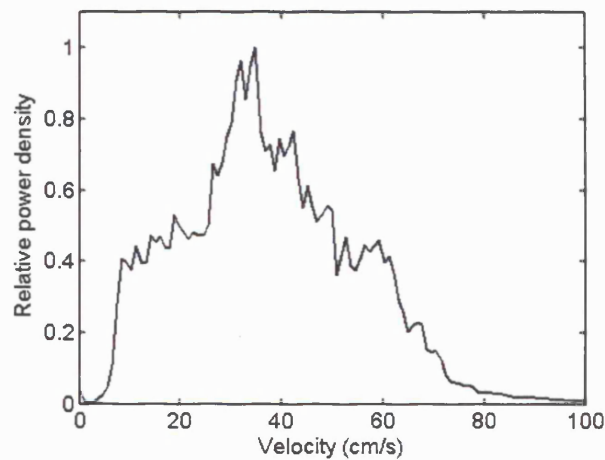


Figure 7.13 Selectively averaged spectra from an *in vivo* signal showing a peak in power for the middle of the velocity range

Flattening the sonogram is a solution to only one of the differences between temporal averaging of the *in vivo* and *in vitro* signals. Spectral broadening in the individual estimates because of the acceleration of the blood must be considered also. However, the velocities in the MCA are generally not high, $V_{SYS} < 100$ cm/s, and the pulsatility is also quite low, maximum slope of 0.03 kHz/ms. For this reason the 41 ms segments used to process the *in vitro* signal were considered appropriate. This is backed up by the calculations in Fish (1991) which show that the non-stationarity broadening when

using a 40 ms Hanning window with the type of signals under investigation here is on average less than twice the minimum, which occurs for windows of 10-15 ms duration. Keeping a longer FFT length also maintains the reliability of the maximum velocity algorithm.

One failing of the method is an issue that arises from the algorithm used by MATLAB to resample the (individual) spectra. This algorithm assumes that the value of the points outside the resampling region is zero. While this is appropriate at the low velocity limit where the power density tends toward lower values – zero when the filtering is sufficiently powerful – it causes unsuitable interpolations at high velocities. It is visible in the averaged spectrum as a rapid reduction in power as v approaches V_{MAX} . An alternative algorithm which assigns a value of 1 to points above the resampling region (i.e. for velocities in excess of V_{MAX} – velocities above the maximum are, of course, not possible) may improve the appearance of the resampled spectrum, but could introduce artefacts that would be less easily distinguished from real features than the artefacts arising from the use of 0. It was felt that it was more appropriate to retain the original algorithm and exclude those points affected by the artefact from further processing and analysis.

Conclusions

Using TCD recordings from volunteers, it has been shown that it is possible to find evidence of non-uniform insonation of the MCA *in vivo*. This was demonstrated both for short duration recordings from several subjects as well as repeated measurements over time from the same subject. Two averaging techniques were considered in the processing of the signals, using two different approaches to dealing with the time varying nature of the *in vivo* signal. The second method, which used the maximum velocity envelope to flatten the sonogram, allowed all the spectral estimates to be combined into a single, average power spectrum for each recording.

Chapter 8 – Reconstructing Beam Shapes

Introduction

The averaged power spectra that were obtained from the *in vitro* and *in vivo* recordings demonstrated that the effects of the non-uniformity in the ultrasound beam could be seen in the Doppler signal. Extracting more detailed information on the beam's shape required further processing of the data in order to progress from the measured variation in power to a variation in sensitivity across the vessel.

If a method of estimating the beam shape were to be obtained, it could be used to look for changes in the vessel under investigation (MCA or flow phantom channel). In the absence of other factors, such as transducer movement, apparent changes in the beam shape must be attributable to vessel diameter changes. *In vivo*, transducer movement is hard to avoid unless a fixation device is used and the signals are taken from the same examination. For *in vitro* recordings, in which a more predictable, less variable beam shape exists, it might be possible to compare reconstructed beam shapes from recordings at different times and of different channels.

Method

Converting to radial sensitivity

The first step in creating the sensitivity profile of the insonating beam was a plot of relative power for increasing distance from the vessel centre. Once again there were certain assumptions that had to be made. The most critical of these was that the flow in the vessel had a parabolic profile. Making this assumption allowed the averaged power spectrum, which gives the information on power as a function of velocity, to be converted to the power as a function of radius, $P(r)$.

Inverting the parabolic flow equation gives

$$r/R = \sqrt{1 - v/V_{MAX}} \quad \text{Equation 8.1}$$

Using equation 8.1, the x-values were converted from relative velocity to relative distance. The new coordinates were no longer equally spaced. However, the areas of the annuli remained the same (and equal to each other). And, as the intervals still corresponded to equal areas, the power in each must remain proportional to the sensitivity of the ultrasound, so $p(r)$ is the same as the relative, radial sensitivity.

However, further action must be taken to account for the modification of the spectrum by filtering, ISB and attenuation.

Selecting valid data

As shown in previous chapters, it is not only beam inhomogeneities that affect the *in vivo* and *in vitro* signals. Spectra are strongly influenced in certain areas by filtering and spectral broadening. Data that will be used for the reconstruction of the beam shape must exclude these areas. The approach to removing data from the ISB-affected region was reasonably simple. Any values of p from within the radius, i.e. above the velocity, at which the maximum power occurred were excluded. Deciding which points to exclude because of wall-thump filtering was less straightforward, but it was also less critical than the removal of the ISB-affected data as it related to a smaller portion of the eventual sensitivity profile. In practice, a visual inspection of $p(r)$ and a determination based on the perceived gradient were considered sufficient. Unfortunately, removing these sections of data often restricted the valid dataset to points covering just over half of the radial distance and introduced the further problem of how to reconstruct those parts of the beam for which valid data were unavailable.

Fitting data to model

The decision was made to use a model of a typical beam shape to fit the available sensitivity data. The model had two degrees of freedom, corresponding to the width and height of the shape. It also extended to very low values of sensitivity, which allowed it to cope with large vessels. The primitive shape itself was derived from the measurements of beams in water that were presented in Chapter 2. This is a numerically, rather than analytically, described shape and is shown in Figure 8.1.

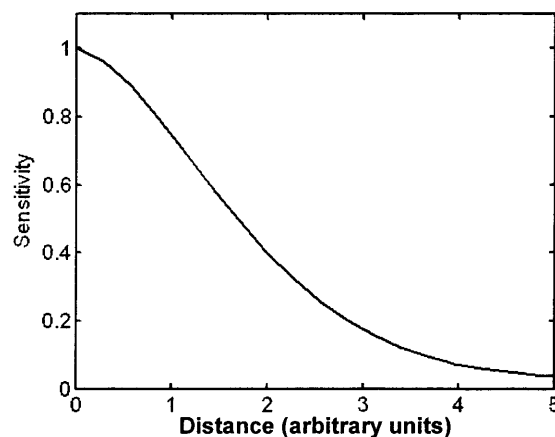


Figure 8.1 Typical beam profile, taken from free field measurements. This forms the shape to which the beam shape reconstructions are fitted.

The least squared error was used to find the closest match of the model to the sensitivity data collected from the spectrum. The width of the shape was changed to match the slopes of the model and the data, while height adjustments were used to find an appropriate relation between the two at $r = 0$. The modelled beam covered the full range of radial distances, unlike the data it was being fitted to, meaning the relative sensitivities at $r = 0$ and $r = R$ could also be estimated.

Distinguishing different channel sizes *in vitro*

Three recordings, from the three different sized channels in the phantom, were digitised and an averaged power spectrum was created from a 10-second segment of each recording. The usual methods were used to estimate the true maximum velocity in the channel and the procedures for processing the data described in the previous paragraphs were followed, i.e. the production of radial sensitivity profiles and the fitting of them to the beam shape model. The three beam shape reconstructions were then scaled from relative radial distances to absolute values, using the known channel sizes of 2, 3 and 4 mm. Once the scaling was complete, the three shapes were compared with each other. A further comparison was made between the absolute size of the reconstructed beams and the free field measurement of the beam. This comparison, only possible *in vitro*, gave an indication of the systematic error of the reconstruction technique.

Comparison of relative vessel sizes *in vivo*

Although measurements of their absolute size were not available for either the beam widths or vessel diameters *in vivo*, the reconstructed beam shape allowed a comparison of the relative sizes. From the location of the 50% sensitivity point, using extrapolation when necessary, the size of the vessel could be estimated in units of $r_{50\%}$ - the beam width for that particular recording. Figure 8.2 shows one such *in vivo* reconstruction where the ultrasound sensitivity has dropped to 50% at a distance $0.655R$ from the centre of the vessel, where R is the vessel radius.

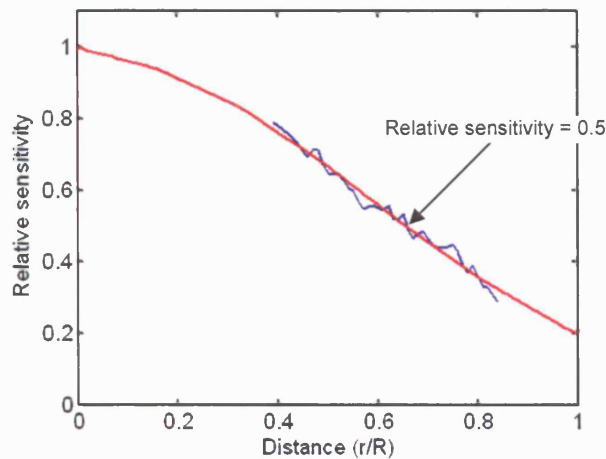


Figure 8.2 Reconstructed beam profile in red, with raw data in blue, showing the distance at which the sensitivity is 50% of the maximum. This distance can be used to compare the relative sizes of the beam and vessel.

Repeatability

The repeatability of the averaged spectra and the beam shape reconstructions was tested by taking consecutive sections of the sonogram over a 20-30 second period, with each of the sections having one-second duration, and producing separate beam shape reconstructions for all of them. A mean shape for the reconstruction was then found by taking the average of the sensitivity estimates at each radial distance. A similar approach was used to calculate the standard deviation (s.d.) in the sensitivity estimates. The boundaries set by plotting the mean \pm s.d. sensitivity profiles were then used to quantify the variability in the estimate of the vessel width. A line, parallel to the x-axis, was drawn to intersect with the mean beam shape at $r/R = 1$. The additional intersections of this line and the two boundary profiles indicated the range of vessel widths within one standard deviation of the mean.

Results

In vitro recordings

Figure 8.3 shows a power spectrum (a) from an *in vitro* recording and its corresponding radial power plot (b). The highlighted areas indicate portions of the data that have been affected by extrinsic factors: ISB (in pink) and wall-thump filters (in green). The relative sizes of the regions in the two plots show how an apparently small amount of spectral broadening can affect a much larger portion of the radial power distribution. The highlighted areas are also those from which data will be excluded from the reconstruction procedure.

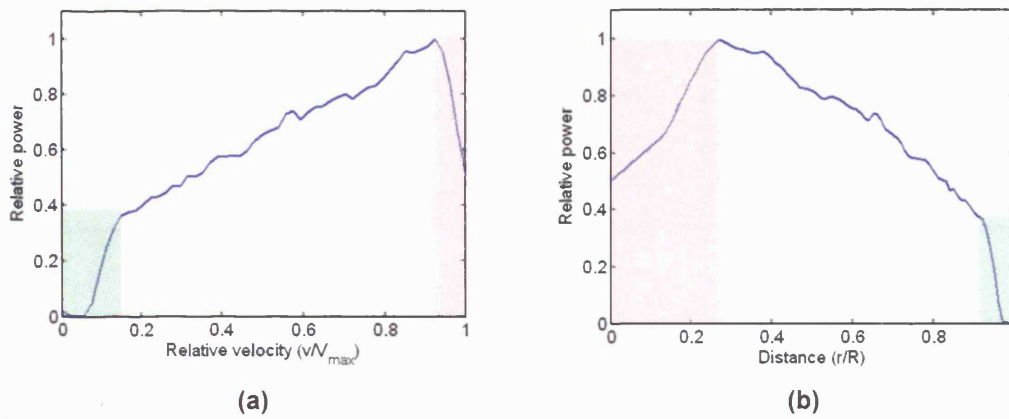


Figure 8.3 Average power spectrum on the left and converted to a plot of power as a function of distance from the centre of the vessel. The pink shaded areas correspond to areas affected by intrinsic spectral broadening. The green shaded areas correspond to regions affected by wall-thump filters.

Figure 8.4 shows a segment of data fitted to the model beam shape. The excluded data are shown as a dashed line. There is a good fit between the data and the model beam shape although it appears that the model shape may not be the best design.

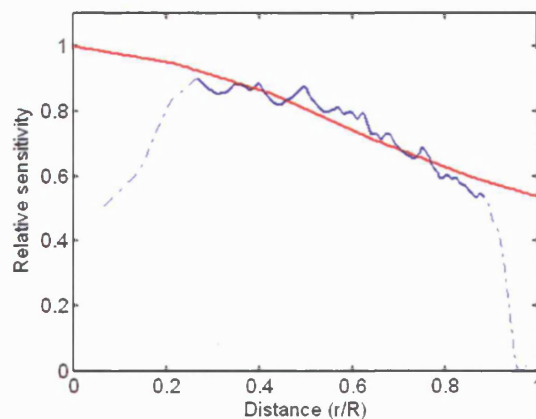


Figure 8.4 Beam shape model (solid red line) fitted to raw data (solid blue line). The dashed line shows sections of raw data that were excluded because of spectral broadening and wall-thump filters.

Variation in channel sizes

When the model was applied to a number of recordings from the flow phantom, it was found that there was a clear difference in the beam shapes that were reconstructed from the different channel sizes. This can be seen in Figure 8.5.

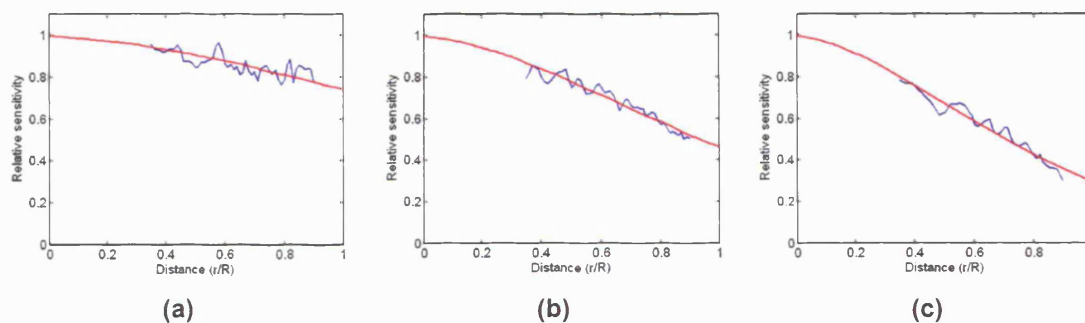


Figure 8.5 Raw data (blue) and reconstructions of beam shapes (red) for averaged power spectra of the signals from (a) 2 mm, (b) 3 mm and (c) 4 mm diameter channels of the *in vitro* flow phantom

Figure 8.6 combines all three reconstructions, scaled appropriately to the width of the channel from which they were taken, and the free field beam sensitivity. The reconstructions are generally similar to each other in appearance – the 3 mm and 4 mm channels coincide – and are also close to the free field beam shape.

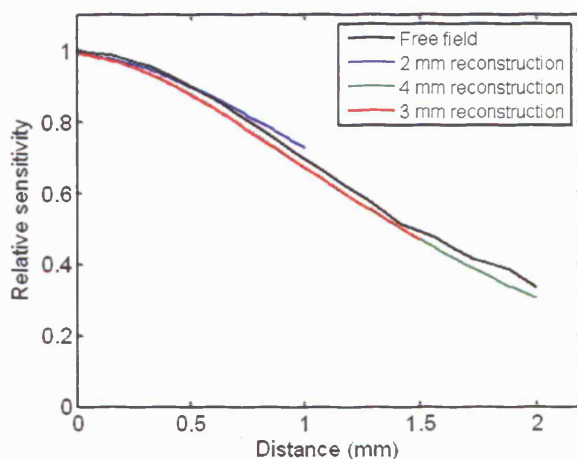


Figure 8.6 Beam shape reconstructions from flow phantom (shown separately in Figure 8.5). The reconstructions were converted from relative distances to absolute distances using knowledge of the phantom channel sizes and are shown in comparison to the free field beam sensitivity (solid black line).

Figure 8.7 is another combined plot. Again, it shows the reconstructed beam shapes from the three channels of the flow phantom. However, the x-axis corresponds to relative radial distances. This is more indicative of the information that would be available from the applications of the technique *in vivo*. In the absence of absolute radial distances, it is still possible to distinguish that the recordings came from channels of different diameters.

The shaded areas in the figure indicate the standard deviation of the reconstructed shapes. At $r/R = 1$ the relative sensitivities are (mean \pm s.d.) 0.75 ± 0.08 , 0.48 ± 0.06 and 0.30 ± 0.05 for the 2, 3 and 4 mm channels, respectively.

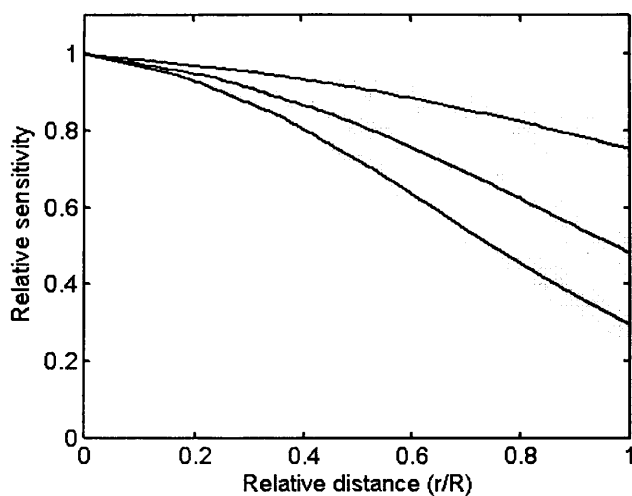


Figure 8.7 Beam shape reconstructions from three different sizes of flow phantom channel. Shaded areas correspond to standard deviation of estimates calculated by performing reconstructions of thirty 1-second segments of the Doppler signal.

Figure 8.8 is a more detailed examination of the variability of the reconstructed beam shapes for a single channel of the flow phantom. The enlarged inset shows the technique used to quantify the variation in the estimated radius of the channel. In this case, the range from one standard deviation below the mean to one standard deviation above was 14% of the mean channel radius.

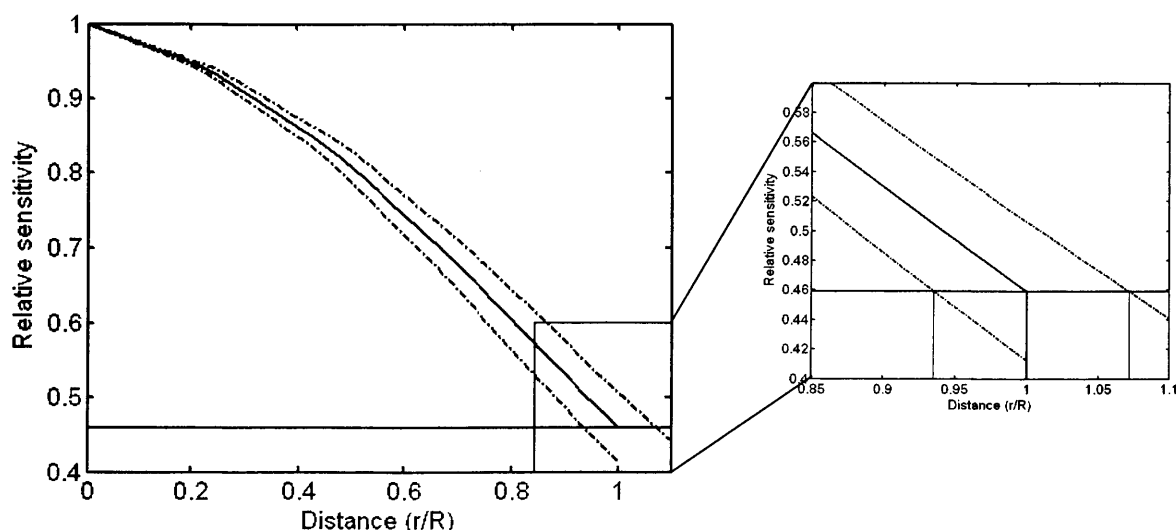


Figure 8.8 Variability in estimates of channel radius. The dashed lines correspond to one standard deviation from the mean beam shape reconstruction. They were produced, as in Figure 8.7, by making reconstructions of many shorter segments of the recording. The relative sensitivity of the average reconstruction at $r/R=1$ was established and the distances at which the upper and lower boundaries reached this level were used to determine a measure of the variation in vessel size relative to the beam.

By looking instead at the widths of the sensitivity profiles for ± 1.96 standard deviations from the mean, it was possible to determine the 2.5% tails of the distribution of the widths of the reconstructed beam shapes. These were found to have a positive skew. The relative diameters for the upper and lower 2.5% tails are presented in Table 8.1 for the three different vessels of the flow phantom. Presented along with these are the percentage changes in diameter that would be detectable at the 95% confidence level, assuming that both the original and new vessel size resulted in the same distribution of beam shape estimates.

Table 8.1 Values of sensitivity for upper and lower 2.5 % tails of the reconstructions of beam shapes from the Doppler signal recorded from each of the three flow phantom vessels. Also, the relative diameter changes that would thus be detectable using this technique.

	2 mm	3 mm	4 mm
r/R for lower 2.5% tail	0.72	0.85	0.88
r/R for upper 2.5% tail	1.70	1.20	1.13
Diameter increase detectable at 95% confidence level	136%	41%	28%
Diameter decrease detectable at 95% confidence level	58%	29%	22%

In vivo recordings

Figure 8.9 shows the mean (\pm s.d.) beam shape reconstructions for 30 seconds of *in vivo* data divided into one-second segments. This is the recording that produced the spectra shown in Figure 7.7. The *in vivo* sonogram was flattened using the technique described in Chapter 7 to allow all spectral estimates to be used in the averaging. The equivalent variation in vessel width (for one s.d. below to one s.d. above the mean beam shape) is 16% of the mean vessel width.

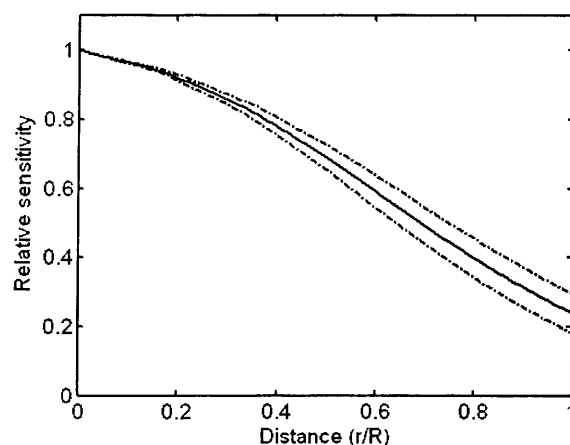


Figure 8.9 Mean beam shape reconstruction (solid line) \pm standard deviation (dashed line) for 30 one-second segments of *in vivo* data

The variability over a longer time was investigated using the extended TCD recording discussed in Chapter 7. A comparison was made between five seconds of data taken at 15-minute intervals, again from the same recording as used to produce Figure 8.9, above, and Figure 7.7. The variability in the vessel width determination, given by the standard deviation, was now 18% of the mean. The mean reconstructed beam profile is shown in Figure 8.10

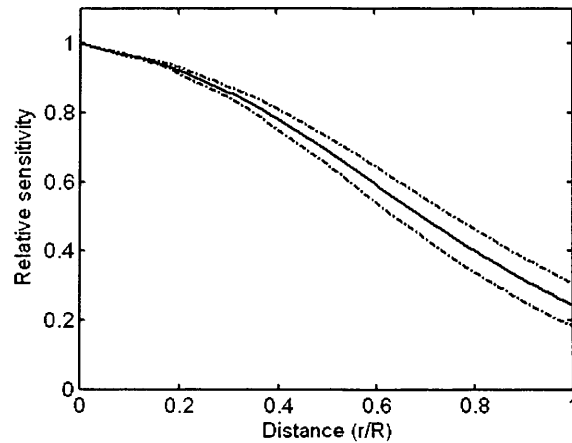


Figure 8.10 Variability of beam shape reconstructions for four *in vivo* recordings at 15-minute intervals (mean – solid line, \pm s.d. – dashed line)

Figure 8.11 shows reconstructed beam shapes from the other seven healthy subjects introduced in Chapter 7. (The sonograms and spectra for these recordings are shown in Figure 7.5.) The estimate of the vessel size relative to the beam is indicated on each plot. In general, these lie in the range $(0.5 - 2)r_{50\%}$. It should be remembered that $r_{50\%}$ is the 50% sensitivity width of the beam, and not the traditional beam width measurement of 50% (-6 dB) intensity – this would be 25% sensitivity, $r_{25\%}$. The vessel widths relative to $r_{25\%}$ are shown in Table 8.2. Although the data are few and have a wide distribution, they indicate that the vessels and beams are of similar widths (mean $R/r_{25\%} = 0.93$, s.d. ± 0.31). This is in keeping with expectations for an MCA diameter of 3 mm and the beam width measurements presented in Chapter 2.

Table 8.2 The estimated width of the MCA relative to the beam width (-6dB intensity = 25% sensitivity) for beam shape reconstructions from seven subjects

Subject	$R/r_{25\%}$	Subject	$R/r_{25\%}$
1	1.18	2	1.01
3	0.35	4	0.88
5	1.29	6	0.76
7	1.06		

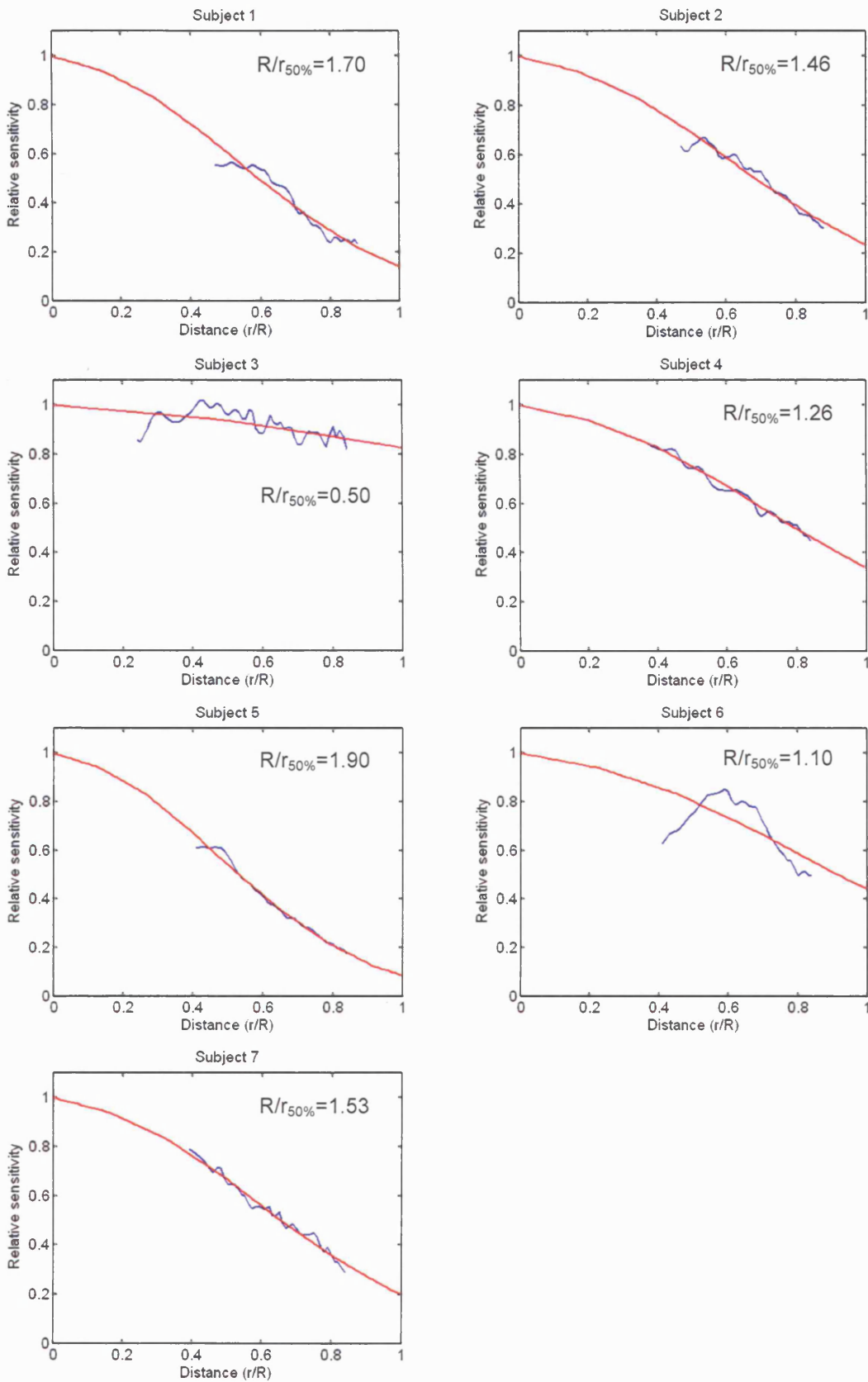


Figure 8.11 Reconstructed beam shapes (red lines) for the seven *in vivo* recordings introduced in Chapter 7. The figure on the top right of each plot indicates the estimated size of the vessel relative to the beam. The raw data, $P(r)$, is shown in blue.

Discussion

Assumptions necessary for technique

The explicit assumption of parabolic flow in the MCA and the implicit assumption that a beam shape based on free field measurements can accurately model the *in vivo* sensitivity are the two most debatable aspects of this work. In one sense, if the reconstructions are used purely for qualitative comparison purposes, the assumptions are not as specific as they appear at first and it was shown in Chapter 7 that there is good reason for believing that the flow in the MCA has a parabolic profile. However, an inappropriate mapping between velocities and radial differences would distort the appearance of the sensitivity information and, combined with an unsuitably shaped model, produce a reconstructed profile with little connection to reality.

It should be noted also that the free field beam shape, rather than a bone distorted beam shape, was used as the model to which the spectral data was fitted. This was chosen as the most flexible of the available beam shapes and also because there was no reason to suppose that any one beam shape would be more appropriate than another for the *in vivo* recordings. The free field shape fits to the average beam shape quite closely, as shown in Figure 8.12(a). The fit is poorer for bone sample 6 (Figure 8.12(b)), which was the most distorting of the bone samples, but it is still close.

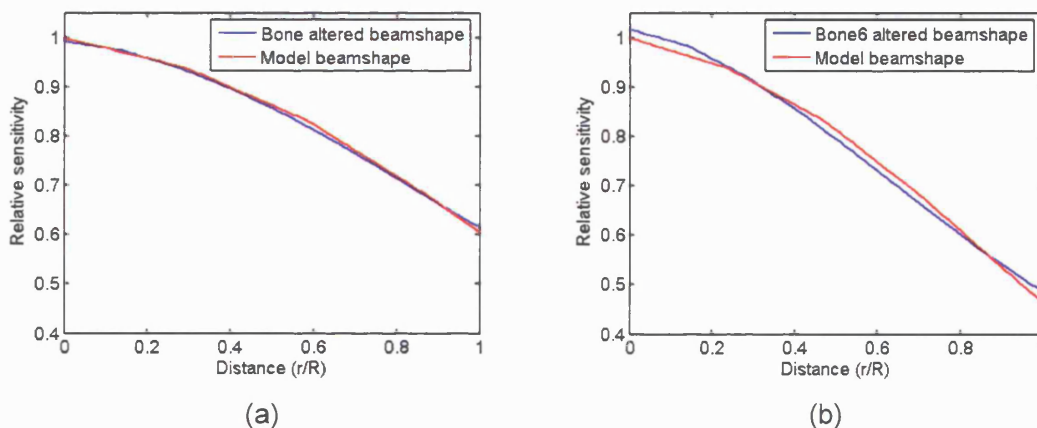


Figure 8.12 Comparison between the model shape (red line) used to fit the spectral data and reconstruct the beam shape and the average beam shape for all four bone samples (a) and the beam shape for bone sample 6 (b)

Comparison of reconstructed and measured beams

While discussing this issue, it is useful to include the results of the reconstructed profiles from the flow phantom recordings. The beam shape reconstruction is the estimate of the ultrasound sensitivity profile over the channel (or vessel) width. This

shape depends on both the sensitivity of the beam and the width of the vessel. Clearly, the Doppler signal can only contain information from the section of the ultrasound field that intersects with the vessel. *In vivo* the width is unknown, but *in vitro* the diameters of the channels through the flow phantom were defined in its construction. When scaled to these known channel widths (Figure 8.6), the reconstructions were consistent with each other and also with the free field measurement of the beam – a considerable endorsement of the technique.

The small differences between the two may be due to the variance in the reconstructed shapes, or it may have arisen from a systematic error in the method used to determine the free field beam shape within the phantom vessel. In order to determine that beam shape, it was necessary to process the data that were collected in the plots described in Chapter 2 in a similar manner to some of the steps described in the numerical model of Chapter 3. Firstly, the relative beam and vessel alignments were accounted for by matching the 45° angle of the flow phantom. This significantly changes the appearance of the ultrasound sensitivity within the vessel, as can be seen in Figure 8.13(a). The areas of highest sensitivity are no longer concentrated in the centre of the vessel but stretch across the lumen from top to bottom, with the highest sensitivity occurring at the proximal wall. This is due to the inherent beam shape, in particular the reduction of sensitivity with distance from the transducer. The radially averaged profile of this distribution is shown in Figure 8.13(b). The profile seen by the angled vessel is much flatter than the free field profile shown in Figure 2.4 for the reasons discussed in the section on angled vessels in Chapter 3, with the added effect of the much larger angle here (45° rather than 15°).

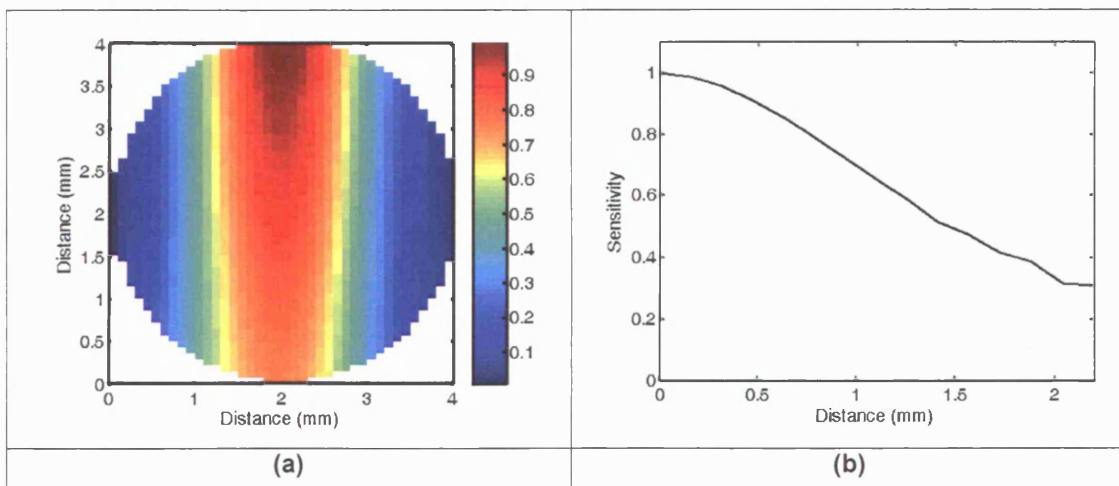


Figure 8.13 Distribution of ultrasound sensitivity within the channels of the wall-less flow phantom in (a) two-dimensions and (b) a one-dimensional radial average

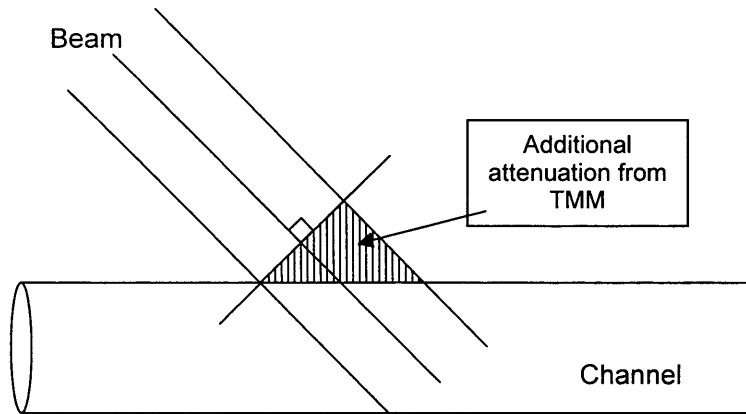
Additional attenuation

Figure 8.14. Illustration of variable path lengths through TMM along the length of the channels in the flow phantom

The angle of the vessel also introduces a variable amount of TMM between the transducer and vessel as shown in the diagram above (Figure 8.14). This is a much smaller effect than the first, causing an increase of no more than 1% in the relative sensitivity at large radii.

There is a further variation in TMM thickness in the direction perpendicular to the vessel axis (see Figure 8.15). The actual reduction in sensitivity at the edges of the channel depends on the width of the channel and the angle of insonation. For a beam perpendicular to the vessel the sensitivity is reduced by 2.3% for the 2 mm diameter channel and 4.7% for the 4 mm channel. For beam at an angle of 45° to the vessel, this would increase to 3.3% and 6.7%, respectively. This is a larger effect than that caused by the variable attenuation along the vessel length but the difference is barely perceptible, as shown in Figure 8.16.

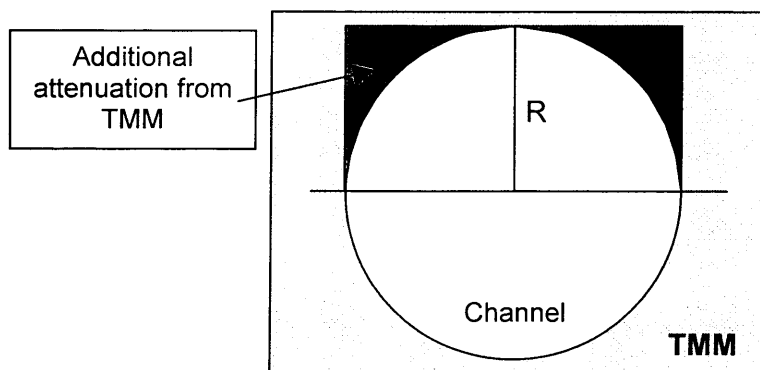


Figure 8.15 Diagram of additional attenuation of ultrasound beam away from the vessel centre. The periphery of the beam travels through a greater thickness of tissue mimicking material (TMM).

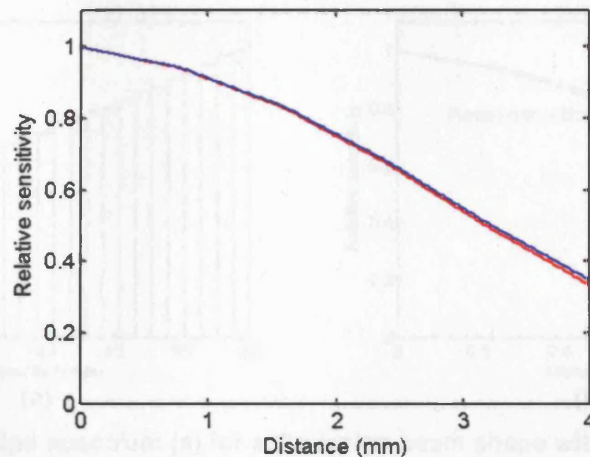


Figure 8.16 Effect of additional lateral attenuation on beam shape. The blue line plots the sensitivity of the free field beam. The red line is the calculated beam shape for the situation shown in Figure 8.13, where the edges of the beam pass through greater amounts of tissue mimicking material than the centre of the beam.

Flow profile

Even an accurate representation of the beam shape will not fit perfectly to data that has been distorted because of an invalid assumption of parabolic flow. However, the parabolic flow condition is likely to hold for the *in vitro* data because of the set up of the phantom with long inflow lengths through straight vessels and it was demonstrated in Chapter 7, by means of fluid dynamics equations, that the flow profile in the MCA is very nearly parabolic in shape. A beam shape can also be reconstructed from a modelled spectrum, where the flow profile is known to be exactly parabolic. The method for producing these spectra was described in Chapter 5 and such a spectrum is illustrated in Figure 8.17 below.

By using a modelling approach, both the original beam shape and the velocity profile are known exactly. The spectrum produced by the model was in turn used as the input to the beam reconstruction algorithm. The comparison between the beam shape input into the numerical model and the reconstruction produced by the reconstruction algorithm is shown in Figure 8.17(b). Again, there is a small difference between the two: the reconstruction has produced a slightly, steeper slope. The absolute limits of the accuracy of the technique are difficult to calculate and the evidence of the repeated reconstructions suggests that the determining factor may be the stochastic nature of the Doppler signal.

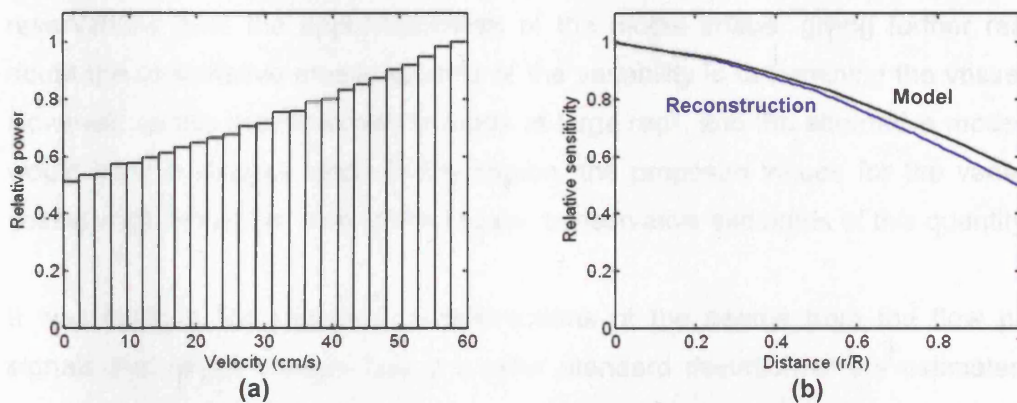


Figure 8.17 Modelled spectrum (a) for a Gaussian beam shape with a FWHM equal to the vessel diameter and (b) a comparison of the beam reconstructed from this spectrum with the original model beam shape

Suitability of model beam shape

There is no *a priori* basis for the assumption that the *in vivo* beam shape can be modelled by a profile based on free field sensitivity measurements. However, on the evidence of the sensitivity fields shown in Chapter 2, there is no one shape that can accurately describe the ultrasound beam within the skull. Thus, the choice of model is an arbitrary one. It was mentioned, in relation to Figure 8.4, that the chosen model shape might not be the best possible. Visually, there appears to be a shallower slope in the raw data than in the model at small distances and *vice versa* at large distances. Figure 8.18 (below) shows the match between the raw data and the model for an *in vivo* recording. The raw data was produced from the averaged power spectrum of a 30 second segment. It could be said that the same discrepancy between the shapes of the two exists, but it is less striking than in Figure 8.4.

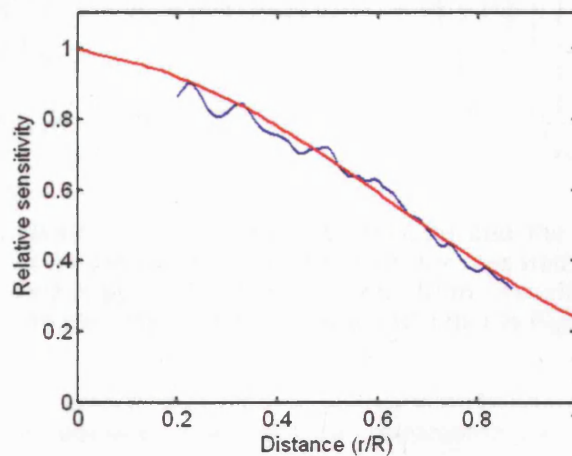


Figure 8.18 Raw sensitivity data (blue) and reconstructed beam shape (red) for a 30 second *in vivo* recording

Thus, although the fit of the model to the data is good, there may still be some reservations over the appropriateness of the model shape, giving further reason to doubt the quantitative measurements of the variability in determining the vessel width. However, as this measurement is made at large radii, and the alternative model shape would have a steeper slope in this region, the proposed values for the variability in vessel width would be, even if inaccurate, conservative estimates of this quantity.

It was seen in the repeated reconstructions of the beams from the flow phantom signals that larger vessels had a smaller standard deviation of the estimated beam shape. Larger vessels incorporate a wider variation in ultrasound sensitivity, or a greater portion of the overall beam shape. This will improve the fitting of a model shape to the raw data.

Even if the beam shape is correct, the use of the standard deviation to set confidence limits on the reconstructed shape could be inappropriate. The standard deviation is only appropriate for normally distributed data. Most of the distributions of sensitivity values at $r/R = 1$ were, indeed, normally distributed, and this is where the standard deviation was employed, but the transformation to vessel widths introduced skewness. Figure 8.19 shows a distribution of *in vivo* sensitivity values at $r/R = 1$ and the estimated vessel widths derived from these values.

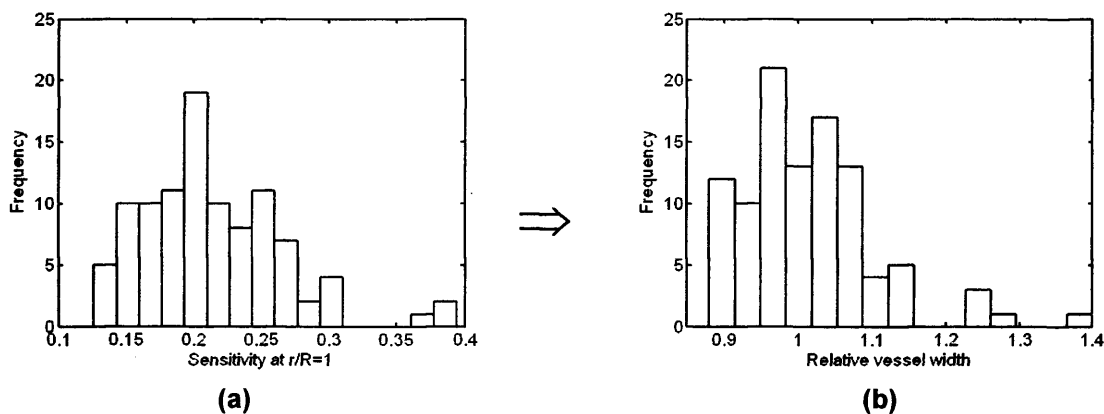


Figure 8.19 Distributions of sensitivities at $r/R=1$ (a) and the resulting distribution of vessel widths relative to the mean beam shape (b) for repeated reconstructions of 100 s of an *in vivo* recording. The conversion from sensitivity to relative width was performed in the manner indicated in Figure 8.8

To avoid relying on possibly inappropriate, parametric descriptors of the data, an empirical cumulative distribution function, ϕ , can be created; effectively a graphical representation of the technique used to produce the values in Table 8.1. This

distribution is displayed in Figure 8.20, together with insets that allow closer examination of the regions around $\phi = 0.025$ and $\phi = 0.975$ – the 2.5% tails. If this distribution were to apply to all *in vivo* reconstructions, a vessel would have to increase in diameter by 42%, or decrease by 30%, to be detected at the 5% level of significance. This is far in excess of any reported, pharmaceutically provoked, diameter changes in the MCA.

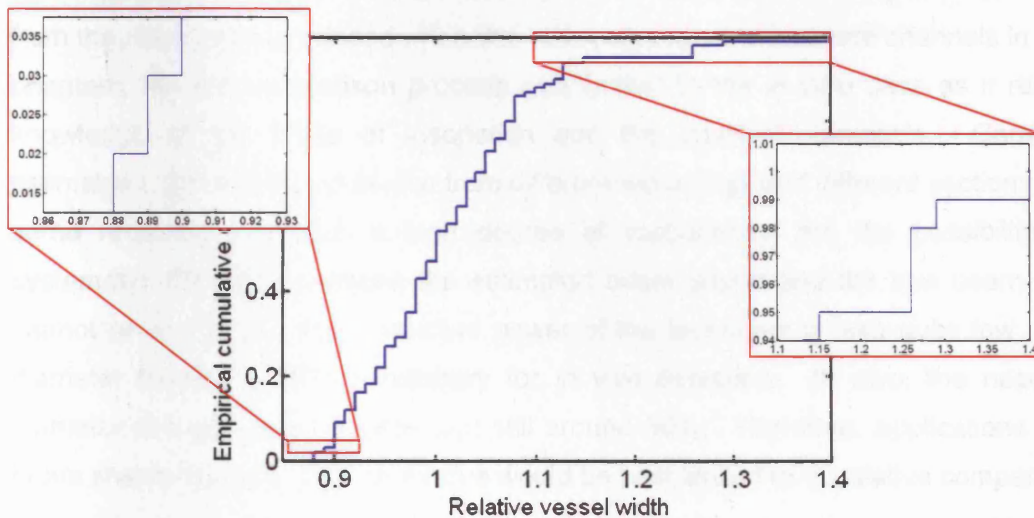


Figure 8.20 Empirical cumulative distribution function of relative vessel widths for repeated reconstructions of 100 s of an *in vivo* TCD recording

The magnitude of the detectable diameter changes are based on an assumption that the distribution of beam shape estimates has the same shape and size for both the original and the new vessel size. In fact, it was shown *in vitro* that larger vessels have a smaller distribution of estimates. Therefore, diameter increases smaller than the figures quoted in the previous paragraph and in Table 8.1 could be detected with 95% confidence. Unfortunately, the limited number of channel sizes in the flow phantom did not allow a closer investigation of the true values. Also of interest, was the fact that the *in vivo* recording did not produce a significantly larger standard deviation in the beam shape estimates than that from the 3 mm flow phantom channel. This is probably due to the reasonably high signal-to-noise of the *in vivo* signal, combined with the averaging technique that allowed all spectra in each one-second segment to be combined. It may be possible to reduce the variance in the beam shape estimates by averaging over a longer time. For example, taking two-second segments of data, the calculated diameter changes detectable in the 3 mm channel were reduced to a 22% increase and an 18% decrease – a little over half the values calculated for the one-

second segments. If this approach were to be taken, it would be necessary to ensure, however, that the vessel size could not have changed during the averaging period.

Conclusions

It is possible to use information contained within the Doppler signal to reconstruct a profile of the ultrasound beam used in the insonation of the vessel. Whether this reconstruction is an accurate representation of the actual beam is uncertain. Good agreement was found between a measured beam and the beam shapes reconstructed from the sonograms produced when this beam was used to insonate channels in a flow phantom, but the comparison process was limited to the *in vitro* case as it required knowledge of the angle of insonation and the channel diameters. Comparing estimates both *in vitro* and *in vivo* from different recordings and different sections of the same recording indicated a high degree of consistency, but the possibility of a systematic difference between the estimated beam shape and the true beam shape cannot be excluded. The predictive power of the technique is also quite low, with a diameter change of 42% necessary for *in vivo* detection. *In vitro*, the necessary diameter changes were smaller, but still around 30%. Therefore, applications of the beam shape reconstruction technique would be best limited to qualitative comparisons.

Chapter 9 – Summary and Conclusions

Summary of work

The work presented in the first half of this thesis demonstrated the significant non-uniformity of the transcranial ultrasound field. On a gross level, the non-uniformity arises from the inherent shape of the ultrasound as produced by the size of the piezoelectric crystal and the focussing built in to the housing. On a more detailed level, measurements of commercial ultrasound beams were made that demonstrated that non-uniformity was dependent in a unique way on the temporal bone sample through which the sound waves passed.

With this knowledge of the spatial variation in sensitivity, a numerical model was developed to explore the effects of the non-uniform insonation on the Doppler power returned by blood vessels in the field. Vessels were created in the model to simulate the shape of the MCA. These imitation vessels were of varying shapes from straight cylinders aligned along the beam axis to those that followed more complicated paths based on measurements of real MCA positions and others with trajectories that were angled with respect to the beam. By incorporating 3-D information on the ultrasound beam and the shape and path of the MCA, this model expanded on previous studies which were based on 2-D ultrasound sensitivity and limited vessel orientations.

From the model, maps of returned power were created. These showed the relative Doppler signal power returned from any given vessel and ultrasound field for each possible location of the vessel in the beam. The power maps were also used to determine the difference in returned power for vessels of different sizes located at the same point in the field. From this it was possible to compare the relative changes in power, ΔP , with the relative changes in area, ΔA , for any of the vessel shapes in any of the ultrasound fields. The ratio $\Delta P/\Delta A$ was used to examine the differences.

$\Delta P/\Delta A$ was significantly different from 1 for a number of vessel sizes and ultrasound fields with a minimum value of 0.58. The ratio was found to be below 1 for vessels that were centrally located in the beam, i.e. the change in Doppler power underestimated the change in vessel cross-section. The precise value depended on the size of the vessel and the particular sensitivity field. Larger vessels had a lower value of $\Delta P/\Delta A$ than smaller vessels for the same location in any given field. Vessels located toward

the periphery of the beam had higher values of $\Delta P/\Delta A$ than those in the centre with the ratio reaching values in excess of 1 at the largest distances.

A typical value for $\Delta P/\Delta A$ in each case was determined by taking the original power map for the vessel and field; isolating a sub-set of positions that returned power within 1 dB of the maximum; calculating $\Delta P/\Delta A$ for each of those positions and finding the median value. These median values were, naturally, larger than the individual values of $\Delta P/\Delta A$ at the most central locations, but were still less than 1 in every case. Thus, Doppler signal power methods generally underestimate changes in vessel size. For the 24 situations investigated in detail (four temporal bone samples, three sizes of model vessel and 10% increases and decreases in diameter) the median value of $\Delta P/\Delta A$ was 0.83 with a standard deviation of 0.08, implying that a Doppler power method would generally underestimate an area change in the MCA by $17\% \pm 8\%$.

In the second part of the thesis, the focus switched from modelling signal power to the examination of Doppler signals recorded *in vitro* and *in vivo*. The *in vitro* work was carried out using a wall-less phantom created from a tissue mimicking material through which a steady flow of blood mimicking fluid could be sent. A commercial TCD system was used to insonate channels of different diameters in the phantom and the resulting Doppler audio signals were recorded. These signals were processed to produce, first, sonograms and, then, averaged power spectra for each of the channels. Examination of the averaged power spectra proved that non-uniform insonation could occur in practice, at least in the more controlled environment of a flow phantom. The effect was clearly visible in the shape of the spectrum, along with features attributable to intrinsic spectral broadening and high-pass filters in the receiver electronics that are used to remove the low frequency signal from vessel walls.

TCD signals were collected from healthy volunteers to look for similar features *in vivo*. Although most of the processing of the data was the same as for the recordings taken from the flow phantom, a novel approach to averaging the signal was introduced to account for the pulsatile nature of the signal. Each spectrum of the sonogram was resampled to allow continuous averaging, rather than periodic averaging of systolic spectra. After analysis, it was found that these spectra also indicated non-uniform insonation of the vessel although the features were less striking due to the comparatively lower signal to noise ratio when compared with the *in vitro* signals.

The final section of the thesis described work on the reconstruction of profiles of ultrasound sensitivity from the information contained in the Doppler signal. Reconstructed beam shapes from both *in vitro* and *in vivo* recordings were produced. In the former case, comparisons were made with the known beam shape. It was found that the beam shape could not be reconstructed with sufficient accuracy to allow vessel diameter changes to be detected directly – a 42% change in diameter would be required to detect *in vivo* changes with 95% confidence. Nor was it possible to determine absolute vessel diameters, because of the unpredictability of the *in vivo* shape and position of the ultrasound beam.

Further work

Using reconstructions to correct signal power method

Having shown that non-uniform insonation occurs *in vivo* and estimating the errors that it can cause when using a signal power technique, the next step would be to find a method by which these errors may be corrected or reduced. Obviously one approach would be to use a wider TCD beam, i.e. decrease the inherent non-uniformity of the ultrasound field. However, there is no guarantee that the increased beam width and flatter sensitivity profile will endure in the presence of temporal bone. The second approach is to use the information on beam shape that can be extracted from the sonogram to apply a correction factor to the measured changes in power. The outline of such an approach follows.

First, the beam shape must be reconstructed from the averaged power spectrum. This indicates the size, R , of the vessel relative to the width of the beam. The 50% sensitivity radius, $r_{50\%}$, can be designated as the beam "width". For smaller vessels, or broader beams, it may be necessary to extrapolate the reconstruction to find the radial distance at which the sensitivity would drop to 50%. Otherwise, the relative radius at which the reconstructed sensitivity profile has a value of 0.5 can be read from the plot. The estimated ratios of vessel diameter to beam width for the *in vivo* recordings were included in Chapter 8. The vessel sizes ranged from being almost the same as the beam width to being nearly twice as large.

The second step requires the creation of a look-up table of correction values for vessel of different sizes relative to the beam. This provides a correspondence between the measured change in the power and the actual change in area. This table can be

generated from the modelling program and comprises the typical discrepancies between power and area changes for each of the relative vessel sizes. In order to be more generally applicable, the look-up table could be created for a generic beam shape, rather than any particular TCD system or bone sample, but it might be possible to tailor the data to a specific spectral shape.

Finally, the user can take the information on vessel size and power change and use the look-up table to find the change in area. An example of such a table has been created for illustration purposes (Table 9.1). It is based on free-field sensitivity data and a straight, cylindrical vessel. This table gives an estimate of the change in area that occurs for each of four changes in the measured power. It is necessary to divide the results into vessels of different sizes relative to the ultrasound beam to account for the effect that vessel size has on the average ultrasound sensitivity.

To use the table, the ratio of beam width to vessel size estimated in step one is used to choose the appropriate row. Then, the size of the measured power change is used to choose the appropriate column. The figure at the intersection of row and column is the estimate of the change in vessel cross-section.

Table 9.1 Example of a look-up table for signal power method correction. Using an estimate of the vessel width relative to the beam size, a measured change in power can be converted to a change in vessel cross-section

		Measured change in power				Modelled change in area
		5%	10%	15%	20%	
Relative vessel diameter ($R/r_{50\%}$)	0.5	5%	11%	16%	22%	
	1	6%	13%	20%	27%	
	1.25	8%	16%	24%	33%	
	1.5	9%	19%	30%	42%	
		Modelled change in area				

Verification of signal power correction factors

The difficulty with applying this method is that there is no way of determining the accuracy of the beam shape reconstruction. This means that the modelled correction factor might actually reduce the accuracy of the signal power method rather than increase it. This is especially a concern when the results of the *in vitro* reconstruction are considered. It was shown in Chapter 8 that there was a clear discrepancy between the reconstructed beam shapes and the beam as measured in water.

Furthermore, it was not possible to apply the correction factors to those *in vitro* recordings in order to investigate their suitability. The flow phantom channels were physically separated and there was no guarantee that the relative position of the beam with respect to the channel was the same in each case, although the consistency of the reconstructed beam shapes suggests that the alignment was good. Application of the look-up table to *in vivo* recordings would not be useful without an assured mechanism for provoking changes in MCA diameter and a dependable solution to the original problem of measuring those diameter changes.

One possibility for verifying the look-up table is to make measurements on a vessel-mimicking phantom where changes in flow rate can be used to provoke changes in the diameter of a vessel, constructed from a suitably elastic material. For such a set-up, flow signals from vessels of different diameters could be measured without the need for repositioning the transducer.

Checking reconstruction technique in vivo in vasospasm

It was shown in Chapter 8 that the reconstruction technique is limited to the detection of very large changes in MCA diameter, changes outwith the capability of pharmaceutical provocations. However, diameter changes of around 50% can be seen during vasospasm in patients with severe head injuries. It would be a useful test of the technique to perform reconstructions from TCD data collected during vasospasm and subsequent to successful treatment. This may also address some of the difficulties that result in a lack of correlation between TCD and rCBF measurements that have been found in some studies (Vajkoczy et al. 2001).

Conclusions

Although TCD is widely used for the monitoring of cerebral haemodynamics, its limitations are often poorly understood or ignored. Changes in velocity are frequently equated with changes in volumetric flow without any consideration of vasoreactivity in the basal vessels. Those workers who do consider the possibility of size variability in the MCA generally rely on a measurement of the total signal power or an index based on signal power to reveal any diameter changes. While this is an improvement, it still does not include provision for any inhomogeneity in the ultrasound field used to insonate the vessel. An unconsidered application of the Doppler signal power method can result in large errors (up to 42% and typically $17\% \pm 8\%$ for the models presented) in the quantification of blood flow changes. This indicates the need for careful and considered interpretation of TCD results when vessel diameter changes may be present.

References

AIUM and NEMA. "Standards for real-time display of thermal and mechanical acoustic output indices on diagnostic ultrasound equipment." American Institute of Ultrasound in Medicine and National Electrical Manufacturers Association. 1992.

Angell, E. L. and Evans, D. H. Limits of uncertainty in measured values of embolus-to-blood ratio due to Doppler sample volume shape and location. *Ultrasound in Medicine and Biology*. 2003 July; 29(7):1037-1044.

Arts, M. G. J. and Roelvros, J. M. J. Instantaneous measurement of bloodflow by ultrasonic means. *Medical & Biological Engineering*. 1972; 10(1):23-34.

Aubry, J. F.; Tanter, M.; Pernot, M.; Thomas, J. L., and Fink, M. Experimental demonstration of noninvasive transskull adaptive focusing based on prior computed tomography scans. *Journal of the Acoustical Society of America*. 2003 Jan; 113(1):84-93.

Axel, L. Cerebral blood-flow determination by rapid-sequence computed-tomography - a theoretical-analysis. *Radiology*. 1980; 137(3):679-686.

Balbis, S.; Guiot, C.; Roatta, S.; Arina, R., and Todros, T. Assessment of the effect of vessel curvature on Doppler measurements in steady flow. *Ultrasound in Medicine and Biology*. 2004 May; 30(5):639-645.

Bednarczyk, E. M.; Wack, D. S.; Kassab, M. Y.; Burch, K.; Trinidad, K.; Haka, M. and Gona, J. Brain blood flow in the nitroglycerin (GTN) model of migraine: measurement using positron emission tomography and transcranial Doppler. *Cephalalgia*. 2002; 22:749-757.

Brands, P. J.; Hoeks, A. P. G., and Reneman, R. S. The effect of echo suppression on the mean velocity estimation range of the RF cross-correlation model estimator. *Ultrasound in Medicine and Biology*. 1995; 21(7):945-959.

British Medical Ultrasound Society. Guidelines for the safe use of diagnostic ultrasound equipment. [Web page] 2000; Accessed 2005 November 24. Available at: http://www.bmus.org/BMUS_Safety_Guidelines_final.htm.

Clark, James M.; Skolnick, Brett E.; Gelfand, Rober; Farber, Roger E.; Stierheim, Maria; Stevens, W. Craig; Beck, George Jr. and Lambertsen, Christian J. Relationship of ^{133}Xe cerebral blood flow to middle cerebral artery flow velocity in men at rest. *Journal of Cerebral Blood Flow and Metabolism*. 1996 November; 16(6):1255-1262.

Dahl, Arve; Russell, David; Nyberg-Hansen, Rolf and Rootwelt, Kjell. Effect of Nitroglycerin on cerebral circulation measured by transcranial Doppler and SPECT. *Stroke*. 1989; 20:1733-1736.

Dahl, A.; Russell, D.; Nyberghansen, R.; Rootwelt, K., and Bakke, S. J. Cerebral vasoreactivity in unilateral carotid-artery disease - a comparison of blood-flow velocity and regional cerebral blood-flow measurements. *Stroke*. 1994 Mar; 25(3):621-626.

Dahl, Arve; Russell, David; Rootwelt, Kjell; Nyberg-Hansen, Rolf and Kery, Emilia. Cerebral vasoreactivity assessed with transcranial Doppler and regional cerebral blood flow measurements: dose, serum concentration and time course of the response to acetazolamide. *Stroke*. 1995 Dec; 26(12):2302-2306.

- Dejong, D. A.; Megens, P. H. A.; Devlieger, M.; Thon, H. and Holland, W. P. J. Directional quantifying Doppler system for measurement of transport velocity of blood. *Ultrasonics*. 1975; 13(3):138-141.
- Démolis, P.; Dinh, Y. R. T. and Giudicelli, J. F. Relationships between cerebral regional blood flow velocities and volumetric blood flows and their respective reactivities to acetazolamide. *Stroke*. 1996 Oct; 27(10):1835-1839.
- Detre, J. A.; Alsop, D. C.; Vives, L. R.; Maccotta, L.; Teener, J. W. and Raps, E. C. Noninvasive MRI evaluation of cerebral blood flow in cerebrovascular disease. *Neurology*. 1998 Mar; 50(3):633-641.
- Detre, J. A.; Samuels, O. B.; Alsop, D. C.; Gonzalez-at, J. B.; Kasner, S. E., and Raps, E. C. Noninvasive magnetic resonance imaging evaluation of cerebral blood flow with acetazolamide challenge in patients with cerebrovascular stenosis. *Journal of Magnetic Resonance Imaging*. 1999 Nov; 10(5):870-875.
- Deverson, Stephanie and Evans, David H. The effects of beam shape on the ability to predict changes in vessel size from Doppler signal power. *Ultrasound in Medicine and Biology*. 2000a; 26(2):245-253.
- Deverson, Stephanie and Evans, David H. Using Doppler signal power to detect changes in vessel size: a feasibility study using a wall-less flow phantom. *Ultrasound in Medicine and Biology*. 2000b; 26(4): 593-602.
- Deverson, Stephanie; Evans, David H, and Bouch, D Clive. The effects of temporal bone on the transcranial Doppler ultrasound beam shape. *Ultrasound in Medicine and Biology*. 2000; 26(2): 239-244.
- Edmeads, J. Cerebral Blood-Flow in Migraine. *Headache*. 1977; 17(4):148-152.
- Eicke, B. M.; Buss, E.; Bahr, R. R.; Hajak, G., and Paulus, W. Influence of Acetazolamide and CO₂ on extracranial flow volume and intracranial blood flow velocity. *Stroke*. 1999 Jan; 30(1):76-80.
- Evans, D.H. Some aspects of the relationship between instantaneous volumetric blood-flow and continuous wave Doppler ultrasound recordings - III. The calculation of Doppler power spectra from mean velocity waveforms, and the results of processing these spectra with maximum, mean, and rms frequency processors. *Ultrasound in Medicine and Biology*. 1982; 8(6):617-623.
- Finn, John Paul; Quinn, Michael William; Hall-Craggs, Margaret Anne and Kendall, Brian E. Impact of vessel distortion on transcranial Doppler velocity measurements: correlation with magnetic resonance imaging. *Journal of Neurosurgery*. 1990; 73:572-575.
- Fish, P. J. Nonstationarity broadening in pulsed Doppler spectrum measurements. *Ultrasound in Medicine and Biology*. 1991; 17(2):147-155.
- Friberg, Lars; Olsen, Jes; Iversen, Helen K. and Sperling, Bjørn. Migraine pain associated with middle cerebral artery dilatation: reversal by sumatriptan. *The Lancet*. 1991 July 6; 338:13-17.

Fujii, M.; Sakamoto, K.; Toda, Y.; Negishi, A. and Kanai, H. Study of the cause of the temperature rise at the muscle-bone interface during ultrasound hyperthermia. *IEEE Transactions on Biomedical Engineering* 1999 May; 46(5):494-504.

Giller, C. A.; Hatab, M. R., and Giller, A. M. Estimation of vessel flow and diameter during cerebral vasospasm using transcranial Doppler indices. *Neurosurgery*. 1998 May; 42(5):1076-1081.

Haase, C. G.; Becka, M.; Kuhlmann, J., and Wensing, G. Influences of caffeine, acetazolamide and cognitive stimulation on cerebral blood flow velocities. *Progress in Neuro-Psychopharmacology & Biological Psychiatry*. 2005 May; 29(4):549-556.

Halsey, J. H. Effect of emitted power on wave-form intensity in transcranial Doppler. *Stroke*. 1990 Nov; 21(11):1573-1578.

Hart, R. and Haluszkiewicz, E. Blood flow velocity using transcranial Doppler velocimetry in the middle and anterior cerebral arteries: correlation with sample volume depth. *Ultrasound in Medicine and Biology*. 2000 Oct; 26(8):1267-1274.

Hatab, M. R., Giller, C. A., and Clarke, G. D., Evaluation of cerebral arterial flow with transcranial Doppler ultrasound: theoretical development and phantom studies *Ultrasound in Medicine and Biology*, 1997; 23:1025-1031.

Heimdal, A. and Torp, H. Ultrasound Doppler measurements of low velocity blood flow: limitations due to clutter signals from vibrating muscles. *IEEE Transactions on Ultrasonics Ferroelectrics and Frequency Control*. 1997 Jul; 44(4):873-881.

Hoksbergen, A. W. J.; Legemate, D. A.; Ubbink, D. T., and Jacobs Mijhm. Success rate of transcranial color-coded duplex ultrasonography in visualizing the basal cerebral arteries in vascular patients over 60 years of age. *Stroke*. 1999 Jul; 30(7):1450-1455.

Hunter, R.; Mcluskie, R.; Wyper, D.; Patterson, J.; Christie, J. E.; Brooks, D. N.; McCulloch, J.; Fink, G., and Goodwin, G. M. The pattern of function-related regional cerebral blood-flow investigated by single photon-emission tomography with Tc-99m-HMPAO in patients with presenile Alzheimers-disease and Korsakoffs psychosis. *Psychological Medicine*. 1989 Nov; 19(4):847-.

Itoh, T.; Matsumoto, M.; Handa, N.; Maeda, H.; Hougaku, H.; Hashimoto, H.; Etani, H.; Tsukamoto, Y., and Kamada, T. Rate of successful recording of blood-flow signals in the middle cerebral-artery using transcranial Doppler sonography. *Stroke*. 1993 Aug; 24(8):1192-1195.

Jarquín-Valdivia, A. A.; McCartney, J.; Palestrant, D.; Johnston, S. C., and Gress, D. The Thickness of the Temporal Squama and Its Implication for Transcranial Sonography. *Journal of Neuroimaging*. 2004 Apr; 14(2):139-142.

Kelley, R. E.; Chang, J. Y.; Scheinman, N. J.; Levin, B. E.; Duncan, R. C., and Lee, S. C. Transcranial Doppler assessment of cerebral flow velocity during cognitive tasks. *Stroke*. 1992 Jan; 23(1):9-14.

Kety, SS and Schmidt CF. The determination of cerebral blood flow in man by the use of nitrous oxide in low concentrations. *American Journal of Physiology*. 1945; 143: 53-66.

Kleiser, B.; Scholl, D., and Widder, B. Doppler CO₂ and Diamox test - decreased reliability by changes of the vessel diameter. *Cerebrovascular Diseases*. 1995 Nov-1995 Dec 31; 5(6):397-402.

Kossoff, G. Analysis of focusing action of spherically curved transducers. *Ultrasound in Medicine and Biology*. 1979; 5:359-365.

Kruise, C.; Jacobsen, T. B.; Lassen, L. H.; Thomsen, L. L.; Hasselbalch, S. G.; Dige-Petersen, H., and Olesen, J. Dipyridamole dilates large cerebral arteries concomitant to headache induction in healthy subjects. *Journal of Cerebral Blood Flow and Metabolism*. 2000 Sep; 20(9):1372-1379.

Kruise, C.; Thomsen, L. L.; Birk, S., and Olesen, J. Migraine can be induced by Sildenafil without changes in middle cerebral artery diameter. *Brain*. 2003 Jan; 126:241-247.

Lassen, N. A.; Henriksen, L., and Paulson, O. Regional cerebral blood-flow in stroke by Xe-133 inhalation and emission tomography. *Stroke*. 1981; 12(3):284-288.

Lindgaard, Karl-Fredrik; Lundar, Tryggve; Wiberg, Jan; Sjoberg, Dag; Aaslid, Rune, and Normes, Helge. Variations in middle cerebral artery blood flow investigated with noninvasive transcranial blood velocity measurements. *Stroke*. 1987; 18:1025-1030.

Lubbers, Jaap. Application of a new blood-mimicking fluid in a flow Doppler test object. *European Journal of Ultrasound*. 1999; 9, 267-276.

Lunt, M. J.; Ragab, S.; Birch A. A.; Schley D. and Jenkinson, D. F. Comparison of caffeine-induced changes in cerebral blood flow and middle cerebral artery blood velocity shows that caffeine reduces middle cerebral artery diameter. *Physiological Measurement*. 2004; 25:467-474.

Maeda, H.; Etani, H.; Handa, N.; Tagaya, M.; Oku, N.; Kim, B. H.; Naka, M.; Kinoshita, N.; Nukada, T.; Fukunaga, R.; Isaka, Y.; Matsumoto, M.; Kimura, K., and Kamada, T. A validation-study on the reproducibility of transcranial Doppler velocimetry. *Ultrasound in Medicine and Biology*. 1990; 16(1):9-14.

Marinoni, M.; Ginanneschi, A.; Forleo, P., and Amaducci, L. Technical limits in transcranial Doppler recording: inadequate acoustic windows. *Ultrasound in Medicine and Biology*. 1997; 23(8):1275-1277.

Mascia, L.; Fedorko, L.; Terbrugge, K.; Filippini, C.; Pizzio, M.; Ranieri, V. M., and Wallace, M. C. The accuracy of transcranial Doppler to detect vasospasm in patients with aneurysmal subarachnoid hemorrhage. *Intensive Care Medicine*. 2003 Jul; 29(7):1088-1094.

Mo, Larry YL; Yun, Louis CM, and Cobbold, RSC. Comparison of four digital maximum frequency estimators for Doppler ultrasound. 1988; 14(5):355-363.

Muller, M. and Marziniak, M. The linear behavior of the system middle cerebral artery flow velocity and blood pressure in patients with migraine - lack of autonomic control? *Stroke*. 2005 Sep; 36(9):1886-1890.

Niehaus, L.; Gottschalk, S., and Weber, U. Influence of nitroglycerin-induced dilation of basal brain arteries on MCA blood flow velocity and volume flow. *Ultraschall in Der Medizin*. 1998 Oct; 19(5):225-229.

Ogasawara, K.; Ito, H.; Sasoh, M.; Okuguchi, T.; Kobayashi, M.; Yukawa, H.; Terasaki, K., and Ogawa, A. Quantitative measurement of regional cerebrovascular reactivity to Acetazolamide using (123) I-N-Isopropyl-P-Iodoamphetamine autoradiography with SPECT: Validation study using (H₂O)-O-15 with PET. *Journal of Nuclear Medicine*. 2003 Apr; 44(4):520-525.

Oskouian, R. J.; Martin, N. A.; Lee, J. H.; Glenn, T. C.; Guthrie, D.; Gonzalez, N. R.; Afari, A., and Vinuela, F. Multimodal quantitation of the effects of endovascular therapy for vasospasm on cerebral blood flow, transcranial Doppler ultrasonographic velocities, and cerebral artery diameters. *Neurosurgery*. 2002 Jul; 51(1):30-41.

Poulin, M. J. and Robbins, P. A. Indexes of flow and cross-sectional area of the middle cerebral artery using Doppler ultrasound during hypoxia and hypercapnia in humans. *Stroke*. 1996 Dec; 27(12):2244-2250.

Ramnarine, Kumar V; Nassiri, Dariush K; Hoskins, Peter R, and Lubbers, Jaap. Validation of a new blood-mimicking fluid for use in Doppler flow test objects. 1998; 24(3): 451-459.

Ramnarine, Kumar V; Anderson, T, and Hoskins, Peter R. Construction and geometric stability of physiological flow rate wall-less stenosis phantoms. *Ultrasound in Medicine and Biology*. 2001; 27(2):245-250.

Russell D and Brucher R. Non-invasive middle cerebral artery blood flow and diameter assessments. (Abstract.) *Stroke*. 2004 Jun; 35 (6):E259-E259.

Schmetterer, L.; Wolzt, M.; Krejcy, K.; Graselli, U.; Findl, O.; Eichler, H. G., and Singer, E. A. Cerebral and ocular hemodynamic effects of sumatriptan in the nitroglycerin headache model. *Clinical Pharmacology & Therapeutics*. 1996 Aug; 60(2):199-205.

Serrador, Jorge M; Picot, Paul A; Rutt, Brian K; Shoemaker, J Kevin, and Bondar, Roberta L. MRI measures of middle cerebral artery diameter in conscious humans during simulated orthostasis. 2000 Jul; 31, (7): 1672-1678.

Settakis, G.; Molnar, C.; Kerenyi, L.; Kollar, J.; Legemate, D.; Csiba, L., and Fulesdi, B. Acetazolamide as a vasodilatory stimulus in cerebrovascular diseases and in conditions affecting the cerebral vasculature. *European Journal of Neurology*. 2003 Nov; 10(6):609-620.

Shaw, A.; Pay, N.M. and Preston, R.C. Assessment of the likely thermal index values for pulse Doppler ultrasonic equipment – Stage II: experimental assessment of scanner/transducer combinations. NPL Report CMAM 12. National Physical Laboratory, Middlesex, UK. March 1998.

Silvestrini, M.; Baruffaldi, R.; Bartolini, M.; Vernieri, F.; Lanciotti, C.; Matteis, M.; Troisi, E., and Provinciali, L. Basilar and middle cerebral artery reactivity in patients with migraine. *Headache*. 2004 Jan; 44(1):29-34.

Skinhøj, E.; Hoedtras, K; Paulson, O. B., and Lassen, N. A. Regional cerebral blood flow and its autoregulation in patients with transient focal cerebral ischemic attacks. *Neurology*. 1970; 20(5):485-.

Thomaides, T.; Karagounakis, D.; Spantideas, A., and Katelanis, S. Transcranial Doppler in migraine attacks before and after treatment with oral zolmitriptan or sumatriptan. *Headache*. 2003 Jan; 43(1):54-58.

Thompson, R. S.; Aldis, G. K. and Linnett, I.W. Doppler ultrasound spectral power density distribution: measurement artifacts in steady flow. *Medical and Biological Engineering and Computing*. 1990; 28:60-66.

Thompson, R. S. and Aldis, G. K. Flow spectra from spectral power density calculations for pulsed Doppler. *Ultrasonics*. 2002; 40:835-841.

Totaro, R.; Marini, C.; Cannarsa, C., and Prencipe, M. Reproducibility of transcranial Doppler sonography - a validation-study. *Ultrasound in Medicine and Biology*. 1992; 18(2):173-177.

Totaro, R.; Marini, C.; Dematteis, G.; Dinapoli, M., and Carolei, A. Cerebrovascular reactivity in migraine during headache-free intervals. *Cephalalgia*. 1997a May; 17(3):191-194.

Totaro, R.; De Matteis, G.; Marini, C.; Baldassarre, M., and Carolei, A. Sumatriptan and cerebral blood flow velocity changes during migraine attacks. *Headache*. 1997b Nov; 37(10):635-639.

Vajkoczy, P.; Horn, P.; Bauhuf, C.; Munch, E.; Hubner, U.; Thome, C.; Poeckler-Schoeninger, C.; Roth, H., and Schmiedek, P. Effect of intra-arterial papaverine on regional cerebral blood flow in hemodynamically relevant cerebral vasospasm. *Stroke*. 2001 Feb; 32(2):498-505.

Valdueza, José Manuel; Balzer, Jörn Oliver; Villringer, Arno; Vogl, Thomas Josef; Kutter, Raphael, and Einhäupl, Karl Max. Changes in blood flow velocity and diameter of the middle cerebral artery during hyperventilation: assessment with MR and transcranial Doppler sonography. *American Journal of Neuroradiology*. 1997a Nov; 18, 1929-1934.

Valdueza, José Manuel; Balzer, Jörn Oliver; Villringer, Arno; Vogl, Thomas Josef; Kutter, Raphael, and Einhäupl, Karl Max. Effect of hyperventilation on the diameter and blood flow velocity of the middle cerebral artery: A TCD and MR study. Klingelhofer, J.; Bartels, E., and Ringelstein, E. B., editor. *New Trends in Cerebral Hemodynamics and Neurosonology*. Elsevier; 1997b; pp. 215-220.

Van der Zwan, Albert; Hillen, Berend; Tulleken, Cornelius A. F. and Dujovny, Manuel. A quantitative investigation of the variability of the major cerebral artery territories. *Stroke*. 1993; 24:1951-1959.

White, R. P.; Deane, C.; Hindley, C.; Bloomfield, P. M.; Cunningham, V. J.; Vallance, P.; Brooks, D. J. and Markus, H. S. The effect of the nitric oxide donor glyceryl trinitrate on global and regional cerebral blood flow in man. *Journal of the Neurological Sciences*. 2000; 178:23-28.

Wu, Junru; Cubberley, Frances; Gormley, Gerard and Szabo, Thomas L. Temperature rise generated by diagnostic ultrasound in a transcranial phantom. *Ultrasound in Medicine and Biology*. 1995; 21(4):561-568.